

LUCAS CAETANO GROSCHE

STUDY OF THE INTERACTIONS BETWEEN EMULSION FLOW AND A
SPECTROMETER PROBE BASED ON NUMERICAL SIMULATIONS

São Paulo, 2014

LUCAS CAETANO GROSCHE

STUDY OF THE INTERACTIONS BETWEEN EMULSION FLOW AND A
SPECTROMETER PROBE BASED ON NUMERICAL SIMULATIONS

Dissertação apresentada à Escola
Politécnica da Universidade de São Paulo
para obtenção do título de Mestre em
Engenharia

São Paulo
2014

LUCAS CAETANO GROSCHE

STUDY OF THE INTERACTIONS BETWEEN EMULSION FLOW AND A
SPECTROMETER PROBE BASED ON NUMERICAL SIMULATIONS

Dissertação apresentada à Escola
Politécnica da Universidade de São Paulo
para obtenção do título de Mestre em
Engenharia

Área de concentração: Engenharia Química

Orientador: Prof. Dr. José Luís de Paiva

São Paulo
2014

Este exemplar foi revisado e corrigido em relação à versão original, sob responsabilidade única do autor e com a anuência de seu orientador.

São Paulo, 05 de fevereiro de 2014.

Assinatura do autor _____

Assinatura do orientador _____

Grosche, Lucas Caetano

Study of the interactions between emulsion flow and a spectrometer probe based on numerical simulations / L.C.

Grosche. – versão corr. -- São Paulo, 2014.

81 p.

Dissertação (Mestrado) - Escola Politécnica da Universidade de São Paulo. Departamento de Engenharia Química.

1.Oil-in-water 2.Emulsion flow 3.Computational fluid dynamics 4.Multiphase flow I.Universidade de São Paulo. Escola Politécnica. Departamento de Engenharia Química II.t.

ACKNOWLEDGMENTS

I would like to express my greatest gratitude to the people who have helped and supported me throughout my project. I am grateful to Professor Jose Luis de Paiva for the continuous support for the project, from initial advice & contacts in the early stages of conceptual inception & through ongoing advice & encouragement to this day. As well from the Brazilian coordinator from the EPM project Prof. Roberto Guardani, who gave me the golden opportunity to be part of his research team, which include the opportunity of working in an international research group, in collaboration with the University of Bremen.

I wish express my gratitude to my good friend José Eduardo Alves, the person who first encouraged me to do my master in Chemical engineer and the one who always was there to support me every time a thought I couldn't make it to the end.

I am grateful to Professor Galo A. Carrillo Le Roux, who was the one to first introduce me to Professor Guardani, and without his help I could never have start my Master.

I would like to express my gratitude for Professor Udo Fritsching, and all the colleagues from the University of Bremen, for being so well received and supported during all the time I was there. I am grateful to my german friends; Sören and Benjamin who help me during the time I was in Germany.

I would like to express my gratitude to my friends here at the University of Sao Paulo; Cristhiane, Adriana, Lidiane, Fernando, Fabiana, Lina, Esmar and Cristiana who made my university life easier.

I wish to thank my parents for their tremendous contributions and support both morally and financially towards the completion of my studies. And my sister, Catarina, who was always supporting me, and never let my down.

ABSTRACT

In the present work, the flow behavior of an oil-in-water emulsion around and inside the measurement chamber of an in-line optical sensor probe is studied. The emulsion consists of a metalworking fluid, with oil droplets diameter ranging from 100 nanometers to 100 micrometers. The design of the UV-Vis light spectrometer probe is in accordance with the concept proposed in the research project named EPM (Emulsion Process Monitor in Metalworking Processes), carried out within the scope of the BRAGECRIM program between the University of São Paulo and the University of Bremen. This study is based on the numerical simulation of the interactions between the emulsion and the measurement system using computational fluid dynamic techniques, and is aimed at evaluating the effects of the probe geometry, its position relative to the flow field, and fluid properties on the expected spectrometer readings. Such effects are correlated with changes in droplet concentration and or droplet size segregation inside the measurement chamber of the optical probe, which can cause changes in the scattered light intensity readings.. Segregation effects due to flow disturbances around the probe can be neglected under normal measurement conditions, with the probe facing the slit area inlet against the flow stream. Based on the simulation results, even if the probe is misplaced, the effect on the measurements is still insignificant. *In-situ* measurements carried out in a laboratory set up installed in the injection tube of a drilling machine support the simulation results, since no segregation effect related to the measurement system was observed. In addition to the study, the possibility of bacteria attachment on the internal glass walls of the probe was evaluated and it was found that when the flow velocity is large enough to produce a wall shear stress of about 3-5 Pa the bacterial contamination may be avoided. Changes in the probe geometry are proposed in order to attain an isokinetic condition for the flow around and inside the probe, resulting in a higher wall shear stress for lower inlet flow velocities. An additional study was performed using a tracking particle model to understand the relevance of the individual particles behavior under different flow conditions. The results do not indicate any significant effect on the measurements inside the probe, although additional studies should be carried out in this topic by considering a population balance model for the oil droplets.

Keywords: oil-in-water emulsion flow, computational fluid dynamics, multiphase flow.

RESUMO

O presente trabalho tem como objetivo o estudo do comportamento do escoamento de uma emulsão do tipo óleo - em - água que flui no interior de câmara/duto de medição e que tem como obstáculo em seu caminho uma sonda de um sensor óptico, sensor óptico este que deve avaliar em tempo real a estabilidade da emulsão onde esta inserido. A emulsão é constituída por um fluido de corte para usinagem, com gotículas de óleo de diâmetro variando de 100 nanômetros para 100 micrometros. A sonda utilizada junto ao espectrômetro de luz UV- Vis está de acordo com o conceito proposto no projeto de pesquisa chamado EPM (Emulsion Process Monitor in Metalworking Fluid), realizado no âmbito do programa BRAGECRIM entre a Universidade de São Paulo e a Universidade de Bremen. Este estudo baseia-se na simulação numérica das interações entre a emulsão e o sistema de medição proposto, utilizando técnicas de Fluido Dinâmica Computacional (CFD), e tem por objetivo avaliar os efeitos da geometria da sonda, a sua posição em relação ao campo do escoamento, e propriedades do fluido, em especial as propriedades a serem medidas pelo espectrômetro. Tais efeitos estão correlacionadas com alterações na concentração de gotas e a segregação ou o tamanho das gotas dentro da câmara de medição da sonda óptica, o que pode causar mudanças nas leituras de intensidade de luz difusa. Efeitos de segregação devido a perturbações do escoamento em torno da sonda podem ser negligenciados, em condições normais de medição, com a sonda voltada para frente e sua área de entrada contra a corrente do escoamento. Com base nos resultados de simulação, mesmo que a sonda seja deslocada, o efeito sobre as medições ainda é insignificante. Medições foram efetuadas em laboratório e também foram realizadas medições in-situ utilizando um adaptador de medição acoplado diretamente no tubo de injeção de fluido de corte da máquina de perfuração, estes testes foram feitos para de validar os resultados obtidos por simulação, uma vez que não se observou qualquer efeito de segregação relacionada com o sistema de medição. Além disso, foi acrescentada ao estudo, a possibilidade de fixação de bactérias nas paredes de vidro internas da sonda e verificou-se que quando a velocidade de escoamento é suficientemente grande para produzir uma tensão de cisalhamento de cerca de 3-5 Pa a fixação de bacteriana pode ser evitado .Aproveitando os resultado do estudo para prevenção

de contaminação por bactéria, mudanças na geometria da sonda foram propostas a fim de atingir uma condição isocinética para o escoamento ao redor e dentro da sonda , resultando em uma maior tensão de cisalhamento para baixas velocidades de fluxo de entrada. Por fim um estudo adicional foi realizado utilizando um modelo de rastreamento de partículas para compreender a relevância do comportamento individual de cada partícula no escoamento da emulsão. Os resultados não indicam qualquer efeito significativo sobre as medições no interior da sonda, embora estudos adicionais devam ser realizados neste tópico , considerando um modelo de balanço populacional para as gotículas de óleo .

Palavras-chave: escoamento de emulsão de óleo em água, fluido dinâmica computacional, escoamento multifásico.

ABBREVIATIONS

CFD	Computational Fluid Dynamics
EPM	Emulsion Process Monitor in Metalworking Processes
DNS	Direct Numerical Simulation
DPE	Dispersed Phase Element
RANS	Reynolds Averages Equations
PVC	Polyvinyl chloride
MWF	Metal Working Fluid

SYMBOLS

α	phase fraction
U	velocity
p	pressure
ν^{eff}	effective viscous stress accounting for turbulence
ν_t	turbulent stress
ν	viscous stress
$\frac{S_\phi}{\rho_\phi}$	momentum transfer, describes the interfacial forces acting on phase α due to the presence of other phases
F_D	drag force

u	velocity
C_D	The drag coefficient
F_L	lift force
C_L	lift coefficient
F_{VM}	virtual mass force
C_{VM}	virtual mass force coefficient
ρ	density
x_{pi}^n	particle displacement
v_p	particle velocity
m_p	particle mass
F_{all}	sum of all forces acting on the particle
v_f	continuous fluid velocity
v_p^o	velocity at the starting time step
F_B	buoyancy force due the gravity
F_R	force due the domain rotation, both centripetal and Coriolis forces
F_p	pressure gradient force
\bar{v}_f	mean fluid velocity
v'_f	velocity random velocity fluctuation due to turbulence
τ_e	eddy life time

l_e	eddy length
Γ	normally distributed random number which accounts for the randomness of turbulence about a mean value
k	local kinetic energy
C_k	turbulence constant
ϵ	local dissipation rate
σ	applied shear rate
τ	wall shear stress
μ	absolute viscosity of the fluid
ω	modified dissipation energy
C_μ	parameter for the model and has a value of 0.09
u^+	dimensionless velocity
y^+	dimensionless distance
E_τ	roughness parameter
ϑ	viscosity ratio
Ca	capillary number
μ_d	droplet viscosity
μ_m	matrix viscosity
γ	interfacial tension between the drop and the matrix
We	Weber number

G	velocities gradient
η_m	shear viscosity of the Newtonian matrix
We_{cr}	critical Weber number
On	Ohnesorge number
N_{ij}	number of collisions per unit time per unit volume between the two classes of particles
$\beta(v_i, v_j)$	collision frequency function
a_i	radius
V_{Tij}	antiparticle potential between particles I and j
R_{ij}	sum of $R_{ij} = (a_i + a_j)$
ϵ_d	energy dissipation per unit mass of fluid
α_s	correction coefficient for the droplet collision frequency
p''	modified pressure
S_{M_i}	sum of the forces acting on the body
$(\overline{u_i u_j})$	contribution of the fluctuating Reynolds stresses
P_{ij}	shear
$P_{ij,b}$	buoyancy turbulence production
Φ_{ij}	pressure strain tensor
C_S	Reynolds Stress model constant
β	expansion coefficient from the Boussinesq buoyancy model

b_i	Buoyancy
a_{ij}	anisotropy tensor
S_{ij}	mean strain rate tensor
Ω_{ij}	vorticity tensor

FIGURES LIST

Figure 1: Emulsion structure (Sander, 2012).....	12
Figure 2: Illustration of the emulsion destabilization process (Mollet & Grubenmann, 2000)	14
Figure 3: Illustrative image of binary droplet coalescence phases.(Wang, Gong, Ngan, & Angeli, 2009)	16
Figure 4: Plexiglas Channel sketch	23
Figure 5: Dimensions of the probe	24
Figure 6 Plexiglas channel setup.....	25
Figure 7: Nozzle adapter at the Hermle U 630 T (milling machine, conc. = 5 v%)	26
Figure 8: Dimensions of the probe	28
Figure 9: Representative sketches of the probe, general and side views.....	31
Figure 10: Geometry improvement in the probe construction.....	32
Figure 11: Grid sensitivity study, for the Plexiglas channel	33
Figure 12: Grid sensitivity study, nozzle geometry	34
Figure 13: Time dependent concentration of particles of 100 nm size inside the measurement area	35
Figure 14: Time averaged concentration ratio inside the probe slit for different particle sizes.	36
Figure 15: Oil Concentration Ratio vs. Flow Velocity, simulations for particle diameter of 10 microns.....	37
Figure 16: Oil Concentration Ratio vs. Flow Velocity, used variables, inlet 3m/s and 10 microns of droplet diameter	39
Figure 17: Oil Concentration Fraction, variables; inlet 3m/s and 10 microns of droplet diameter	39
Figure 18: Oil volume-fraction measurement inside the channel, variables, inlet 3m/s and 10 microns of droplet diameter	40
Figure 19: Oil Concentration Fraction, variables; inlet 3m/s and 50 microns of droplet diameter	41
Figure 20: Oil volume-fraction measurement inside the channel, variables, inlet 3m/s and 50 microns of droplet diameter	41
Figure 21: Oil Concentration Fraction, variables; inlet 3m/s and 80 microns of droplet diameter	42

Figure 22: Oil volume-fraction measurement inside the channel, variables, inlet 3m/s and 80 microns of droplet diameter	42
Figure 23: Oil Concentration Fraction; variables; inlet 3m/s and 100 microns of droplet diameter	43
Figure 24: Oil volume-fraction measurement inside the channel, variables, inlet 3m/s and 100 microns of droplet diameter	43
Figure 25: Velocity profile, nozzle adapter, variables; inlet 3m/s and 10 microns of droplet diameter	44
Figure 26: Oil Concentration Fraction; variables, inlet 3m/s and 10 microns of droplet diameter	45
Figure 27: Oil volume-fraction measurement inside the nozzle, variables; inlet 3m/s and 50 microns of droplet diameter	45
Figure 28: Velocity profile, position sensitivity study. Variables; inlet 3m/s and 10 microns of droplet diameter	46
Figure 29: Oil volume-fraction measurement inside the sensor for 45° rotation . Variables; inlet 3m/s and 10 microns of droplet diameter	47
Figure 30: Oil Concentration Fraction for a probe rotation of 45°, variables; inlet 3m/s and 10 microns of droplet diameter	47
Figure 31: Oil Concentration Fraction for a probe rotation of 45°, variables; inlet 3m/s and 50 microns of droplet diameter	48
Figure 32: Oil volume-fraction measurement inside the channel for a 45° rotation Variables; inlet 3m/s and 50 microns of droplet diameter	49
Figure 33 Oil volume-fraction measurements inside the channel for 45° rotation Variables; inlet 3m/s and 80 microns of droplet diameter	49
Figure 34: Oil Concentration Fraction for the probe rotation of 45°, variables; inlet 3m/s and 80 microns of droplet diameter	50
Figure 35: Oil volume-fraction measurement inside the channel for 45° rotation Variables; inlet 3m/s and 100 microns of droplet diameter	51
Figure 36: Oil volume fraction for 45° rotation of the probe , variables; inlet 3m/s and 100 microns of droplet diameter	51
Figure 37: Velocity profile, for 90° sensitivity study	52
Figure 38: Oil volume-fraction inside the probe measurement channel for 90° rotation. Variables; inlet 3m/s and 10 microns of droplet diameter fraction	52
Figure 39: Oil Concentration fraction for 90°probe rotation , variables; inlet 3m/s and 10 microns of droplet diameter	53
Figure 40: Oil Concentration Fraction for the probe rotation study, variables; inlet 3m/s and 50 microns of droplet diameter	54

Figure 41: Oil volume-fraction measurement inside the channel form rotation study 90° Variables; inlet 3m/s and 50 microns of droplet diameter	54
Figure 42: Oil Concentration Fraction form the probe rotation study 90°, variables; inlet 3m/s and 80 microns of droplet diameter.....	55
Figure 43: Oil volume-fraction measurement inside the channel form rotation study 90° Variables; inlet 3m/s and 80 microns of droplet diameter	55
Figure 44: Oil Concentration Fraction form the probe rotation study 90°, variables; inlet 3m/s and 100 microns of droplet diameter.....	56
Figure 45: Oil volume-fraction measurement inside the channel form rotation study 90° Variables; inlet 3m/s and 100 microns of droplet diameter	56
Figure 46: Inside geometry of the probe.....	58
Figure 47: Wall shear stress variation inside the probe	59
Figure 48: Wall shear stress inside the probe	59
Figure 49: Representative sketch for the line inside the probe where the measurement is made.....	60
Figure 50: Flow velocity profiles for different probe constructions, given the slit inlet angle θ , with initial flow velocity of 0.03m/s.	61
Figure 51: Flow velocity profiles for different probe construction, given the slit inlet angle θ , with initial flow velocity of 3 m/s.	61
Figure 52: Oil shear stress rate for different inlet geometries, for an initial flow velocity of 0.03 m/s.....	62
Figure 53: Concentration inside the probe vs. geometry change	63
Figure 54: Plexiglas measurement areas of the particle tracking model	64
Figure 55: Measurement area inside the probe slit chamber	65
Figure 56: Concentration ratio vs. the number of injection position of oil droplets, results from the k-w model	65
Figure 57: Velocity profile vs. Two-phase flow model, inside Probe's geometry inlet	66
Figure 58: Oil. Volume Fraction profile vs. Two-phase flow model, inside Probe's geometry inlet.....	67
Figure 59: Concentration ratio inside a channel with a long path after the probe	68
Figure 60: Turbulence Eddy Dissipation ($m^2 s^{-3}$) along with the Plexiglas Channel...	69
Figure 61: Velocity vector along the Plexiglas channel, for Euler Lagrange simulation and k- ω trubulence model	70
Figure 62: Spectrometer charts, Volume of oil 1%	72

Figure 63: Spectrometer charts, Volume of oil 2%	72
Figure 64: Spectrometer charts, Volume of oil 4%	73
Figure 65: Spectrometer charts, Volume of oil 5%	73
Figure 66: Spectrometer charts, Volume of oil 10%	73
Figure 67: Spectrometer charts from various oil concentrations and fixed flow velocity 0.271(m/s)	74
Figure 68: Spectrometer charts from the In situ measurement (26.07.2012)	75
Figure 69: Spectrometer charts from the In situ measurement (30.07.2012)	75
Figure 70: Geometry improvement.....	78

TABLE LIST

Table 1: Assumptions used in the coagulation model	19
Table 2: Process variables used in the experimental facility	25
Table 3: Measuring instruments and devices	26
Table 4: Changes in the probe construction	32
Table 5: Concentration ratio inside the volume of the probe slit area	67

TABLE OF CONTENTS

FICHA CATALOGRÁFICA	4
1. INTRODUCTION.....	1
2 STATE OF THE ART	4
2.1 Multiphase flow	4
2.2 CFD Modeling	6
2.2.1 <i>Modeling Euler-Euler multiphase flow</i>	6
2.2.2 <i>Modeling Euler-Lagrange multiphase flow</i>	8
2.3 Emulsions/ Metal working fluids	12
2.4 Droplet coalescence and break up problems	14
2.5 Bacteria Contamination	21
3 METHODS AND METHODOLOGIES	23
3.1 Test descriptions, Channel	23
3.2. Test descriptions, Nozzle	26
3.3 Mesh generation	27
3.4 General Case system	29
3.5 Study of geometry improvements	31
4. RESULTS / DISCUSSION.....	33
4.1 Grid sensitivity study	33
4.2 Segregation effects	34
4.2.1 <i>Effects of segregation inside the slit area of the probe</i>	37
4.2.2 <i>Study on the placement of the probe</i>	46
4.3 Coagulation and Break up effects	57
4.4 Bacteria adhesion	58
4.5 Changes in the probe Geometry	60
4.6 Comparison between Euler-Euler and Euler-Lagrange models discretization	63
5. COMPARATIVE ANALYSIS: SIMULATIONS VS. EXPERIMENTS	71
5.1 In-situ Measurements at the Plexiglas channel	71
5.2 In-situ Measurements using the nozzle adapter directly at the drilling machine	74
6. CONCLUSIONS	76
7. FUTURE WORK.....	78
REFERENCES.....	79

1. INTRODUCTION

Emulsions characterize an essential constituent in advanced applications in the industry. Milk, margarine and salad dressing from the food industry are among these liquid-liquid dispersions as well as coatings, cleaning agents, cosmetics or metal working fluids. Nevertheless, there are only a few ways to determine whether the dispersion is stable or can break and in many cases the test is performed by human using the sense like vision touch and smell, and even though the precision of the detection can vary with the experience of the worker, the methods at least place this person in a hazard situation.

This is why new detection methods must be found for the growing market of 1.2 Million t/a emulsions (Kissler, 2012). One of these methods deals with the particle droplet size distribution. This physical parameter is directly linked to the quality and physical stability of an emulsion because of its influence on the free interactive surface. Therefore the emulsifiers play a important role to maintain the emulsion Stability, although many different events may cause the emulsion to break, at the present work the bacteria contamination will be taken in account. Not only because, bacteria consume the emulsifier, which is important to keep a small mean diameter, but also the bacteria contamination can be prejudicial to the measurement equipment itself, since once bacteria is present at the emulsion it can attached into the probe inside walls and end up interfering with the measurements

It is proven that turbidity spectroscopy is able to assess the stability of metal working fluids based on changes of the droplet size distribution (Deluhery & Rajagopalan, 2005). For non-invasive in-situ measurements of the multiphase fluid a dip side probe should be installed directly into the pipeline of a cutting machine. The roles of concentration differences of the dispersed oil phase, coalescence effects between droplets and bacterial contamination are investigated while the flow around and through the probe is analyzed.

This work was developed within the context of the EPM (Emulsion Project Monitor) project in the Brazilian German Collaborative Research Initiative in Manufacturing Technology (BRAGECRIM) supported by the Deutsche Forschungsgemeinschaft (DFG) and the Brazilian Coordenação de Aperfeiçoamento de Pessoal de Nível Superior (CAPES)..

Thus, a main task of this study is the investigation of the multiphase flow through a probe by computational fluid dynamics using the CFD tool CFX.

Finally it is important to state that since the work performed in the present study is part of a project involving a multitask and multidisciplinary group, the present study takes as a starting point previous studies elaborated in the project. Thus, the master thesis work developed by Sören Sander (Sander, 2012), was used as a starting point reference to the CFD simulation in this work.

The structure of this study is described below.

Work Structure

- Chapter 1: presents a brief introduction to the context of the study.
- Chapter 2 is divided into four main parts with a literature review citing the relevant works and research that were useful to the present work.
 - Chapter 2.2 presents a review on CFD modeling and simulation
 - Chapter 2.3 presents a short review about emulsions and Metal Working Fluids (MWF).
 - Chapter 2.4 presents an insight of the techniques used to predict the Coalescence and Break up of oil droplets in water dispersions.
 - Chapter 2.5 is a summary of literature concerning bacterial deposition and how to remove or prevent that deposition in systems using MWF.
- Chapter 3 is divided into two main subjects the set up condition and other consideration to both experimental work and CFD simulation.
 - The chapter 3.1 describes the work performed in laboratory, where the spectrophotometer was placed at a Plexiglas channel.
 - The chapter 3.2 presents the details form the in situ measurements, where the spectrophotometer was placed direct at the Drilling machine, be using a small nozzle at the emulsion injection pipe, in which the probe could be fixed.
 - Chapters 3.3 to 3.5 describe the CFD modeling, the basic parameters used, methodologies used in the two phase flow model and the turbulence model used.
- Chapters 4 presents results and discussion

- Chapters 4.1 and 4.2 brings a discussion about the coalescence and break up of oil droplets due to the flow behavior and it can be compared with the previous work results from the Sören Sander master Thesis where it was used the openFOAM as a tool to perform the CFD simulation, adding the probe sensitivity study about the position against the fluid flow.
- Chapter 4.3 brings a discussion about the coalescence and break up of oil droplets due to the flow behavior.
- Chapter 4.4 shows the results concerning the hypothesis of bacterial contamination and if the measurement system set up is able to prevent or not bacteria deposition on the inside probe wall.
- Chapter 4.5 the geometry improvements proposed to the probe geometry during the experiments to prove a isokinetic condition to the flow around and inside the probe.
- Chapter 4.6 brings the study performed using the particle tracking modeling to better understand the droplets behavior in the emulsion along the path through the measurement system.
- Chapter 5 brings the results of the experimental work performed at the facilities of the Universität Bremen, in Germany.
 - Chapter 5.1 shows the results of the laboratory work made with a controlled system, where the spectrometer measurements were carried out inside a flow channel.
 - Chapter 5.2 shows the experimental results with the spectrophotometer placed in the injection tube of a drilling machine used at the metalworking workshop in the Universität Bremen
- Conclusions
- Future work proposed for the project continuation.

2 STATE OF THE ART

Multiphase flow simulations have attracted a great deal of research due to the various engineering applications. Some of these studies (Launder & Spalding, 1974), Silva, Damian, & Lage, 2008 and Rusche, 2002 have been used as a basis for the present study. Although these previous studies provide a good overview for multiphase flow simulation, almost nothing could be found about multiphase flow around and inside objects with a defined geometry, such as a spectrophotometer probe. However, much can be found about flow around a circular cylinder, a condition that can be adapted to the present case by changing the geometry to that of the probe immersed in metal working fluid.

Among the various researchers the work of Williamson, 1997, with his overview published in 1997 regarding the advances on vortex dynamics in bluff body wakes can be highlighted. The author points out the experiments of (Gerrard, 1978), (Hama, Long, & Hegarty, 1957), (Cai & Wallis, 1993), (Shih, Wang, Coles, & Roshko, 1993), (Berger & Wille, 1972).

The work by Williamson cites a large number of studies about turbulent flows around a bluff body. In the work by (Prasad & Williamson, 1997) the authors demonstrate the effect of the cylinder wake at moderately high Reynolds numbers, $200 < Re < 10000$.

Another source of information regarding the flow around a cylinder is the two-volume book by “ (Zdravkovich, 1997), which provides a large amount of technical data on applied mathematics and physics involved in fluid dynamics. In this book a single class of bluff bodies is taken into consideration, only: the one with circular section.

2.1 Multiphase flow

Any numerical methodology is formulated by models and solution procedures (Rusche, 2002). Models are a mathematical representation, for example, a set of equations representing a physical or chemical process that it is intended to predict.

Since the models usually neglect the less important phenomena, the solution procedure provides approximate numerical results, based on the model equations.

Most of the two-phase flow models are represented in an engineering point of view by the Navier-Stokes equations, considering Newtonian law for viscosity and an equation of state. Usually heat and mass transfer, along with phase changes and chemical reactions are not considered in these studies. The description is general which means that with the same set of equation it should be able to represent many particular flow regimes: e.g. laminar or turbulent, and dispersed or stratified, but not just one of them.

At this point it is possible to achieve a numerical solution by Direct Numerical Simulation (DNS), where the Navier-Stokes equations are applied without additional manipulation and the interface topology is considered part of solution. DNS simulation divides the geometrical domain into small volumes, with the aim of determining a broad range of temporal and spatial scales. These scales are associated with the topology of interface for example the Dispersed Phase Element (DPE), or the fluid motion, where eddies encountered in the turbulent motion are displayed. Although a complete resolution is accomplished, resolving these scales is too expensive computationally and involves long execution time. Another modeling approach is the large eddy simulation, recommended for high Reynolds numbers, but since it is a method similar to the DNS, it is very much computational demanding, and it was not explored as an option in the present study.

Perhaps the faster way to performing a simulation of studied case consist on the Reynolds Average Equations (RANS). This model assumes that large volumes can be described by average flow parameters. What really is done is that the transport equations are modified by introducing average and fluctuating components. The idea behind it is that looking at time scales much larger than the time scales of turbulent fluctuation, the turbulent flow can be said to exhibit average characteristics, with an additional time varying fluctuating component. Thus, the equations represent the mean flow quantities only, while modeling the turbulence effects without a need for resolution of the turbulent fluctuations. All the scales of turbulence field are modeled.

Simulation of the RANS equations greatly reduces the computational effort compared to a Direct Numerical Simulation and is generally adopted for practical engineering calculations. However, the averaging procedure introduces additional

unknown terms containing products of the fluctuating quantities, which act like additional stresses in the fluid. These terms, called ‘turbulent’ or ‘Reynolds’ stresses, are difficult to determine directly and so become further unknowns.

The Reynolds stresses need to be modeled by additional equations of known quantities in order to achieve “closure.” Closure implies that there is a sufficient number of equations for all the unknowns, including the Reynolds-Stress tensor resulting from the averaging procedure. The equations used to close the system define the type of turbulence model.

2.2 CFD Modeling

2.2.1 Modeling Euler-Euler multiphase flow

Two distinct multiphase models are usually applied in CFD solvers to describe the multiphase flow behavior, Eulerian-Eulerian model and Eulerian-Lagrangian model.

The Euler-Lagrange model or dispersed PDE model assumes that for two phase flow one phase is the dispersed and the other the continuous one. The dispersed phase is represented by an individual PDEs, which is tracked through the flow domain by the appropriate equation of motion. The equation of motion is the conservation equation of momentum expressed in the Lagrangian formulation, in which the dependent variables are the properties of material particles that are followed in their motion. On the other hand, the conservation equations for the continuous phase are expressed in the Eulerian frame, where the fluid properties are considered as functions of space and time in an inertial frame of reference. Even though the Euler-Lagrange model is able to track each droplet in the flow, that same ability turns the model time demanding and thus only a limited number of droplets can be tracked. This is the reason why, in the present study, the Euler –Euler approach was used, where each phase is treated as a continuum, one interpenetrating each other, and is represented by averaged conservation equations. The averaging process introduces the phase fraction into the equation set, which is defined as the probability that a certain phase is present at a certain point in space and time.

Governing equations: the set of equations solved by the CFD solvers are the unsteady Navier-Stokes for a phase φ given below.

$$\frac{\delta \alpha_{\varphi} U_{\varphi}}{\delta t} + \nabla (\alpha_{\varphi} U_{\varphi} U_{\varphi}) + \nabla (\alpha_{\varphi} v_{\varphi}^{eff}) = - \frac{\alpha_{\varphi}}{\rho_{\varphi}} \nabla p + \alpha_{\varphi} g + \frac{S_{\varphi}}{\rho_{\varphi}} \quad (1)$$

where: α is the phase fraction, U is the velocity, p is the pressure.

v^{eff} is the effective viscous stress accounting for turbulence.

$$v^{eff} = v_t + v \quad (2)$$

v_t is the turbulent stress and v is viscous stress

$\frac{S_{\varphi}}{\rho_{\varphi}}$ is the momentum transfer, which describes the interfacial forces acting on phase α due to the presence of other phases.

As mentioned, the interphase momentum transfer occurs due to the interfacial forces acting on each phase α , due to the interaction with another phase β , and can be calculated as a sum of several independent physical effects: in this study three forces are considered; drag, lift and virtual mass force.

All forces can be modeled using empirical relations and theoretical models (Auton, Hunt, & Prud'Homme, 2006). The drag force is expressed by:

$$F_D = C_D A \frac{1}{2} \rho_c (u_c - u_d) |u_c - u_d| \quad (3)$$

where ρ is the density; u , velocity; suffixes c and d denote the continuous and dispersed phases; and A is the projected area of a particle in its flow direction. The drag coefficient, C_D , is obtained by a correlation and the method used to calculate it is shown in equation 33.

While the drag force moves the particles in negative flow direction, the lift force is equal to the force perpendicular to the flow. A derivation can be found in (Laurien & Herbert, 2009).

$$F_L = \frac{1}{2} \rho U^2 C_L A \quad (4)$$

In this term the lift coefficient C_L must be identified. The last force included in the solver defines the force induced by acceleration of the particles. It is known as the virtual mass force

$$F_{VM} = C_{VM} \rho_c v_p \left(\frac{\delta u_c}{\delta t} - \frac{\delta u_p}{\delta t} \right) \quad (5)$$

where c and p indicate the continuous and particulate phase, respectively. All coefficients must be calculated dependent on the particle form, concentration and the flow conditions.

2.2.2 Modeling Euler-Lagrange multiphase flow

The Euler Lagrange approach is used to formulate the model designated in the CFX solver as particle transport model. The model uses the discretization of Euler – Lagrange theory to predict the multiphase behavior, in particular the dispersed phase behavior by tracking one or a group of particles through the flow in a Lagrangian way, rather than being modeled as an extra Eulerian phase.

Within the particle model, components present in the dispersed phase like drops, bubbles or solid particles are represented by a small number of particles through the continuum fluid.

The treatment of the Lagrangian tracking model involves the integration of the particles path through the discretized domain. Each particle is tracked individually from their injection point of origin to the point where they leave the domain or another imposed criterion is met. In addition, the particles are injected in trains in order to obtain an average of all particle tracks and to generate the source terms to the fluid mass, momentum and energy. Finally, since the particle is tracked from the injection point to the final destination, the tracking procedure is applicable to steady state flow analysis. In the text that follows the methodology to track the particles is described.

The particle displacement is calculated using forward Euler, and is related to the particle velocity. Integration over the time step, δt , according to equation (9):

$$\frac{dx_p}{dt} = v_p \quad (6)$$

The particle displacement is given by:

$$x_{pi}^n = x_{pi}^o + v_{pi}^o \delta t \quad (7)$$

where the superscripts o and n refer to old and new values respectively, and v_{pi}^o is the initial particle velocity.

In the forward integration the particle velocity at the start of the time step is assumed to prevail over the entire step. Then at the end of the time step the analytical solution from the particle momentum equation is used to calculate the new particle velocity:

$$m_p \frac{dv_p}{dt} = F_{all} \quad (8)$$

where F_{all} is the sum of all forces acting on the particle. The analytical solution of the particle momentum equation is given by equation (9):

$$v_p = v_f + (v_p^o - v_f) \exp\left(\frac{\delta t}{\tau}\right) + \tau F_{all} \left(1 - \exp\left(-\frac{\delta t}{\tau}\right)\right) \quad (9)$$

Where the v_f is the continuous fluid velocity.

The fluid properties are taken from the start of the time step. For the particle momentum, v_p^o would match the velocity at the start time step.

In order to take into account all the fluid forces on the particles, there are many variables that should be taken into consideration such as density, viscosity and velocity in the surroundings. These variables are acquired by calculating the element in which the particle is traveling, calculating the computational positions, and using

the underlying shape function of the discretization algorithm to interpolate from the particle position.

The next step to understand the particles motion through the fluid is the momentum transfer equations.

When a particle is traveling withing a continuum fluid matrix, the forces acting on the particle that affect its acceleration and trajectory are the consequence of the velocity difference between the particle and the fluid, and additionally the particle displaces the fluid in its surroundings. The equation used to estimate the particle motion was derived by Boussinesq, Oseen (Wolschin, 2013) among other authors.

$$m_p \frac{dU}{dt} = F_D + F_B + F_R + F_{VM} + F_P \quad (10)$$

The right hand side of the particle motion equation is the sum of the forces to which a particle tracking within a fluid may be submitted.

- F_D = drag force acting on the particle.
- F_B = Buoyancy force due the gravity.
- F_R = force due to the domain rotation, both centripetal and Coriolis forces.
- F_{VM} = virtual mass force or virtual added force, which is particularly important in cases like the motion of bubbles, when the displaced fluid mass exceeds the particles mass.
- F_p is the pressure gradient force. The pressure gradient force affects the particle due to the pressure gradient in the fluid surroundings and is caused by the fluid acceleration. It is only significant when the fluid density is comparable to or larger than the particle density.

Turbulence in particle tracking

The particle tracking depends on the instantaneous fluid velocity, v_f , and which depends on the flow regime, the two options given are laminar or turbulent flows.

For the laminar flow regime, v_f is equal to the mean velocity \bar{v}_f , at the surrounding fluid of the particle. This assumption suggests that for any particle of the

same shape and size injected at the same position, the trajectory is the same for any number of times the particle is injected.

But for the turbulent particle tracking, the instantaneous fluid velocity v_f is decomposed in two terms, the mean fluid velocity, \bar{v}_f , and the v random velocity fluctuation v'_f . Then the particle trajectory is not considered deterministic, which means that two identical particles injected from the same origin point at different times may not have the same path through the domain due to the random nature of the instantaneous fluid velocity, which produces the dispersion in a turbulent flow.

The model of turbulent dispersion of particles is based on the work by Gosman and Loannides (Gosman & Loannides, 1983), where they assume that a particle is always within a turbulent eddy. Once a particle has entered an eddy the fluctuating fluid velocity of that eddy is summed to the mean fluid velocity to form the instantaneous fluid velocity.

The turbulent fluid velocity v'_f is supposed to prevail providing the particle/eddy interaction if the time is less than the life time of the eddy and the shift of the particle is smaller than the eddy length. If only one condition is not matched the particle is assumed to enter a new eddy with new characteristic fluctuating velocity.

The eddy characteristic turbulent velocity v'_f , the eddy life time and length respectively τ_e and l_e , and they are calculated based on the flow turbulence properties.

$$v'_f = \Gamma \left(\frac{2k}{3} \right)^{0.5} \quad (11)$$

$$l_e = \frac{C_k^{\frac{3}{4}} k^{\frac{3}{2}}}{\epsilon} \quad (12)$$

$$\tau_e = \frac{l_e}{\left(\frac{2k}{3} \right)^{\frac{1}{2}}} \quad (13)$$

where the k and ϵ are the local kinetic energy and dissipation, respectively, and C_k is a turbulence constant.

The term Γ is a normally distributed random number which accounts for the randomness of turbulence about a mean value. As a consequence, each component of the fluctuating fluid velocity (u' , v' , w') may have a different value in each eddy.

2.3 Emulsions/ Metal working fluids

Emulsions are systems consisting of at least two immiscible liquid phases, one of which exists in the form of particulates and is dispersed in the other. Usually these phases are water and oil. Water-in-oil systems (w/o) consist of a continuous oil phase with dispersed water droplets. In oil-in-water systems (o/w) the aqueous phase is the continuous phase and the oil phase is the dispersed phase. Usually both phases separate from each other to achieve thermodynamic stability. In order to minimize this energy both liquids try to support less contact area in case of constant temperature and pressure (STEPHAN ET AL. (2005)). So emulsifiers are added to stabilize the system by either steric (nonionic) or electrostatic (ionic) barriers. These substances are polymers with at least a lipophilic and a hydrophilic ending and can adhere to the droplet surface, as seen in Figure 1 (SOREN (2012)).

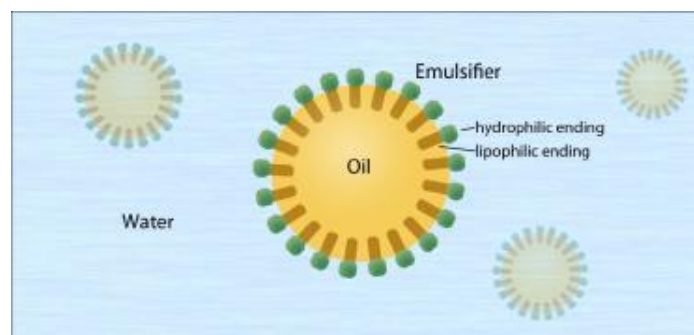


Figure 1: Emulsion structure (Sander, 2012)

The mixture must be stirred so that the emulsifiers can be transported to the droplet surface. In most of the cases the dispersed compound is not self-emulsifying. This means that the emulsifier automatically splits the droplets into smaller ones to increase the surface. The only other option is that the droplets must be produced by mechanical shredding (also see KARBSTEIN & SCHUBERT (1995)). The type of

emulsion obtained is defined by the separation emulsifiers. So emulsifiers with hydrophilic groups lead to the formation of an o/w system, likewise w/o mixtures are formed if the majority of groups are lipophilic.

By mixing, destabilization of the emulsion can take place and different mechanisms can affect the state of an emulsion, which is why semi-stability in terms of droplet size and droplet size distribution is usually a time-dependent quantity.

Microorganisms (microbiological contamination), and external influences such as UV light or reactions between individual components (chemical stability) (Schubert, 2005) result in the instability or "breaking" of an emulsion, which can lead to the complete separation of the phases due to the coalescence of drops of the dispersed phase. In addition to the droplet coalescence, according to the literature (Mollet & Grubenmann, 2000) and (Köhler, 2010) other processes, including aggregation, Ostwald ripening, sedimentation and creaming can take place. Aggregation refers to the convergence of several droplets forming a "grape" (Schubert, 2005). It can cause local concentration differences within the emulsion due to the change of the droplet size distribution and often resulting in coalescence. While aggregation is a reversible process, which can be reversed by means of mechanical forces caused by stirring or shaking, coalescence is irreversible. Ostwald ripening refers to the mass diffusion of several small droplets that ceases to exist and their mass is added to few larger drops and thus represents a contrast to the other mechanism. The aggregation should be added is the possibility of the presence aggregated droplets over a long period without causing coalescence (Mollet & Grubenmann, 2000). Figure 2 shows schematically the above operations at for example occurring sequences represent.

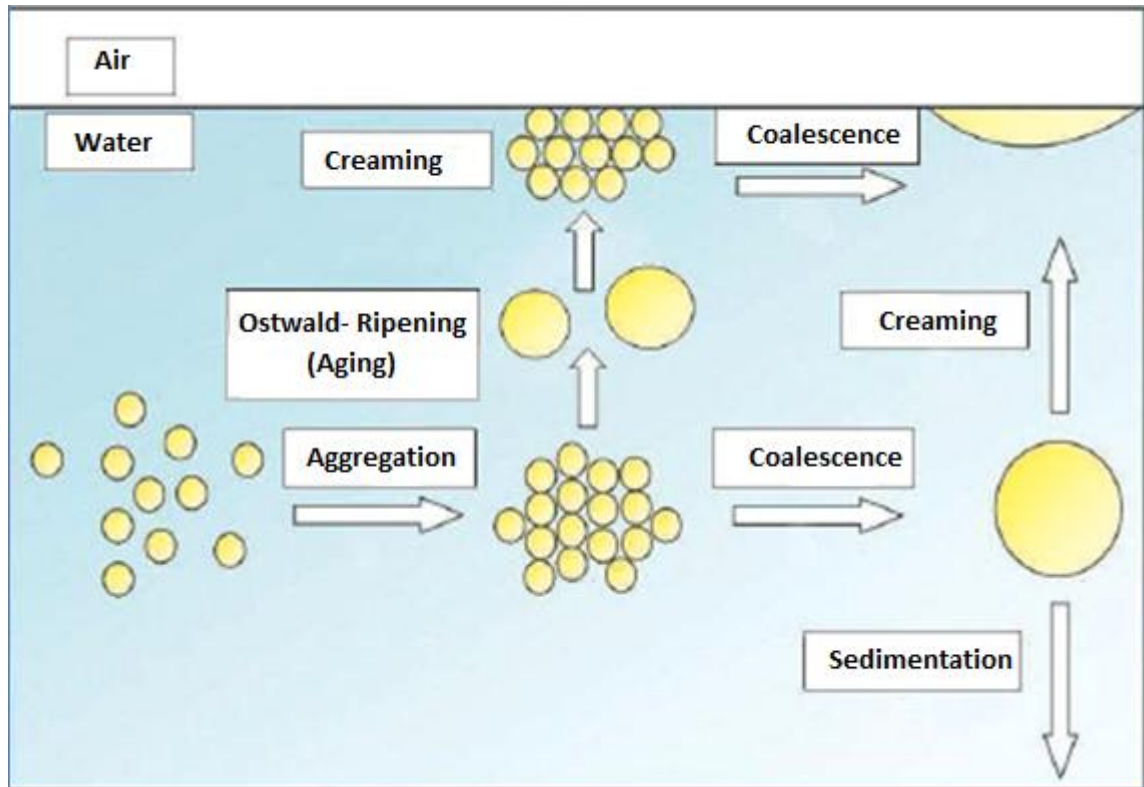


Figure 2: Illustration of the emulsion destabilization process (Mollet & Grubenmann, 2000)

2.4 Droplet coalescence and break up problems

According to Binks (Binks, 1998) emulsion stability is a kinetic concept; therefore any stable emulsion is expected to show almost no variation in number of droplets, size distribution and spatial arrangement of the drops within the experimental time scale.

The destabilization processes that have been taken in consideration in this study include droplet break up, that can result from the especial flow behavior at the measurement system, and droplet coalescence that can result from flow characteristics or can be caused by the natural repulsive effect from parts at the dispersion. Without surfactant, coalescence causes oil and water mixtures to separate into oil and water within seconds.

Concerning the deformation and break-up of Newtonian droplets immersed in immiscible Newtonian matrix, the theme has been extensively investigated in the literature. According to (Abbassi-Sourki, Huneault, & Bousmina, 2009), one of the

first studies developed in this theme was carried out by Taylor, 1932 . He described the drop deformation with two dimensionless parameters, the viscosity ratio ϑ , and capillary number Ca defined as:

$$\vartheta = \frac{\mu_d}{\mu_m} \quad ; \quad Ca = \frac{\mu_m a \sigma}{\gamma} \quad (14)$$

where μ_d and μ_m represent the viscosities of the drop and the matrix, respectively, a denotes the initial radius of the spherical drop, σ is the applied shear rate and γ is the constant interfacial tension between the drop and the matrix.

In general a parameter used to predict the drop behavior is the Weber number.

$$We = \frac{G \eta_m d}{2\gamma} \quad (15)$$

where d is the droplet diameter, G is the velocity gradient, η_m is the shear viscosity of the Newtonian matrix and γ is the interfacial tension.

The dimensionless Weber number, presented in equation 15, presents the ratio of the external stress to the Laplace pressure, usually used to express the drop deformation. It is known that the deformation of the drop increases with We , and above a critical Weber number the drop bursts, then it breaks into smaller ones.

The work from (Tarnogrodzki, 1993), proposes an empirical relation to calculate the critical Weber number for low viscosity fluid:

$$We_{cr} = 12 (1 + 1.0770On^{1.6}) \quad (16)$$

where On is the Ohnesorge number, a parameter that does not depend on the relative velocities. It is given by the equation 17:

$$On = \frac{\mu_d}{\sqrt{\rho_d \sigma_d d}} \quad (17)$$

where the subscript d indicates the dispersed phase, further one the μ_d is the viscosity, ρ_d density, σ_d the surface tension and d is the droplet diameter.

Coalescence of emulsion is a process where two or more drops of the dispersed phase merge together forming a larger droplet, and the final stage of the coalescence would be the total separation of the emulsion into distends phases. Although the complete separation of emulsion due coalescence should not be a problem to be found at real metal work process, since the fluid is changed much earlier it can get to this stage of degradation. The coalescence is still a problem for the reason that the performance of the MWF can be decreased even during it first stages, due the changes at the droplet numbers and as well the droplet size distribution thereby affecting the original fluids proprieties i.e. of cooling and purification.

The emulsion coalescence process basically is the thinning and disruption of the liquid film between the droplets. This can happen if the emulsion droplets closely approach each other in a cream layer, in a flock, or during particle movement, i.e. like in Brownian diffusion or due to flow proprieties i.e. laminar shear or turbulent shear.

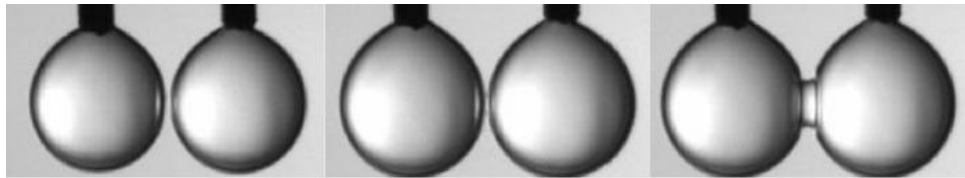


Figure 3: Illustrative image of binary droplet coalescence phases.(Wang, Gong, Ngan, & Angeli, 2009)

In the measurement system proposed in the EPM project, the fluid will be flowing inside a channel, and it is important to know if any coalescence due to particle movement can take place in the measurement area of the spectrophotometer.

The rate of coalescence can be represented by:

$$\text{Rate of coalescence} = \text{rate of collision} \times \text{coalescence efficiency}$$

According to Friedlander, (1977) the theory of coagulation is composed of two parts. The first would be a scheme for keeping count of particle collisions as a

function of the particles size distribution, in this scheme would be then incorporated the collision frequency function.

The number of collisions per unit time per unit volume between two classes of particle sizes is given by the following equation:

$$N_{ij} = \beta (v_i, v_j) n_i n_j \quad (18)$$

where v_i, v_j are the volumes of two classes of particles, and taking into consideration that all the particles are assumed to be spherical, the indices i and j are only related to the particle diameters, and $\beta (v_i, v_j)$ is the collision frequency function.

The collision frequency is then determined by the so-called mechanism of particle collision. Basically it involves all kinds of particle movement that can lead two or more particles to collide. The motion behavior of particles immersed in liquid is usually an outcome of three different forces combined: total static interaction force, the force due to the Brownian motion, and the force generated by the flow medium. Then, knowing all these forces the motion of the particle is given by the following equation.

$$m\ddot{r} = f_T + f_B + f_F \quad (19)$$

where m is the particle mass, and \ddot{r} is its acceleration.

In order to calculate the coagulation process quantitatively, f_T, f_B, f_F must be known. Although in the present study the static interaction force is not taken into consideration, since the static force is usually employed to verify the stability of the suspension, and since the MWF used in most of the studies is assumed to be fresh, it is assumed that no considerable coagulation happens due to the static force.

Further on it will be evaluated the coagulation effect due a dynamic integration. First it is known that particles can interact with each other through their Brownian motion resulting in coagulation.

Assuming, that every collision due to Brownian motion results in coagulation phenomena, named rapid coagulation, The collision frequency of the Brownian coagulation between particles of distinct sizes, i and j , is given by (Okuyama & Higashitani, 2006):

$$\beta_{(n_i n_j)} = \left[\frac{2KT}{3\mu} \right] (a_i + a_j) \left(\frac{1}{a_i} + \frac{1}{a_j} \right) \left(\int_{a_i+a_j}^{\infty} \frac{\exp\left(\frac{V_{Tij}}{kT}\right)}{r^2} dr \right)^{-1} \quad (20)$$

where a_i is the radius, n_j is the number concentration of particle j, and V_{Tij} is the antiparticle potential between particles i and j.

The second process considered is the coagulation due to the shear flow, where the collision between the particles in the flow field will happen because of their relative velocities. Collision can result in coagulation, depending on the balance between the energy of the particles given by the flow and the interparticle potential energy. (Okuyama & Higashitani, 2006) give the collision frequency as:

$$\beta_{(n_i n_j)} = \frac{4}{3} G R_{ij}^3 \quad (21)$$

where G is the velocity gradient, and $R_{ij} = (a_i + a_j)$.

The last contribution to coagulation created by a force generated by the flow is the turbulent shear. Although it is not easy to estimate the coagulation rate of particles in a turbulent flow because of the complicate flow field Saffman and Truner, 1956, derived an expression for the rapid coagulation rate in a turbulent flow without taking the hydrodynamic interaction into account. But the equation given by the Smoluchowski theory of shear coagulation can give a reasonable predication of the collision frequency due turbulent shear:

$$\beta_{(n_i n_j)} = 1.3 \left(\frac{\epsilon_d}{\nu} \right)^{\frac{1}{2}} R_{ij}^3 \quad (22)$$

where ϵ_d is the energy dissipation per unit mass of fluid and ν is the kinetic viscosity of the medium.

Considering the work of Sören (Sander, 2012), it is possible to assume under the conditions of the study here developed, the most relevant phenomenon is the coagulation due to turbulent shear, since the turbulent collision frequency has shown

to be the largest one. Therefore the equation presented by (Okuyama & Higashitani, 2006) to calculate the rate of concentration change of a particle k , considering the population balance, is adopted:

$$\frac{dn_k}{dt} = \frac{1}{2} \sum_{i=1}^{i=k-1} 1.3 \left(\frac{\epsilon_d}{\nu}\right)^{\frac{1}{2}} R_{ij}^3 n_i n_{k-1} - \sum_{i=1}^{\infty} 1.3 \left(\frac{\epsilon_d}{\nu}\right)^{\frac{1}{2}} R_{ij}^3 n_i n_k \quad (k = 1, 2, \dots, \infty) \quad (23)$$

The first term on the right-hand side represents the rate of formation of particle k by the coagulation of smaller particles and the second term the rate of disappearance due to coagulation of the particle k with others.

In order to use equation 23, the assumptions presented in Table 3 are necessary:

Table 1: Assumptions used in the coagulation model

1	R_{ij} is small in comparison with the smallest eddies of turbulence.
2	Particles move with the fluid velocity.
3	Effects of inertia and sedimentation of particles are negligible.
4	The effect of Brownian coagulation which proceeds simultaneously is negligible.
5	Flocs never break up.
6	There exists no interparticle force, and particles coagulate when they collide.
7	The collision efficiency is unity, that is the distortion of the particle trajectory by the hydrodynamic interaction between particles is negligible.

Assumptions 1, 3 and 4 are usually satisfied for colloidal dispersions or emulsion like a MWF under turbulent flow. Assumption 5 is also matched during the earlier stages of coagulation, when the flocs are still too small to break under the shear stress. But assumptions 2, 6 and 7 are not likely to be negligible. Assumptions 2 and 7 may result in a considerable error. Since the collision of particles in a turbulent fluid is also attributed to the velocity gradient of the fluid, the effect of hydrodynamic interaction will not be negligible. In addition, it was shown by (HIGASHITANI, OGAWA, HOSOKAWA, & MATSUNO, 1982) that for dispersions

where the particles are close to each other they can interact hydrodynamically due to the shear flow, and they will collide during their trajectories. Next, in opposite to the assumption 6, there exist interparticle forces between particles when the dispersion is found in an aqueous solution. Therefore it is conventionally assumed that the van der Waals-London force is the only interparticle force in rapid coagulation.

Considering the assumptions 2, 6 and 7 (Saffman & Turner, 2006) derived an expression for the rapid collision rate in a turbulent flow without taking the hydrodynamic interaction into account. In essence equation 22 was modified by adding a correction term α_s , as follows:

$$\beta_{(n_i n_j)} = 1.3\alpha_s \left(\frac{\epsilon_d}{\nu}\right)^{\frac{1}{2}} R_{ij}^3 \quad (24)$$

After determining the collision rate, the main goal of the study is to establish the collision efficiency. Whether the drops will merge together to form a bigger drop, or they just collide and distance each other again. Then, as a result of the collision frequency and collision efficiency, it is expected to calculate the population balance change of the emulsion during the time it is exposed to a process.

Considering the work from, Pinsky et al. "Collisions of Small Drops in a Turbulent Flow" (Pinsky, Khain, & Shapiro, 2007), it give the collision efficiency for cloud droplets from about 10 and 15 microns of diameter to be between 0.03 to 0.09, when exposed to a flow condition of Reynolds numbers in between 5000 to 40000 resulting in a dissipation rate from $0.001 \text{ m}^2 \text{ s}^{-3}$ to $0.1 \text{ m}^2 \text{ s}^{-3}$. Although the drops of water in clouds present in a cloud are slightly different than a dispersion of a MWF, it is interesting to see that even in dispersion where the droplets have a bigger diameter and no emulsifier is present to prevent coalescence, the collision efficiency is close to 10 %.

2.5 Bacteria Contamination

Water miscible metal working fluids fulfill several functions in manufacturing technique. During any metal working process like turning, drilling, milling, boring and grinding MWF perform cooling of the metal work piece and tool.

Although microbial contamination and degradation of water miscible MWF are widespread problems leading to functional problems and hygienic concerns, points that will not be considered in the present study. This work considers microbial contamination as a problem related to the metal working activity, by evaluating if the measurement system proposed can be affected by bacterial contamination, especially if any measurement area of the probe can be blocked by bacteria adhesion. Thus, one of the study goals is to evaluate adequate conditions to avoid bacterial contamination.

A parameter that is widely used by the European Hygienic Engineering and Design Group, EHEDG, is the wall shear stress, considered a direct flow parameter for prediction of cleanability. Based on that assumption, the only task needed is to find out the critical wall shear stress to clean a bacterial exposed surface or to avoid any adhesion of microorganisms.

First it is important to highlight how bacteria or any microorganism can stick to a surface wall. The typical kinetics of any bacterial adhesion follows a pattern, where an initial linear trajectory can be seen, followed by a leveling off to an end stage.

During the initial phase, organisms that arrive at a surface interact solely with the surface, and during this stage the affinity of the organism for the surface is a condition given to the adhesion process to take place. At later stages, when the surface is already partially covered with adhering organisms an arriving organism will have interaction with the surface, but also with the already adhered microorganisms. And thus will form a bond even harder to separate.

According to (Busscher & van der Mei, 2006) bacterial adhesion can be tested using a flow displacement system allowing to calculate the wall shear rate σ (s^{-1}) acting on adhering microorganisms, as the main source of fluid flow forces on the adhering organisms.

At a surface, fluid flow is essentially absent and flow increases with distance away from the surface. Consequently, fluid flow is slightly higher over the top of an

adhering microorganism than at its bottom, which yields a shear. The force resulting from this shear acts parallel to the surface and depends on the viscosity of the suspension and the microbial dimensions.

The wall shear rate is the main hydrodynamic force exerted by the flow on an adhering organism and is determined by the velocity gradient near the wall. The wall shear rate can be calculated from velocity profiles determined with either particle image velocimetry or numerical simulation (Busscher & van der Mei, 2006), using:

$$\sigma = \frac{dv}{dh} \quad (25)$$

where the v is the velocity in the direction of the main flow and h is the distance perpendicular to the surface.

The hydrodynamic force per unit surface area exposed to the wall shear stress rate is directed parallel to the wall and is defined as the wall shear stress τ (N.m^{-2}), which is the product of the wall shear rate with the absolute viscosity of the fluid present at the system.

$$\tau = \mu \sigma \quad (26)$$

where μ ($\text{kg.m}^{-1}.\text{s}^{-1}$)

After all, according to the literature a wall shear stress of about 3-6 Pa or higher should be enough to avoid bacteria adhesion (Jensen & Friis, 2004), and for cleaning purposes the wall shear stress values need to be in a much higher range, about 20-80 Pa (Guillemot et al., 2006).

3 METHODS AND METHODOLOGIES

Before starting the simulation of the multiphase flow through the probe, and to give a better understanding of the two different systems modelled in this study, chapters 3.1 and 3.2 present a general description of the equipment used to do the experimental measurements, both at the channel used in the laboratory and the nozzle attached directly to the cutting machine. The geometries and the process variables shown in the next two chapters are the base conditions for all the CFD simulations carried out further on.

3.1 Test descriptions, Channel

The effect of process variables on turbidity readings for the flow of oil in water emulsions was evaluated at a 560 mm long square Plexiglas channel with constant cross section, with area of 20 mm x 20 mm according to Figures 4 and 5.

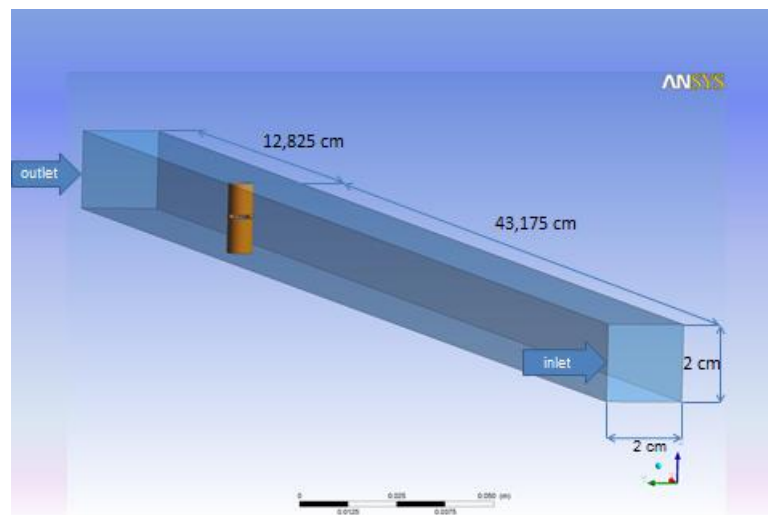


Figure 4: Plexiglas Channel sketch

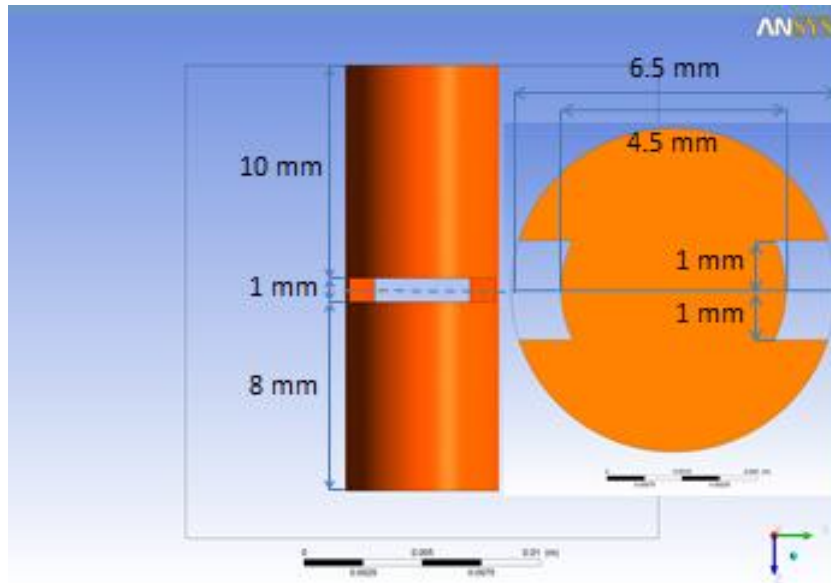


Figure 5: Dimensions of the probe

The set-up of the channel consisted of a 10 liter PVC reservoir connected directly to a centrifugal pump, pumping the emulsion through PVC flexible braided hoses to the Plexiglas channel previously described. Just before entering the emulsion in the channel there is a three-way plug valve attached to provide a recirculation system to the reservoir. The dip probe was installed at a distance of 430mm from the channel inlet, in a way that the scattering window is at the center of the channel. After the channel a volumetric flow meter and another three-way plug valve are installed. The three-way plug valve enables the recirculation of the fluid or its discharge. Figure 6 shows an flow diagram of the experimental setup.

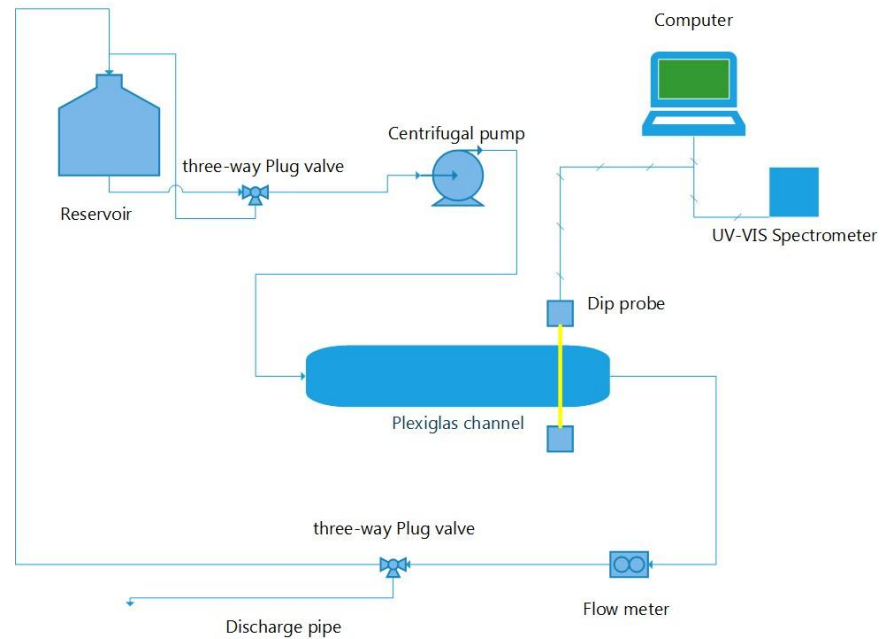


Figure 6 Plexiglas channel setup

In addition to the main setup, a frequency inverter with voltage and frequency control is implemented to the pump control system for regulation of the flow volume to investigate the effect of different flow velocities on the spectrophotometer readings. With the help of the flow meter each fluid velocity was determined. For this, the displayed voltage values based on the volume flow rate were previously calculated.

Table 2: Process variables used in the experimental facility

Nr.	Process variables	Unit	values
1	Fluid velocity	m/s	0.039; 0.078; 0.117; 0.157; 0.195; 0.231; 0.271; 1; 2; 3
2	Oil volume concentration, in volume	%	0.5; 1; 2; 3; 4; 5; 6; 10

Table 3 lists the components of the laboratory setup.

Table 3: Measuring instruments and devices

Designation	Manufacturer	Model/Features
Centrifugal Pump	Speck Pumpen	NPY-2251-MK-TOE
Light Source	Ocean Optics	DH-2000-BAL
Spectrometer	Ocean Optics	HR 2000+ES
Dip probe	Ocean Optics	T300-RT-UV-VIS

3.2. Test descriptions, Nozzle

The nozzle was adapted to be used in the machine to attach the dip probe directly before the metal working fluid outlet pipe. The first measurement was done just after the monthly refill of fluid in the machine, so the metalworking fluid was new, and this enabled to monitor the changes in the oil characteristics with time. Figure 6 shows the position of the nozzle and the dip probe in the milling machine.



Figure 7: Nozzle adapter at the Hermle U 630 T (milling machine, conc. = 5 v%)

To simplify the simulations using CFD, the nozzle was represented with its inside channel as a circular cross section pipe, with 9 mm of diameter, and the MWF velocities ranged from 0.4 to 3 m/s.

3.3 Mesh generation

For the multiphase flow simulation through the probe a mesh needed to be created for each of the geometries shown in chapters 3.1 and 3.2., and the area around the sensor was discretized into many small domains to achieve better accuracy in the areas of interest.

In order to have a fast convergence and a precise result the mesh generation has the most important role when working with CFD (Baden, Chrisochoides, Gannon, & Norman, n.d.).

In the process of mesh generating some especial characteristics were considered, for instance an optimum point between flexibility and accuracy. For the simulation made using CFX experience shows that unstructured mesh is easier to deal with, and this gives the flexibility necessary to create a good representation of the probe scattering area.

Another aspect is the viscous flow that exists near the channel walls. In order to be able to track its effects the number of cells close to the walls were set according to the wall treatment of each turbulence model. If the cells close to the wall are not big enough the wall functions do not work properly. What leads us to one of the challenges of mesh generation especially at the probe slit area where the volume needed to be divided into a very fine mesh to provide an adequate resolution..

Even after an independency study was made for the mesh, in order to ensure that the results concerning the influence of different flow velocities were reliable, for each of the velocities used in the simulations from 0.039 to 3 m/s a mesh was generated regarding the size of the first cell close to the wall. As the velocity increases the dimensionless wall distance decreases.

The dimensions of the dip probe used in the experimental setup are shown in Figure 8. The particle laden flow must enter the slit to get tracked by the light transmission sensor.

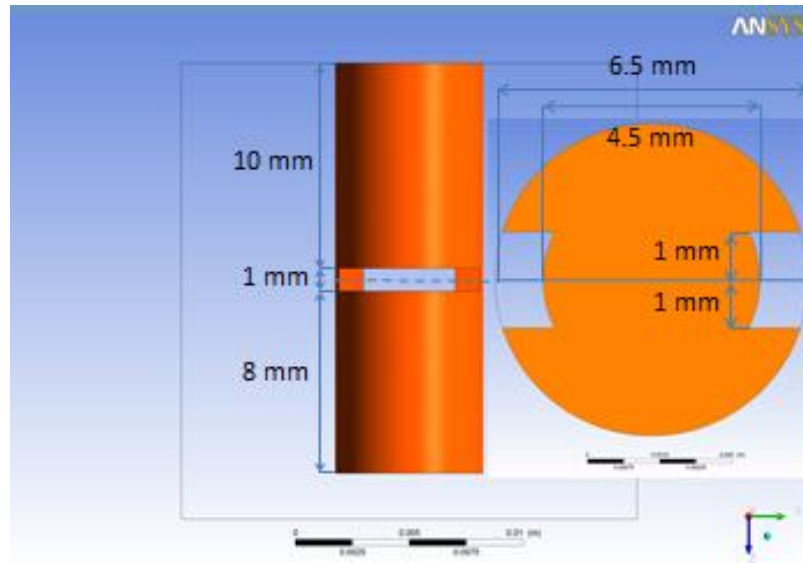


Figure 8: Dimensions of the probe

Another topic of concern in this study is the geometry of the probe itself. One of the main problems when creating the mesh is the small distance, especially when considering the probe slit. When using the $k-\omega$ model for the turbulent flow analyses, a certain wall distance needs to be satisfied. Therefore, all the meshes created, at the channel walls, have defined distances for the first cells. This way the distance from the wall is adjusted for different velocities and turbulence models. Especially when dealing with the $k-\epsilon$ model the specific distance that needs to be kept creates some problems, because inside the 1 mm slit the values for a minimum distance cannot be resolved as the length is too small. That is one of the reasons why the $k-\epsilon$ model has not been used in this study.

3.4 General Case system

At the present chapter, the consideration and coefficients used to the simulation area further detailed. A uniform velocity profile at the inflow boundary, uniform velocity for both phases and uniform particle concentration are considered, regarding that for general proposes the oil concentration at the emulsion is always 5% in volume, which is the standard concentration used at the milling machine at the workshop in University Bremen. At outflow boundary the average pressure static and the velocities at the wall were set to zero.

Some of the starting values for the turbulence models can be calculated for the inlet as follows:

for the turbulent kinetic energy:

$$k = \frac{3}{2} (uI)^2 \quad (27)$$

for the turbulent dissipation:

$$\varepsilon = C_\mu \frac{k^{\frac{3}{2}}}{l} \quad (28)$$

and for the specific dissipation rate:

$$w = \frac{\sqrt{k}}{l} \quad (29)$$

where u is velocity, I the turbulent intensity, which is usually set to 5% according to (Versteeg & Malalasekera, 2007), C_μ is the parameter for the model and has a value of 0.09 (Launder & Spalding, 1974) and l is the length scale.

It is described below that the distances from the first cell and the wall need special attention, for this wall function and dimensionless distance y^+ need to be calculated and known.

The wall function is expressed by:

$$u^+ = \frac{1}{k} \log(E y^+) \quad (30)$$

and the dimensionless wall distance is:

$$y^+ = \frac{E_\tau y}{\nu} \quad (31)$$

The wall function is applied as long as the values for the dimensionless wall distance are in the viscous layer $y^+ \geq 5$. The term E is the roughness parameter and k is the geometric constant known as Karman constant and has a value of 0.4 (Zanoun, Durst, & Nagib, 2003)

It is important to mention that considering the small dimensions of the dip probe slit area, part of the mesh will be in the viscous sub layer, where the wall distance y is proportional to the dimensionless equivalent.

And the value for y^+ is :

$$y^+ = u^+ \quad (32)$$

The y^+ values need always be taken in consideration, especially the ones at the frit cells near to the walls. The value of y^+ near to the walls should be always in agreement with the wall function limitations, therefore it is import to remember that for each model, and wall function, the y^+ has a different range, in which the mesh need to be adequate, otherwise the simulation results can not be trusted.

Secondly, the values for the viscosity and density of the water and the oil are equal to the ones at 20 °C (see Table 1 on 11 for oil and VDI WÄRMEATLAS (*VDI-Wärmeatlas*, 2006) for the values of water). Moreover, the values of the constants for the drag force C_D , the virtual mass force C_{VM} , lift C_l , and turbulent drag C_t have to be worked out.

The standard model suggests that the coefficient C_{VM} is 0.5. This value is used for instance by (Auton et al., 2006) while (Cai & Wallis, 1993) and (Wijngaarden & Jeffrey, 2006) obtained expressions dependent on the volume fraction of the dispersed phase. As the fraction is below 5 % in this work, the difference to a fixed value is insignificant and only leads to mathematical instability.

According to (Rusche, 2002) the lift coefficient C_l can be considered zero. Since in this work the particles are very small, and therefore the spherical form does not change due to the flow, the lift force is neglected and the coefficient is set to zero.

The drag force is frequently expressed in terms of the dimensionless drag coefficient, C_D , and was calculated using an expanded version of the empirical correlation by Schiller and Naumann (1933), as follows:

$$C_D = \max\left(\frac{24}{Re}(1 + 0.15 Re^{0.687}), 0.44\right) \quad (33)$$

3.5 Study of geometry improvements

This section presents the study concerning the new configurations of the probe, in order to produce more stable spectrometric measurements and to improve the measurement condition. Therefore the subjects presented will be further evaluated concerning the changes expected due to geometry changes.

First the new geometry change procedure will be explained. In this manner to provide a better understanding of the changes, a sketch representing the probe slit area is shown in Figure 9.

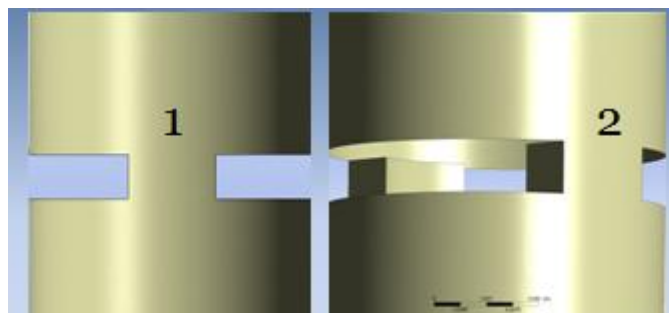


Figure 9: Representative sketches of the probe, general and side views

Figure 10 brings images of two different probe constructions; “1” is a side view of the original probe, and was selected to be the best view given the changes of

geometry to be shown in the sequence. At the right side, image 2 is shows the probe construction was changed.

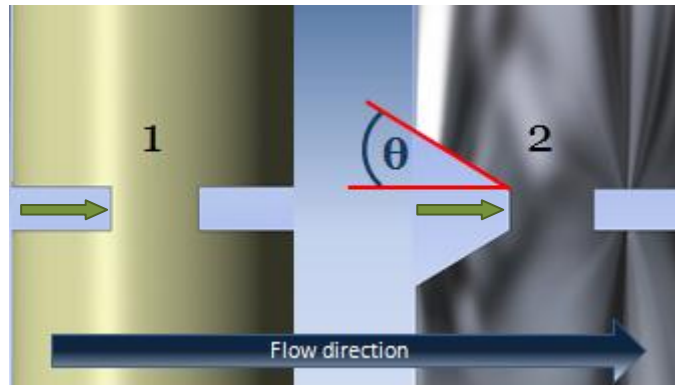


Figure 10: Geometry improvement in the probe construction.

In image 2 the probe inlet (green arrow) has a larger inlet area. The geometry changes can be measured by the angle represented as θ . The main purpose of this change is to increase the flow speed inside the probe just after the inlet. As a result it is expected that the higher flow velocities inside the probe can lead to a smaller recirculation near the side walls of the slit, and consequently a higher wall shear stress that can serve as an auto cleaning effect against bacteria adhesion.

For the changes in the probe construction 3 different angles, θ , were tested in order to predict whether the changes were effective and the effect of angle θ . Table 4 lists the parameters. The simulations were made with particles of 10, 50 and 100 micrometers in diameter. The reason for choosing these values for the diameter will be explained further on in the next chapter. The flow velocities used in the simulations were the lower ones in the experiments. The upper limit corresponds to the expected values used in the drilling machine.

Table 4: Changes in the probe construction

θ value in degrees	Inlet flow velocity (m/s)	
10°	0.039	3
20°		
30°		

4. RESULTS / DISCUSSION

4.1 Grid sensitivity study

An important topic when working with CFD is validation and verification. In some cases this work can be done to show which is the best turbulence model do represent a particular flow, or as it follows to evaluate if the mesh used in the simulations is good enough. In the sensitivity study, the mass flow through the slit was used to evaluate the error produced by changing from coarse to fine mesh. This is the same procedure adopted by (Soren, 2012).

$$\dot{m}_{Slit} = \rho_c \int_{A_{x,z}} (1 - \alpha_{x,z}) \vec{u}_{c,y} dA + \rho_d \int_{A_{x,z}} \alpha_{x,z} \vec{u}_{d,y} dA \quad (34)$$

where $\vec{u}_{c,y}$ is the velocity of the continuous phase and $\vec{u}_{d,y}$ of the dispersed phase, $\alpha_{x,z}$ is the local fraction and dA the area. The flow direction is y, while x and z form the planes perpendicular to the flow.

Figure 11 shows the calculated mass flow rate through the slit area of the probe as a function of the number of cells. It shows that the mesh choose for the channel geometry was a mesh of little more than one million cells, and as it is possible to see after these point the mass flow rate values, of 0.25 kg/h, does not change as much more than 2% even reaching the amount of 3 million cells.

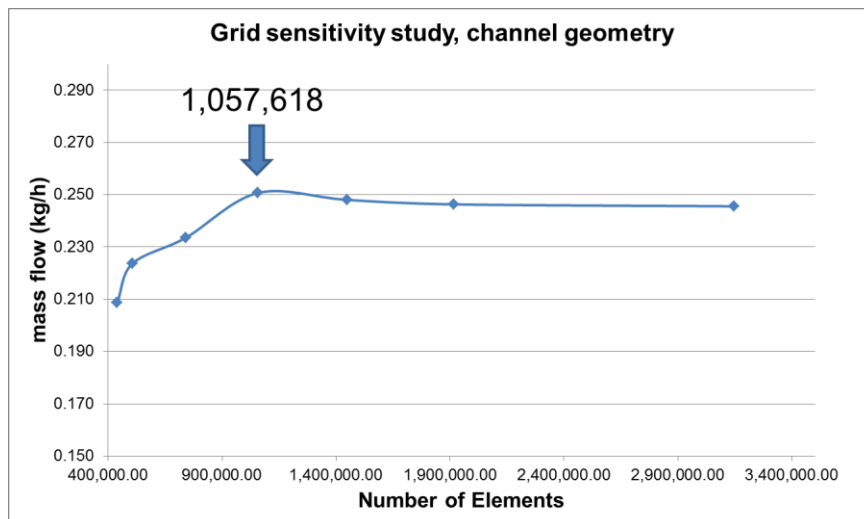


Figure 11: Grid sensitivity study, for the Plexiglas channel

Figure 12 shows the grid sensitivity study for the nozzle, used to attach the dip probe at the milling machine. For this mesh the circular cross section geometry resulted impossible to apply a spaced mesh and at the same time provide the y^+ value at the first cell needed for the K- ω model. The problem was found for all meshes with less than 1 million cells. That is why all the meshes generated were above 1 million cells. After that since for all the generated meshes the mass flow rate was basically the same, and the fluctuation is lower than 1 %, when compared within the finer mesh. The mesh with 1.5 million cell was choose because the better agreement with the y^+ at the walls.

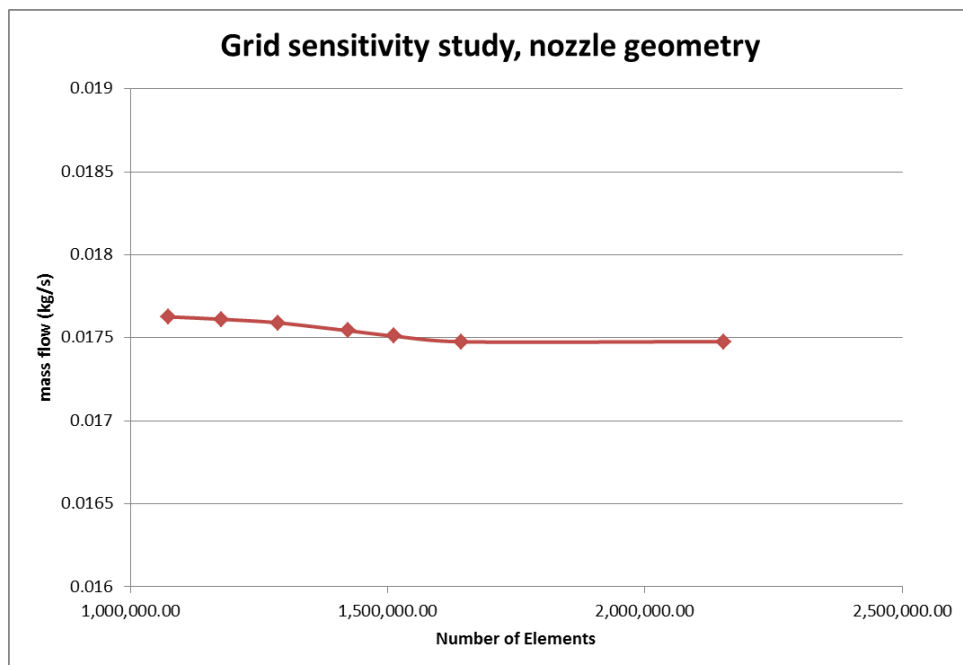


Figure 12: Grid sensitivity study, nozzle geometry

4.2 Segregation effects

Segregation is a problem that can occur during multiphase flow measurements. Particles can concentrate due to inertial or other forces making the flow characteristics to change. For the validation of the method of measurement that was selected for the EPM project, some condition were valuated to ensure that the estimated droplet concentration in the slit area of the probe correspond to the real

one. First for general proposes the concentration of oil, or the oil fraction, at a volume can be calculated by:

$$\bar{\alpha} = \frac{\int_V \alpha dV}{V} \quad (35)$$

where α is the volume fraction and V is the slit volume.

The mean velocities for the dispersed continuous phase at the inlet of the slit can be obtained:

$$\bar{u}_a = \frac{\alpha \int_A u_a dA}{A} \quad (36)$$

$$\bar{u}_b = \frac{(1 - \alpha) \int_A u_b dA}{A} \quad (37)$$

where a and b indicate the dispersed and continuous phase, respectively, while u is velocity and A the surface.

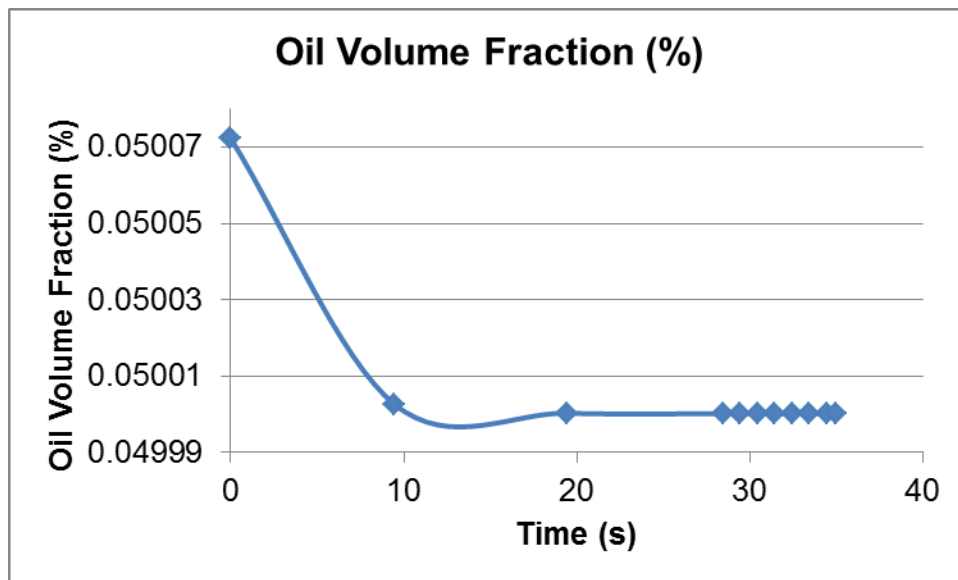


Figure 13: Time dependent concentration of particles of 100 nm size inside the measurement area

The concentration is volume averaged over the whole slit volume, which is the measurement area. The inlet boundary condition causes some instability at the beginning of the simulation. Thus, some fluctuations occur in the first seconds, and if

the simulation is run until about 35 seconds it is possible to see after some time that the oil volume fraction tends to stabilize (Figure 13).

Figure 14 shows the concentration ratio α/α_0 for each droplet size used in the simulation, where α is the concentration inside the slit area and α_0 is the concentration at the inlet. The concentration is calculated by:

$$\alpha = \frac{1}{n_t} \sum_{t=0}^{t=t} \bar{\alpha}_t \quad (38)$$

where n_t is the number of time steps and $\bar{\alpha}_t$ is the mean value at the calculated time.

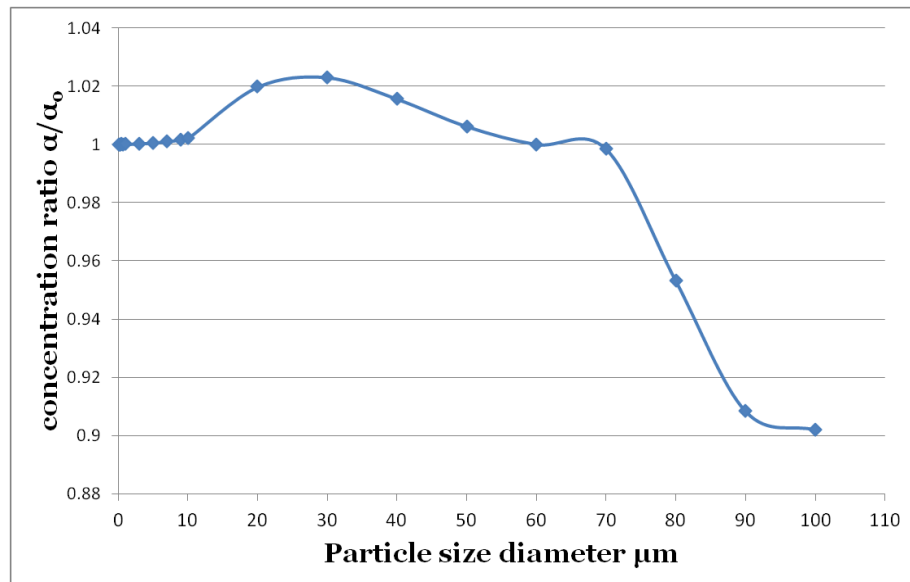


Figure 14: Time averaged concentration ratio inside the probe slit for different particle sizes.

While for small particles the concentration ratio is close to 1 for the particles up to 40 microns of diameter, bigger drops can be affected by the flow condition, resulting in a clear tendency to decrease the concentration ratio. Particles with diameter of 70 μm or more are much more affected by the increased speed at the probe surroundings. The decrease of oil volume fraction inside the probe, about 10%, is a possible end result of the higher inertial forces expected from the bigger particles, which would be more predisposed to create a preferential path around the probe external walls, where the fluid has the higher velocities, preventing a considerable amount of droplets to run through the probe slit area.

Since it is expected that particles with a diameter of 10 micrometer can represent the result from all the smaller diameters tested in the present work and no bigger particle is expected to be found in a stable MWF, a further study was performed to evaluate the influence of the flow velocity at the channel inlet on the 10 microns droplets. Figure 15 shows the results.

Figure 15 shows that by increasing the flow velocity, the concentration ratio is likely to increase, an effect that could be the result of the intensification of recirculation area under higher speed condition.

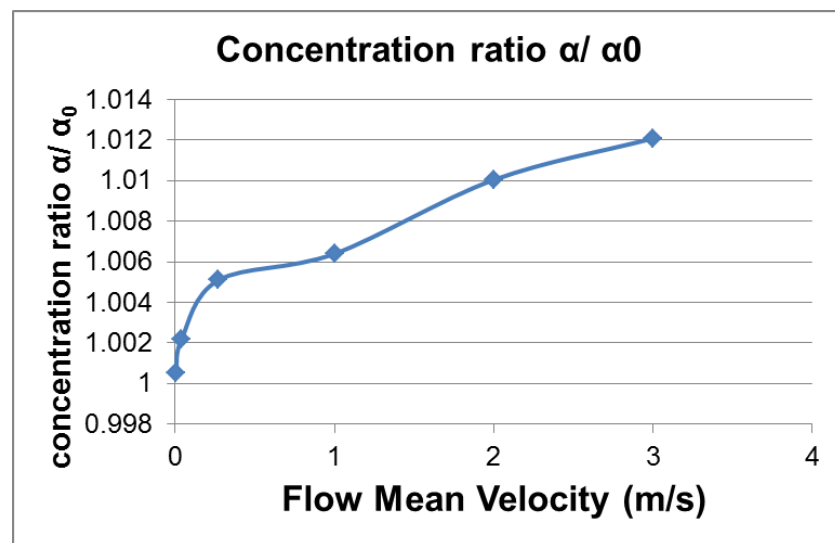


Figure 15: Oil Concentration Ratio vs. Flow Velocity, simulations for particle diameter of 10 microns

4.2.1 Effects of segregation inside the slit area of the probe

This chapter focuses on preventing possible effects of segregation in the area where the laser beam of the spectrometer is actually present. According to the specification of the equipment this area has a circular shape of about 0.3 mm diameter, placed at the center of the slit chamber. For this matter a more detailed study was made to see how the concentration can change over the slit area.

As shown previously the 10 microns droplet diameter and the 3 m/s flow velocity at the inlet was chosen, since they should be adequate to represent the flow conditions inside the slit area for all the droplets with smaller diameter. . Even knowing that no droplet with diameter larger than 10 microns should be present in an

MWF, the values of 50, 80 and 100 microns of diameters were included in the study. Just to evaluate how sensitive the measurement system is when the droplets reach larger size than expected or any other outside particle is added like a bacteria or any contaminant is present. It means that usually at the normal metalworking conditions no droplet is found to have a diameter bigger than 10 microns, which is why bigger particles are usually regarded as contaminant.

In order to perform the study, the slit area was populated with clouds of points where each of these points work as a local probe placed in an equally spaced distribution along the surface of a specific geometry created, which was chosen to be a cylinder built from the bottom wall of the slit to the top, a central cylinder with 1mm of diameter positioned with the center right at the middle of the slit, then three more concentric equal shapes with 2, 3 and 4 mm of diameter until almost reaching the lateral walls of the scattering area. An easier view of these areas is shown in Figure 16, where the yellow sketch indicates each of the areas of measurement. These measurement areas were created in order to ensure that the area of scattering of the probe, where the laser beam is placed, is not affected by any segregation effects caused by the flow behavior inside the probe, the laser beam is about 0.3mm in diameter, and is located completely inside the first cylinder, the other three ones are there to evaluate the concentration effect caused by the presence of vortices near the walls. It is important to mention that the flow direction is upwards in the figure, as indicated by the blue arrow at the right side of the slit. The graphic in Figure 13 shows the results for this simulation.

Figures 16 and 17 show simulation results from the Plexiglas channel system and by the side of each figure was placed a blue arrow indicating the flow direction inside the probe. These figures show that although the inner shape of the probe may result in vorticity effects near the walls, as can be seen from the blue streamlines, those lines indicate the places where the fluid has its slower movement, just like stagnation areas where segregation effects can change the measurement made by the spectrophotometer. Figure 16 is valid for the sequence of the data presented for the simulation made with different droplet diameters. Even by changing the droplet diameter from 10 microns up to 100 microns, it is not expected that the drops will be large enough to change the continuous phase behavior. In result, flow properties like the flow velocities around and inside the probe can be represented by Figure 16 in all the subsequent cases for the flow inside the channel with 3 m/s as inlet flow speed.

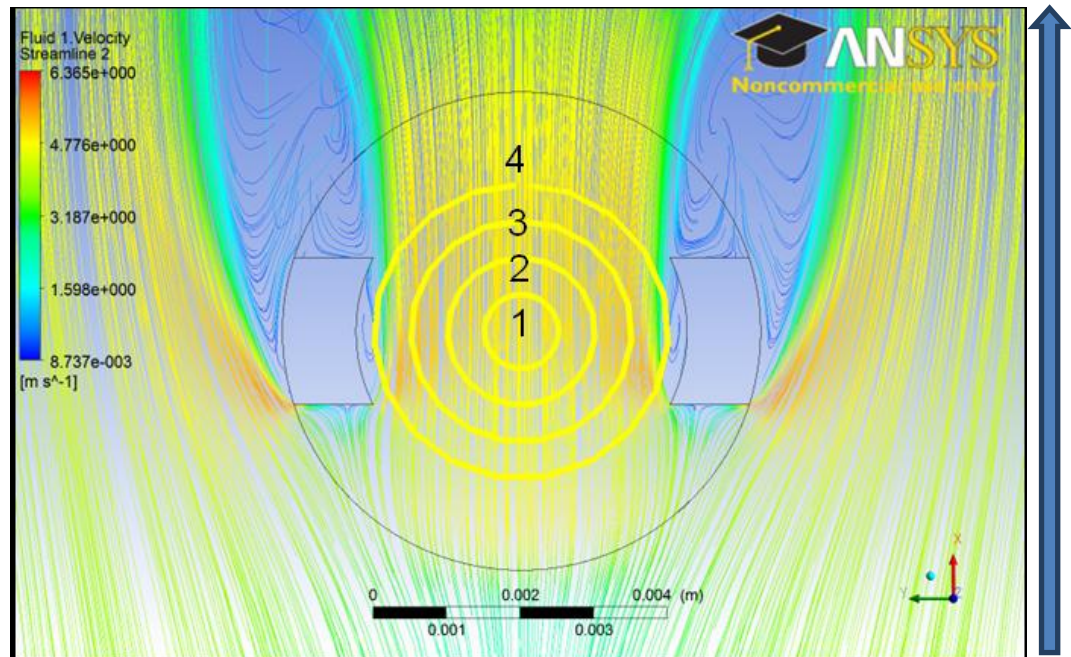


Figure 16: Oil Concentration Ratio vs. Flow Velocity, used variables, inlet 3m/s and 10 microns of droplet diameter

In Figures 17 and 18 it is possible to evaluate the effects of segregation due to the flow condition for a droplet size of 10 microns or lower.

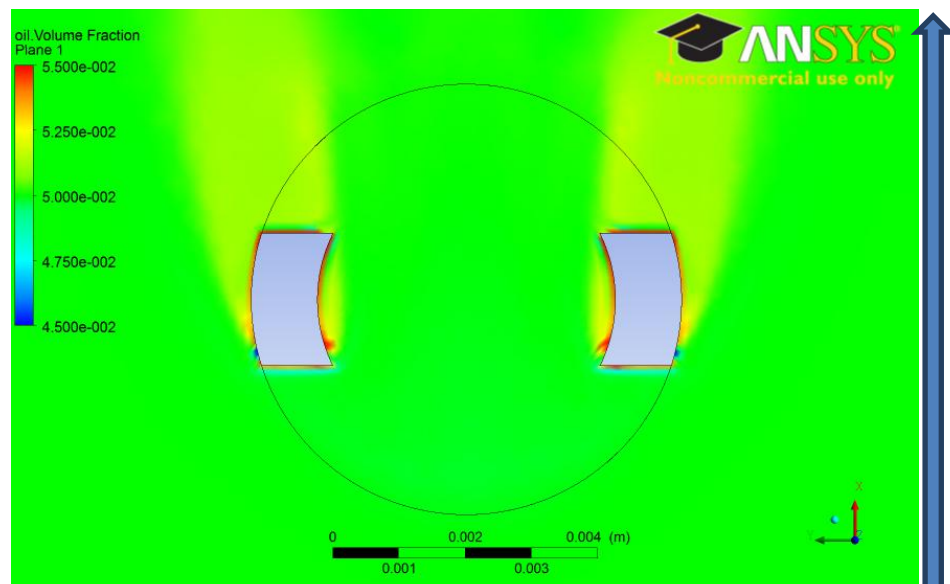


Figure 17: Oil Concentration Fraction, variables; inlet 3m/s and 10 microns of droplet diameter

It is interesting to see, that precisely at the recirculation areas after the probe's walls the concentration gets higher as indicated by the yellow colors in Figure 17. In

spite of the occurrence of vortices, any segregation effects that can change the measurement made by the spectrophotometer should correspond to oscillations of more than 10% in amplitude, and this fluctuation is not found observed in simulation results near the walls, the figure 18 shows the deviations for the areas numbered from 1 to 4 in the previous Figures.

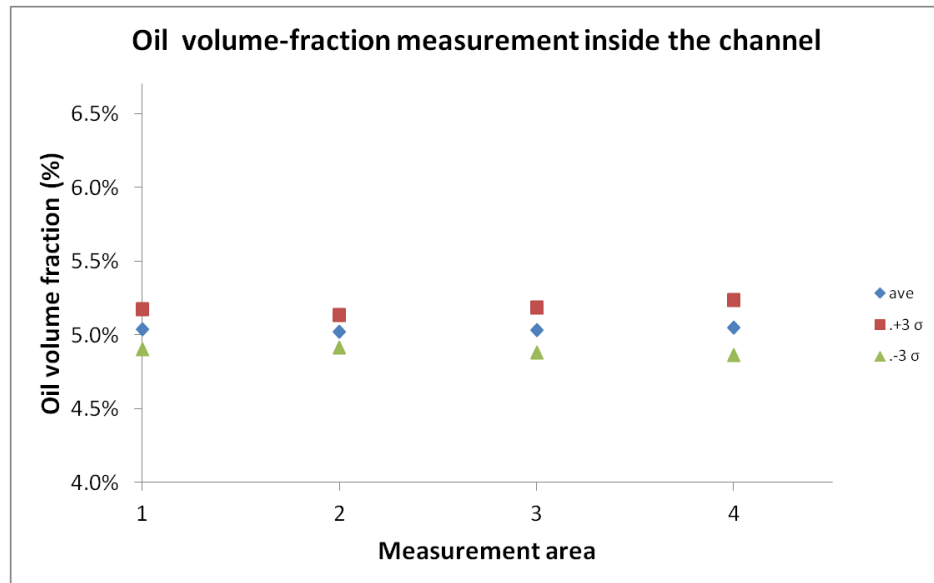


Figure 18: Oil volume-fraction measurement inside the channel, variables, inlet 3m/s and 10 microns of droplet diameter

The results for the simulation using the droplet diameter of 50 microns is shown at the two figures below, at figure 19 it is possible to see a much higher effect of segregation due to the flow conditions around and inside the probe. The figure 20 gives the main concentration and the values of the three standard deviations, which shows a much wider deviation from the mean value, when compared with the 10 microns droplets simulations.

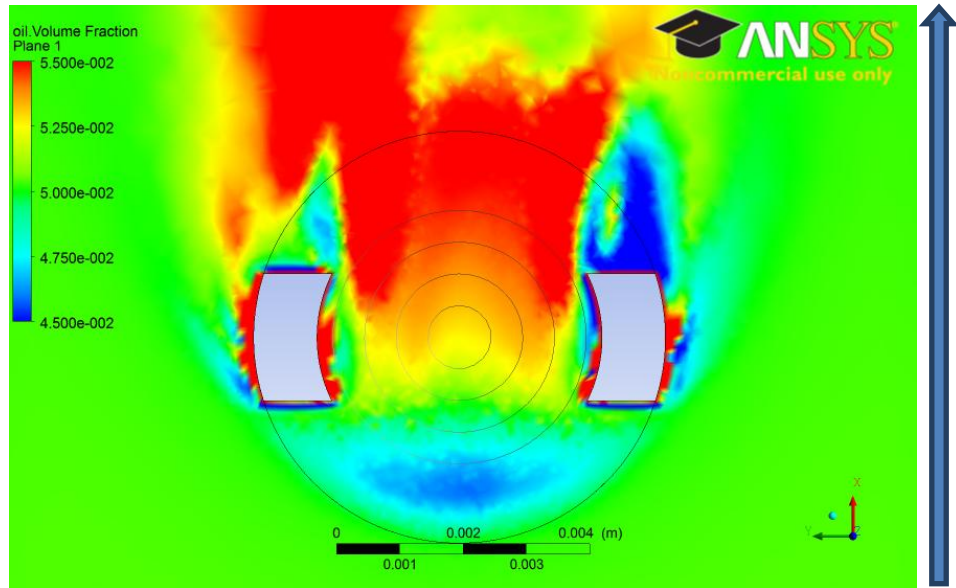


Figure 19: Oil Concentration Fraction, variables; inlet 3m/s and 50 microns of droplet diameter

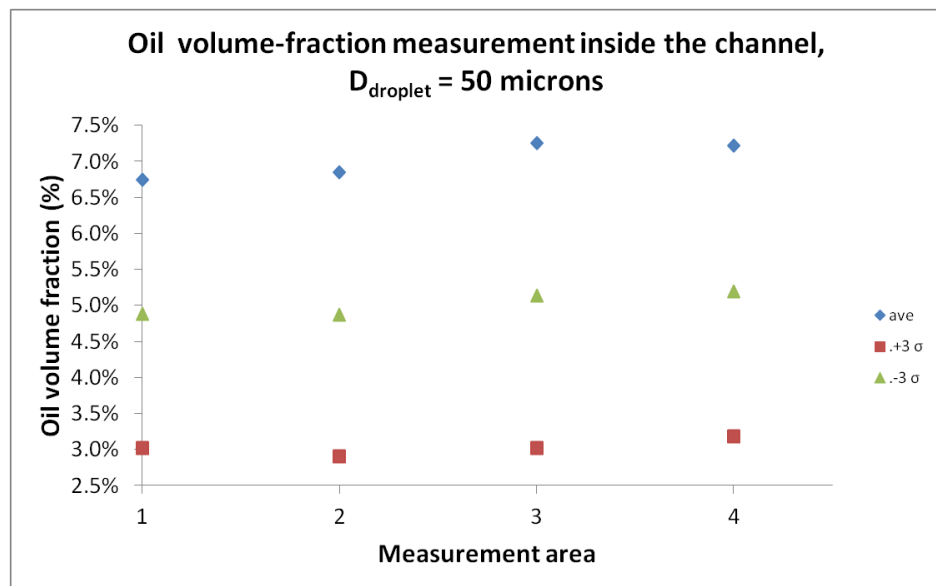


Figure 20: Oil volume-fraction measurement inside the channel, variables, inlet 3m/s and 50 microns of droplet diameter

Proceeding with a sensitivity study of the droplet diameter and to understand the segregation effects of the oil droplets inside the probe geometry the next two Figures, 21 and 22, concern the simulation data using a droplet of 80 microns of diameter, just like the previous data, the figure shows the volume fraction variation over the middle plan view of the probe, and the color variation from green to red indicate the areas where the volume fraction ratio is higher due to the recirculation of

fluid. The figure 22 is there to reassure that for bigger particles the range of volume fraction inside of the probe turns to be wider than for the smallest ones.

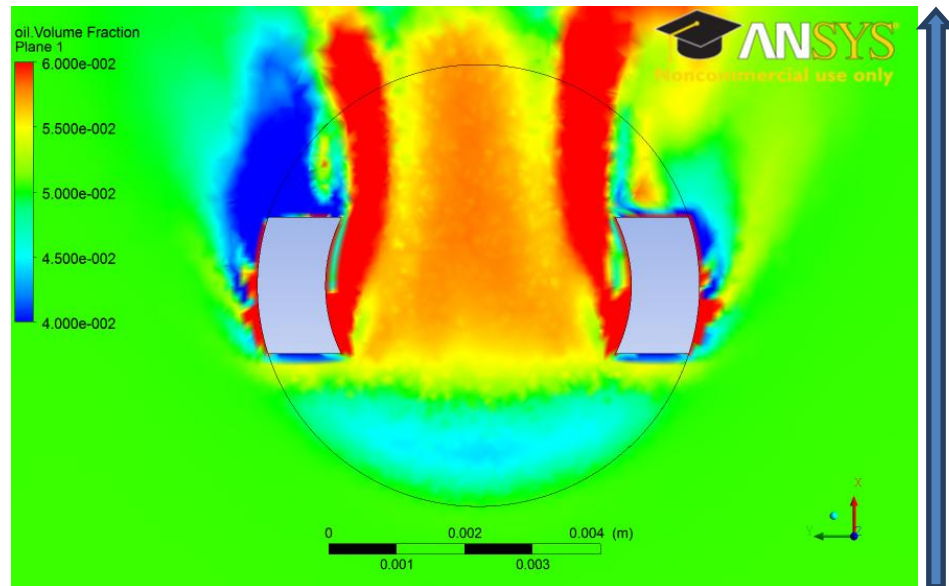


Figure 21: Oil Concentration Fraction, variables; inlet 3m/s and 80 microns of droplet diameter

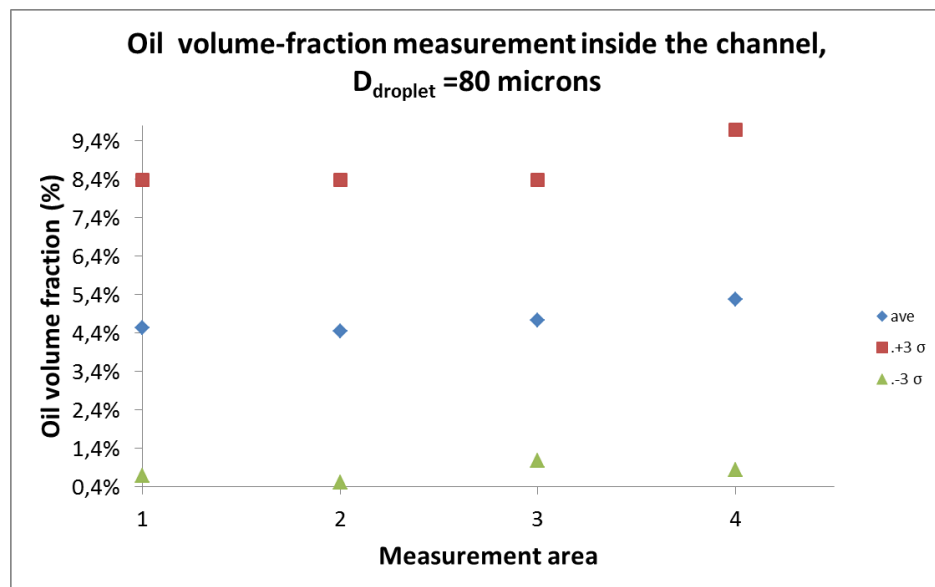


Figure 22: Oil volume-fraction measurement inside the channel, variables, inlet 3m/s and 80 microns of droplet diameter

The biggest particle tested has 100 micrometers. Such droplets are particularly, corresponding to 1/10 of the slit gap, which is only 1mm high. As expected, the segregation effects are much higher in such cases, since bigger particles are more affected by inertial forces. The results of the segregation effects

can be seen in Figures 23 and 24 where the concentration ratio varied over 2 times compared to the inlet condition, indicating that the equipment proposed would be able to provide a reasonable result for a dispersion with a droplet size distribution with the largest diameter close to 100 micrometers, and a different equipment should be proposed for that matter. For example, a new probe cloud be used, one with a larger optical length. Then the droplet size would not be significant in contrast with it.

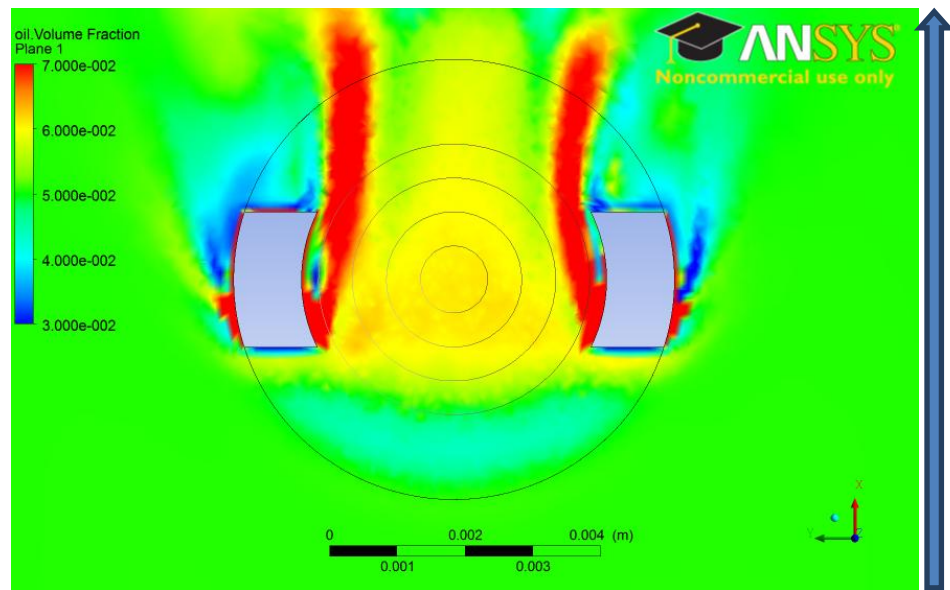


Figure 23: Oil Concentration Fraction; variables; inlet 3m/s and 100 microns of droplet diameter

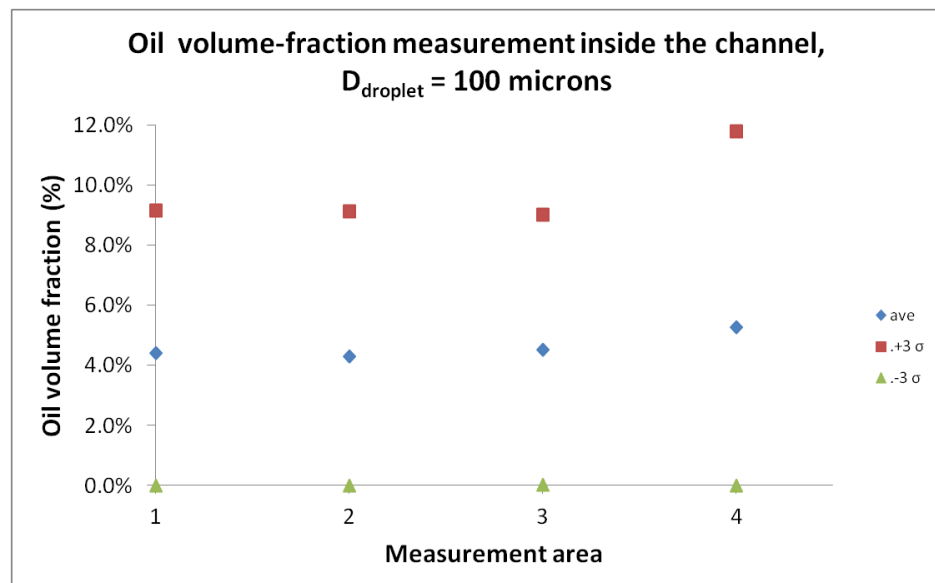


Figure 24: Oil volume-fraction measurement inside the channel, variables, inlet 3m/s and 100 microns of droplet diameter

Simulations were also carried out for the experimental setup in which the sensor was installed in the tube that brings the MWF to the nozzle of a drilling machine.

Figures 25 and 26 show results from the nozzle geometry. These additional study was carried out, because the nozzle created to attach the probe direct at the drilling machine has a geometry different of the geometry of the Plexiglas channel used at the laboratory experiments, therefore the flow condition in it is expect to be different affecting the flow behavior inside the probe as well. One first characteristic of this set up that need to be highlighted is the blockage effect, since the channel where the probe is placed is 1.38 times the diameter of the probe. This fact results in a much higher flow speed inside and at the surroundings of the probe. The effects on the fluid velocity profile can be seen in Figure 25.

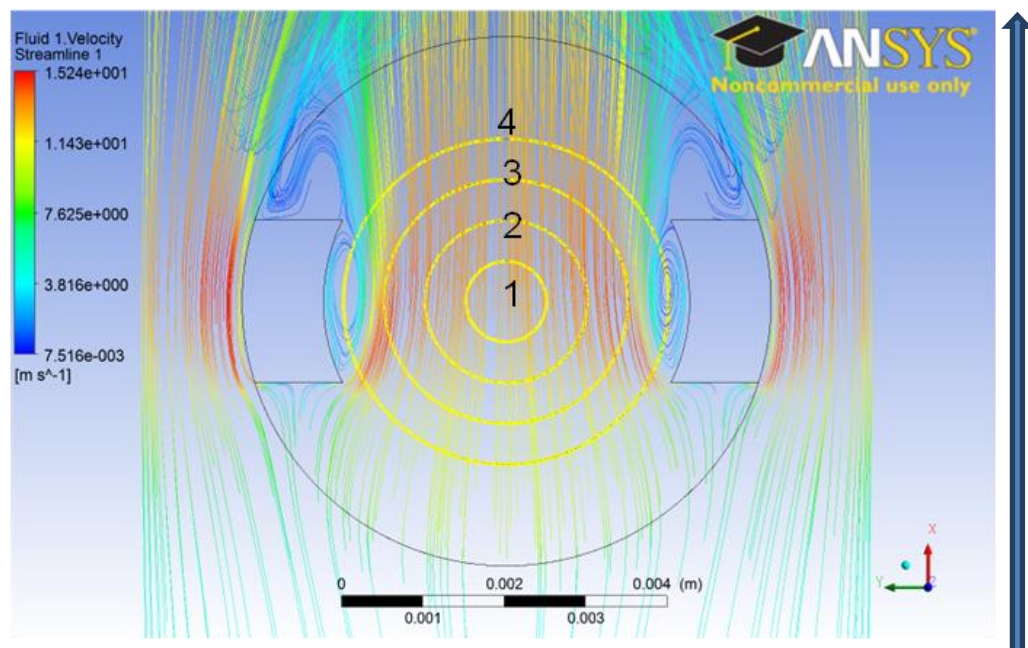


Figure 25: Velocity profile, nozzle adapter, variables; inlet 3m/s and 10 microns of droplet diameter

Compared to Figure 16, for the Plexiglas channel system, the recirculation areas begin to occupy a larger part with segregation effects, even though the spectrophotometer laser beam area did not change. Figure 25 shows that there is a trend to create accumulation areas, indicated by the red points near the walls. The larger areas of recirculation led to larger segregation effects pointed out in Figures 26

and 27. Figure 26 shows how the vortices near the side wall of the probe result in higher values of the standard deviation.

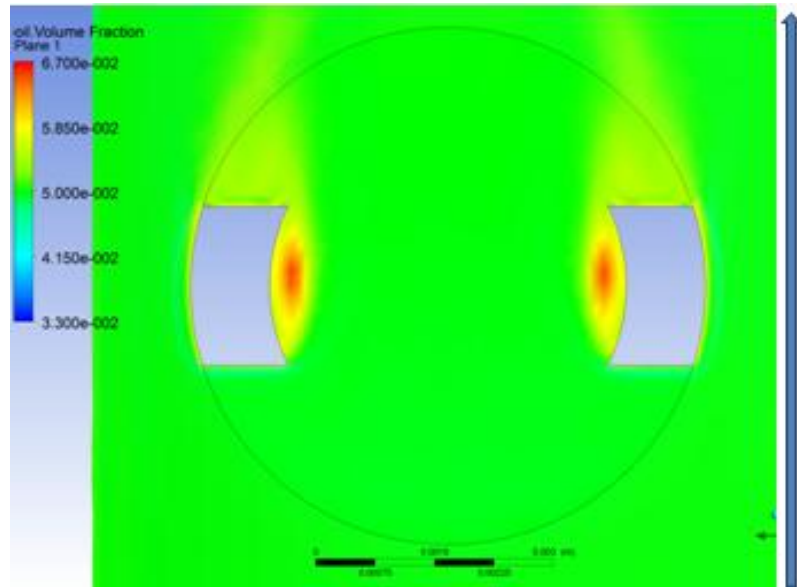


Figure 26: Oil Concentration Fraction; variables, inlet 3m/s and 10 microns of droplet diameter

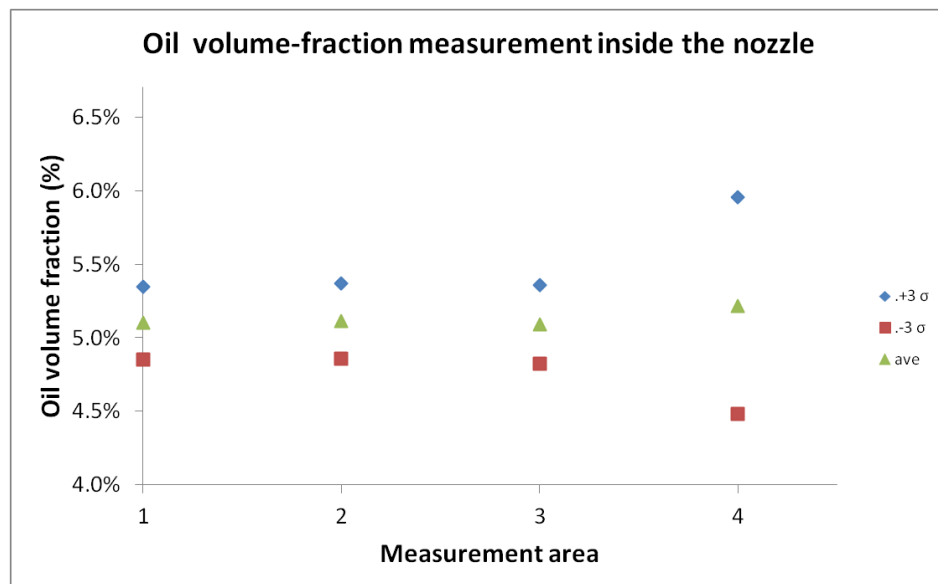


Figure 27: Oil volume-fraction measurement inside the nozzle, variables; inlet 3m/s and 50 microns of droplet diameter

4.2.2 Study on the placement of the probe

After studying the effects that the flow disturbances could have on the sensor measurements, simulations were carried out to evaluate the effects of the probe position on the results. The correct position is assumed to be the one where the slit area of the probe is perpendicular to the flow direction as used in the previous analyses (e.g. Figure 16).

In order to understand if a different position of the probe could result in a deviation of the measurements, two new meshes were created for the Plexiglas geometry.

In the first case the probe was rotated 45 degrees counterclockwise, and the results are as follows. Figures 28 to 30 show the simulation results for an inlet flow speed of 3m/s and a droplet concentration of 5% in volume, with droplet diameter fixed at 10 micrometers. The results indicate that it is possible to occur changes in the velocity profile as expected, but the most important result are shown in Figure 29, indicating the occurrence of considerable changes in the oil concentration inside the measurement area.

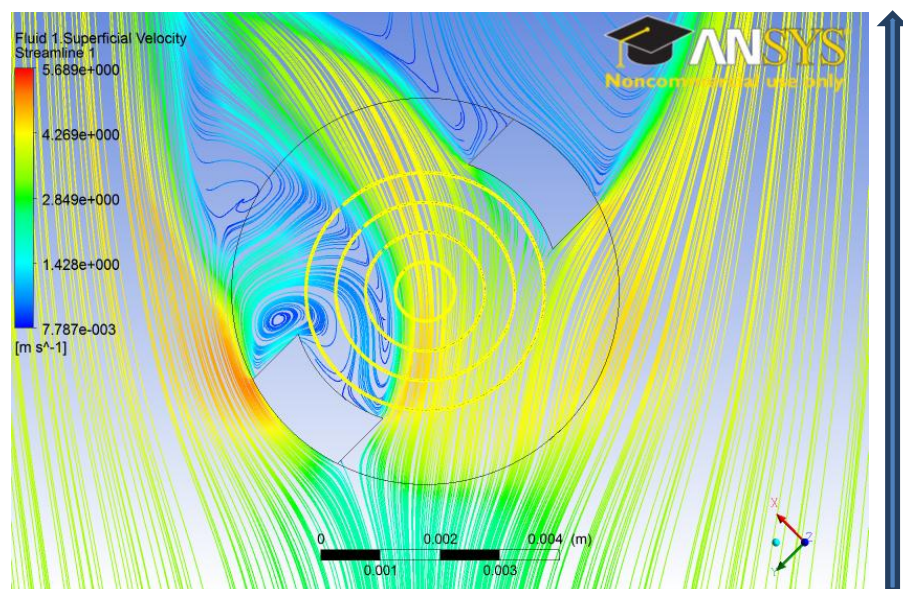


Figure 28: Velocity profile, position sensitivity study. Variables; inlet 3m/s and 10 microns of droplet diameter

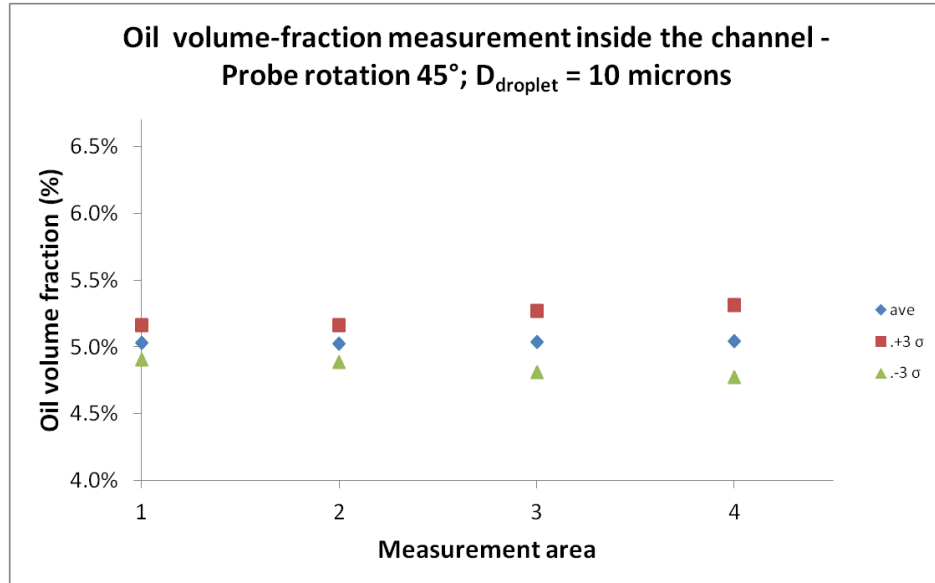


Figure 29: Oil volume-fraction measurement inside the sensor for 45° rotation . Variables; inlet 3m/s and 10 microns of droplet diameter

The results in Figure 30 show that besides the variation of the oil volume fraction along the channel, due to the flow interaction with the cylinder, the major changes are in the recirculation areas after the probe, which does not influence the measurements ensuing that the measurements can be accepted reliable even in such conditions..

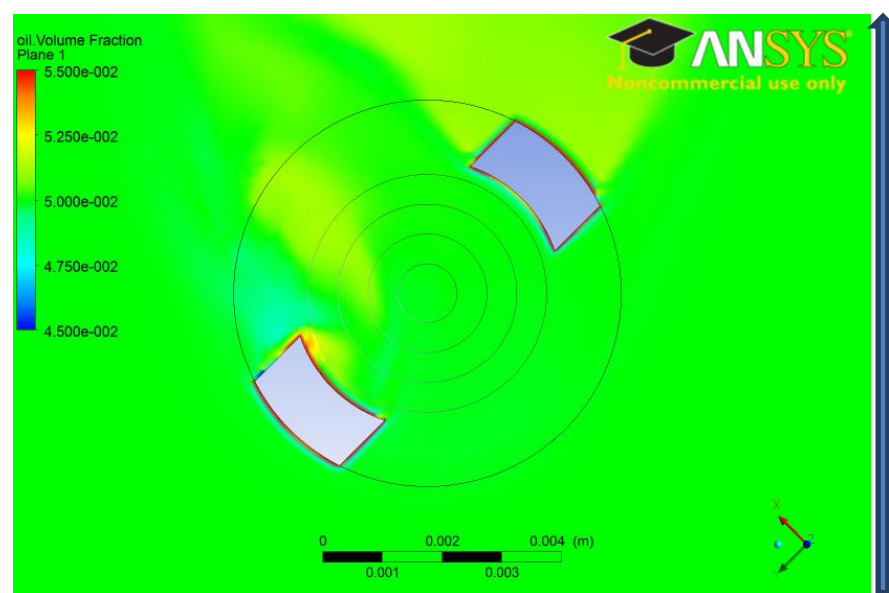


Figure 30: Oil Concentration Fraction for a probe rotation of 45°, variables; inlet 3m/s and 10 microns of droplet diameter

The next results refer to the behavior of the droplet size. Figures 31 and 32 show the oil phase volumetric concentration profile over the measurement area for oil droplets with 50 micrometers of diameter. Again the streamlines of the velocities are not shown for each case because the changes in the droplet should not be big enough to result in any change in the continuous phase behavior.

About the continuous phase behavior, it is interesting to see how the extra turbulence generated by the side wall, currently positioned in a way to block the flow path, also increases the effects of segregation when the droplet diameter is changed, for instance the 50 microns droplet concentration ratio in Figures 31 and 32 show a much higher deviation relative to the inlet condition than considering the probe in its ideal position for measurements.

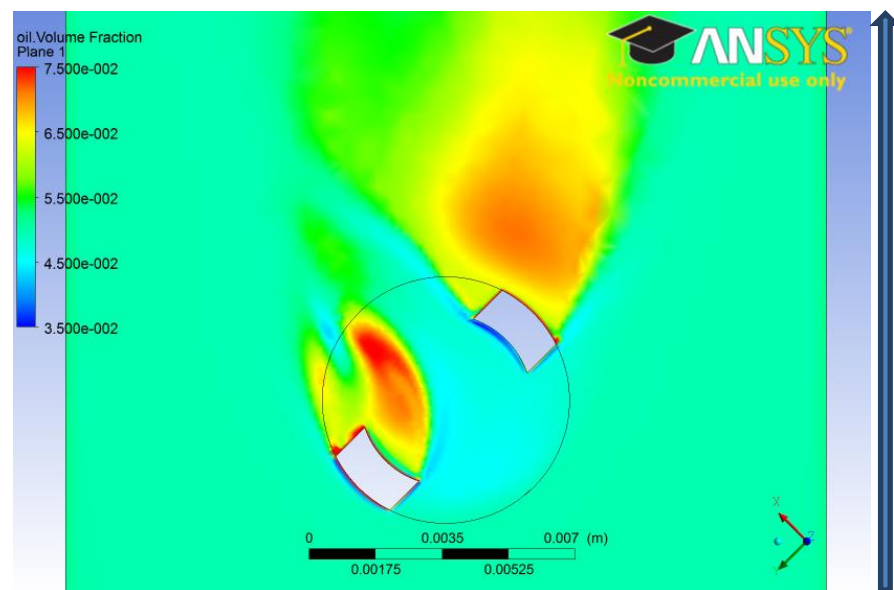


Figure 31: Oil Concentration Fraction for a probe rotation of 45°, variables; inlet 3m/s and 50 microns of droplet diameter

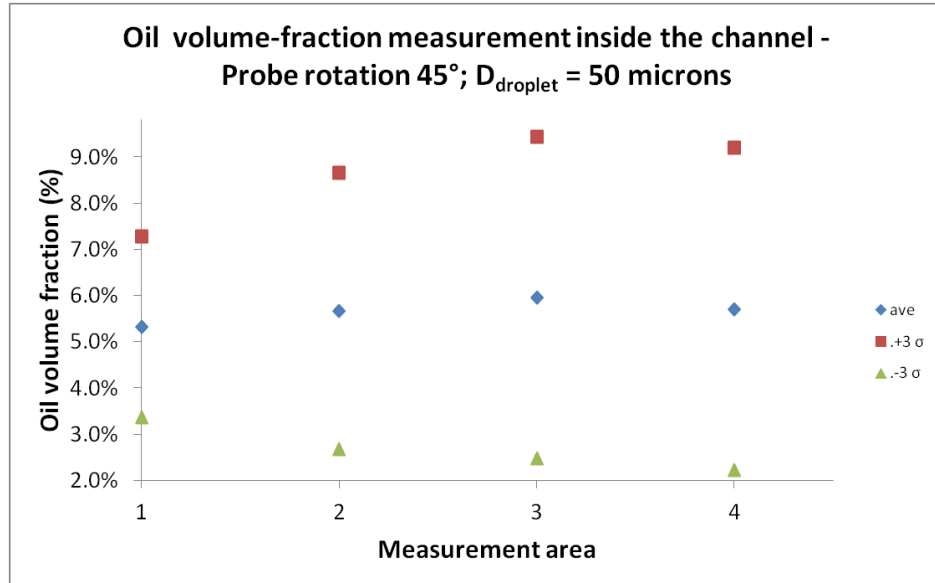


Figure 32: Oil volume-fraction measurement inside the channel for a 45° rotation Variables; inlet 3m/s and 50 microns of droplet diameter

The next results are for the droplets of 80 micrometers. These results follow the same behavior described. The segregation effects should be amplified with the increased droplet diameter.

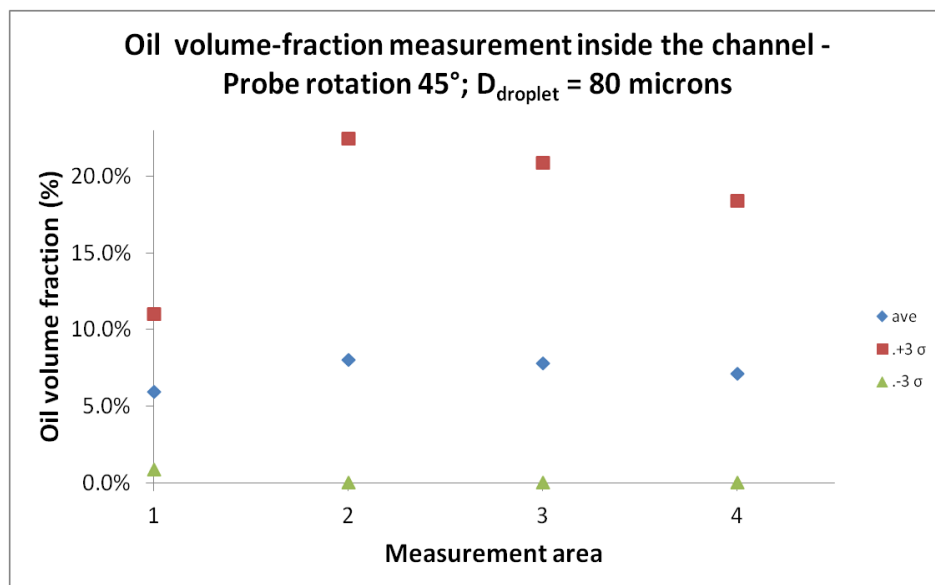


Figure 33 Oil volume-fraction measurements inside the channel for 45° rotation Variables; inlet 3m/s and 80 microns of droplet diameter

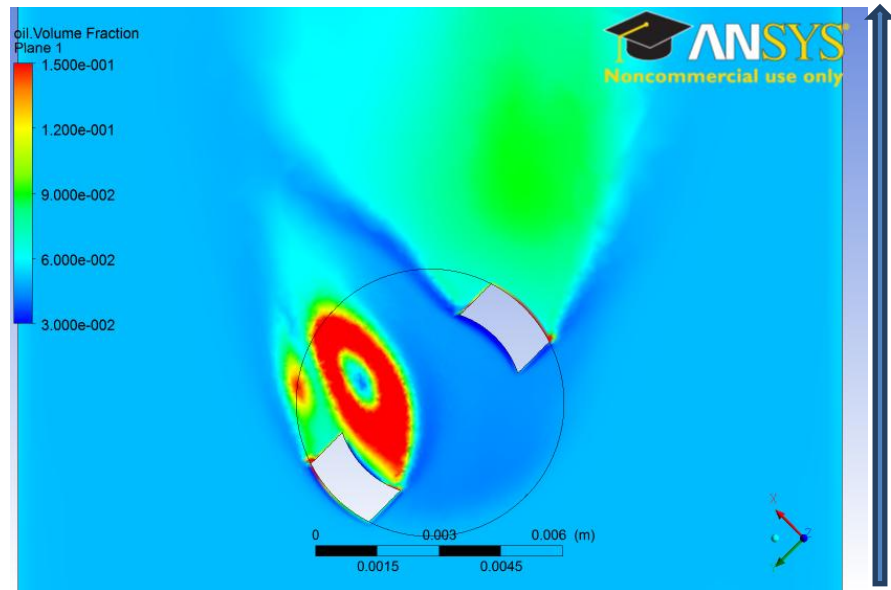


Figure 34: Oil Concentration Fraction for the probe rotation of 45°, variables; inlet 3m/s and 80 microns of droplet diameter

Simulations were also made for droplets with 100 microns and the simulation shows that the impacts over the concentration measurement can be huge, results that invalidate the use of this measurements system for an emulsion containing droplets over these big. In fact the previous simulation indicates that for droplets over 50 microns for diameter should not be tested with the proposed measurement system from the EPM project. But it is important to remember as well, that the MWF, that should be tested using this system should not have a droplet diameter bigger than 10 microns, and for the expected band of a MWF, from 50nm to 10 microns, the simulation results indicate that the measurement system should have no problems obtaining the right values, even with the probe placed 45 degrees at the wrong position.

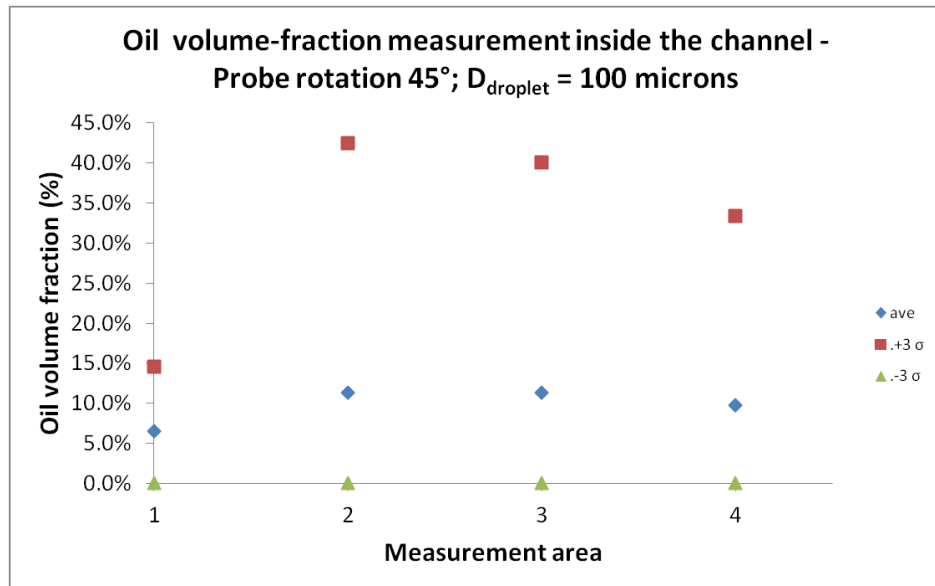


Figure 35: Oil volume-fraction measurement inside the channel for 45° rotation Variables; inlet 3m/s and 100 microns of droplet diameter

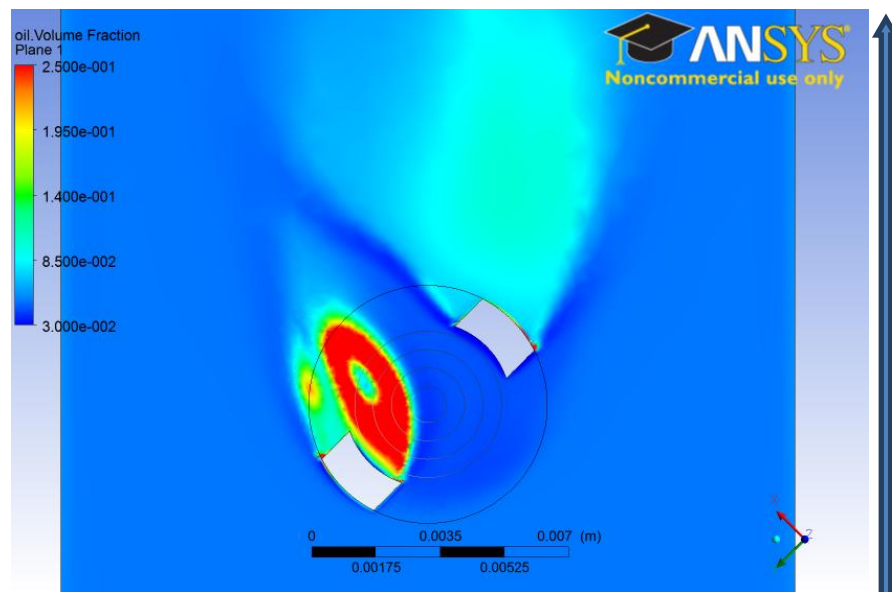


Figure 36: Oil volume fraction for 45° rotation of the probe , variables; inlet 3m/s and 100 microns of droplet diameter

Next a more extreme situation was tested, with the probe side wall faced to the flow direction, which means that the probe was rotated 90 degrees from its original position. It was expected that this would be the worst scenario since the side wall of the probe is blocking the fluid stream in its way through the slit area. Figure 37 shows how the velocity profile is disturbed.

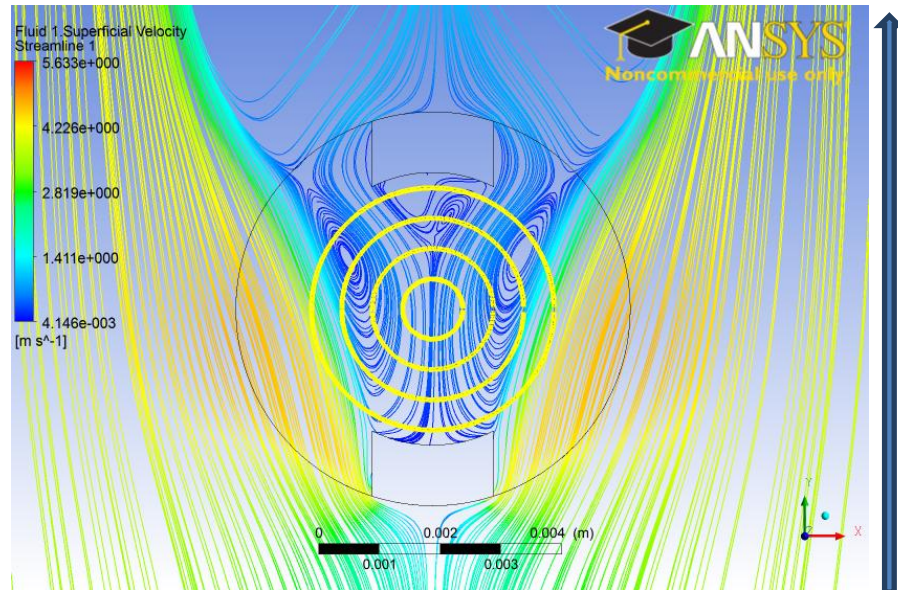


Figure 37: Velocity profile, for 90° sensitivity study

Figure 38 indicates that even in an extreme situation with the droplet size equal to 10 micrometers, the concentration can still be measured without being affected by segregation effects, although this set up should be avoided. Because it is showed before, that for the right probe position the segregation effects are even lower.

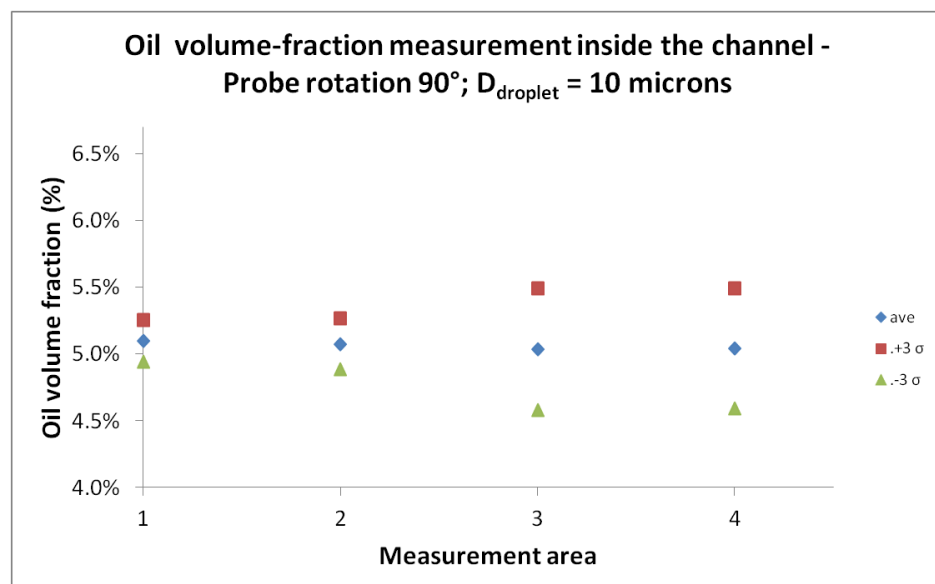


Figure 38: Oil volume-fraction inside the probe measurement channel for 90° rotation. Variables; inlet 3m/s and 10 microns of droplet diameter fraction

Figure 39 shows that, although there is some variation of the inlet oil volume fraction ratio at the probe slit area, it should not be big enough to affect the spectroscopy measurement.

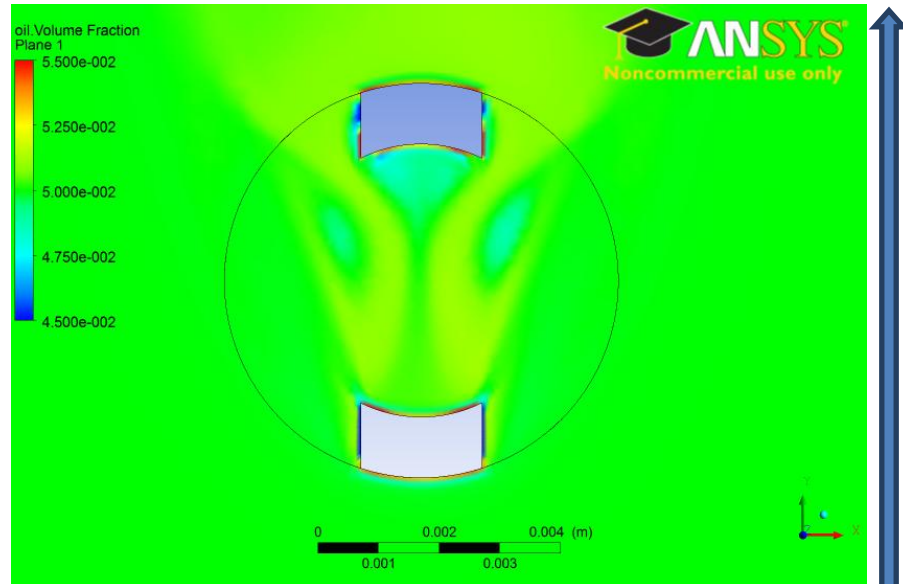


Figure 39: Oil Concentration fraction for 90°probe rotation , variables; inlet 3m/s and 10 microns of droplet diameter

Again, keeping the last analysis the effect of the flow for the different droplet diameters is tested, and once more the oil volume fraction ratio is increased with the increasing of the droplet diameter. Figures 40 and 41 refer to the simulation with droplet diameter equal to 50 micrometers,.

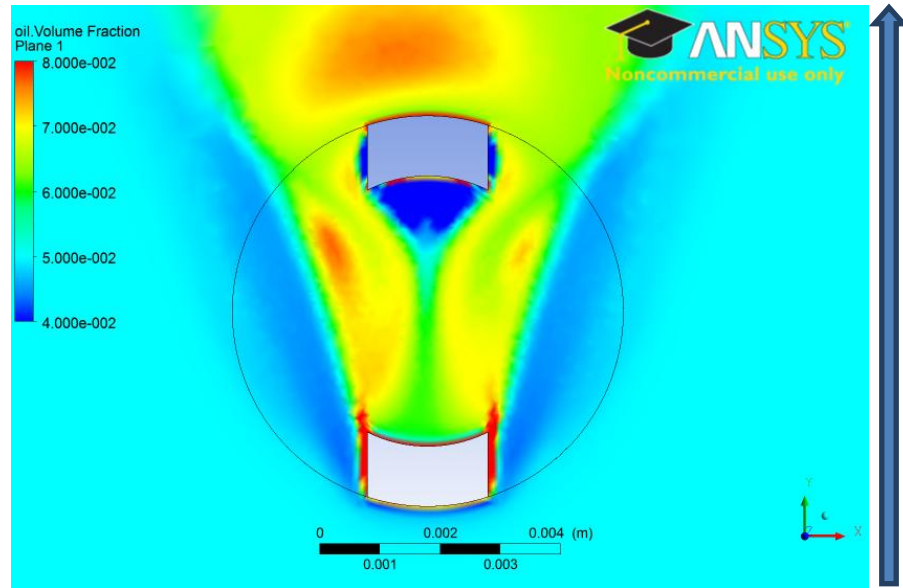


Figure 40: Oil Concentration Fraction for the probe rotation study, variables; inlet 3m/s and 50 microns of droplet diameter

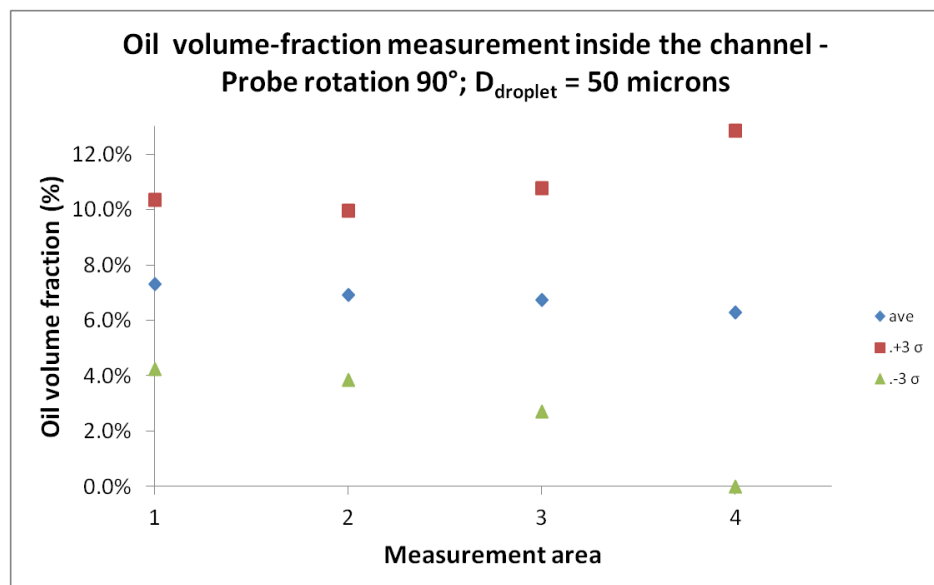


Figure 41: Oil volume-fraction measurement inside the channel form rotation study 90° Variables; inlet 3m/s and 50 microns of droplet diameter

The next figures represent the dispersion with a droplet size of 80 micrometers. It is interesting to see how the volume fraction fluctuates and its variation inside the probe due to the flow characteristics and the droplet mass.

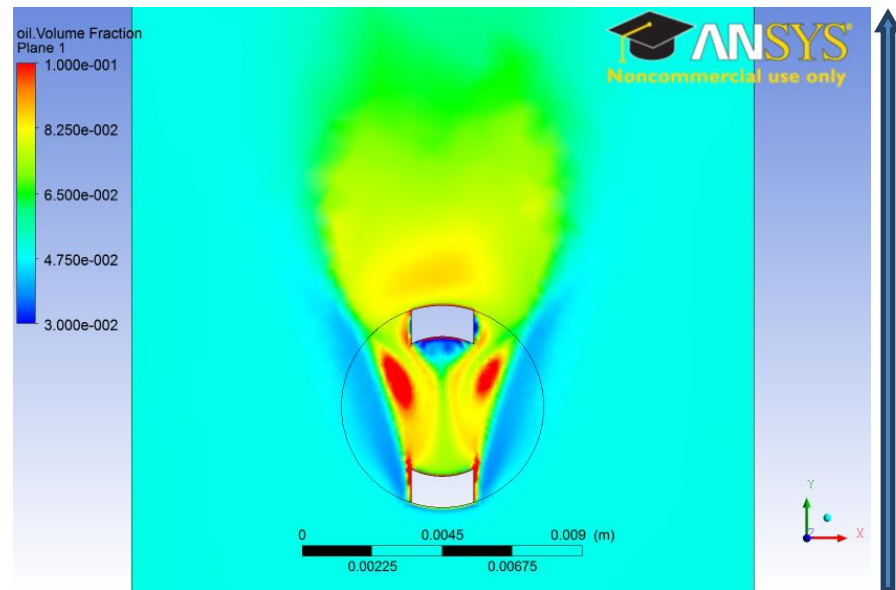


Figure 42: Oil Concentration Fraction from the probe rotation study 90° , variables; inlet 3m/s and 80 microns of droplet diameter

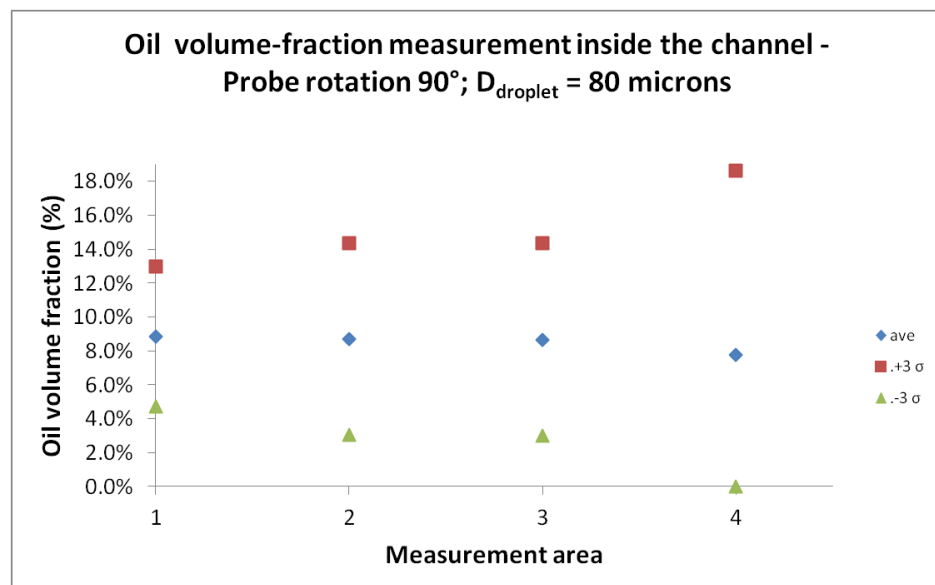


Figure 43: Oil volume-fraction measurement inside the channel from rotation study 90° Variables; inlet 3m/s and 80 microns of droplet diameter

Again in this case, as expected for bigger droplets, it is shown that this condition results in variations of volume fraction inside the probe, indicating that the data from the spectroscopy measurements cannot be reliable for the present condition. In addition Figures 44 and 45 support the results of the previous simulations. Thus, the present position of the probe relative to the flow direction

should be strongly discouraged, since it is shown to be prejudicial to the measurement system proposed.

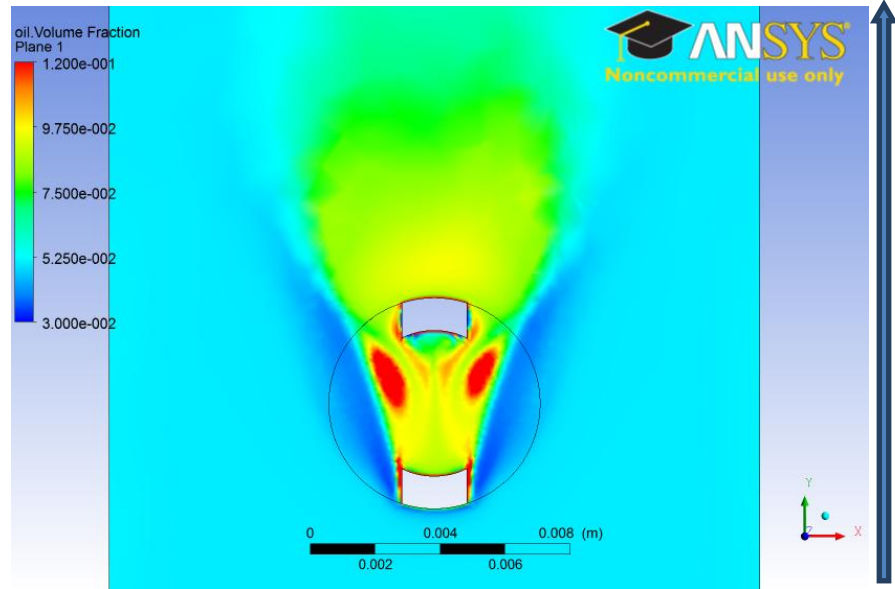


Figure 44: Oil Concentration Fraction from the probe rotation study 90°, variables; inlet 3m/s and 100 microns of droplet diameter

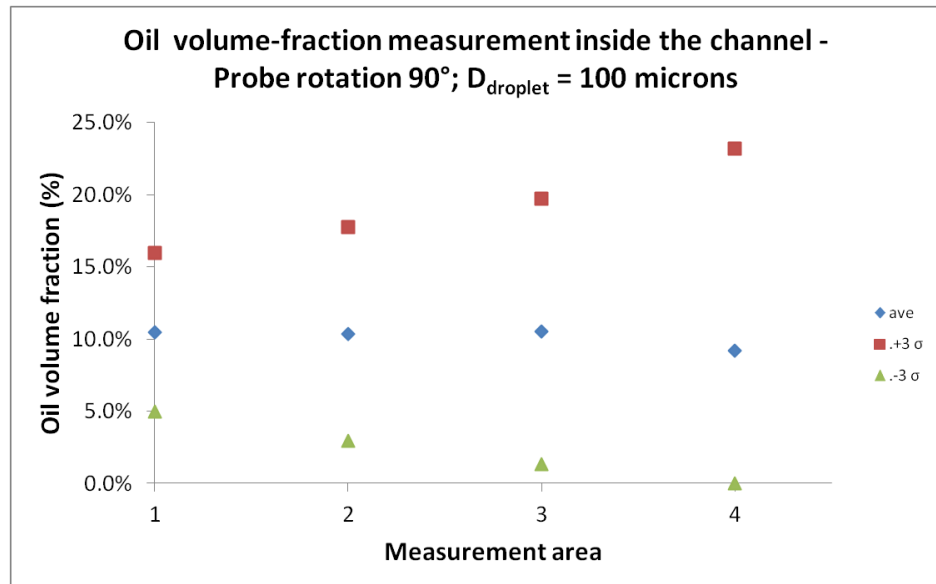


Figure 45: Oil volume-fraction measurement inside the channel from rotation study 90° Variables; inlet 3m/s and 100 microns of droplet diameter

4.3 Coagulation and Break up effects

First the critical Weber number was calculated to predict whether or not the possibility of droplet breakup phenomena should be expected due to the flow conditions provided by the measurement equipment setup.

According to (Binks, 1998), in order to break a single drop the applied shear stress against the interfacial tension (γ) of radius should be one that, the viscous shear stress of the continuous phase must overcome the Laplace pressure :

$$\text{Laplace pressure} = \frac{\gamma}{r} \quad (39)$$

Regarding Equation 55, one can assume that for an oil droplet formed from the same fluid, a higher applied shear stress is needed in order to cause the break up of a smaller droplet. Thus, the next simulations are aimed at verifying if droplet breakup should be considered in the model for larger droplets.

It is known that for a stable emulsion of cutting fluid, even when it is already to be replaced, the droplet diameter is not expected to be bigger than 10 micrometers. Consequently the diameter used in the breakup studies is 10 micrometers. The critical Weber number was calculated for an oil droplet with 10 micrometers of diameter. The resulting We_{cr} is in the order of 10^{10} , and the maximum Weber number found by the shear stress rate over the dispersed phase is found to be $We = 32307$. Since the maximum Weber number is much smaller than the critical Weber, the possibility of breakup of the oil droplets will not be further considered in the simulations.

Another topic of concern treated in this chapter is the possibility of the measurement system set up to provide conditions that can favor coalescence in the emulsion. It was already discussed at chapter 3.5 that coalescence is a phenomenon that depends on the approach of two or more droplets to take place, and the droplets involved in the process need to be close enough so that the film of fluid between them breaks and the droplets merge together into a bigger one.

4.4 Bacteria adhesion

The study topic “bacterial adhesion” is based on the wall shear stress to prevent or even to detach bacteria in adhesive contact with the inner walls of the probe. During the study, various inlet velocities were tested in order to identify the behavior of the wall shear stress inside the probe, especially because of the internal geometry of the probe that provides areas where recirculation or stagnation of the fluid can take place. The critical area, as well as the probe inside geometry is shown in Figure 46.

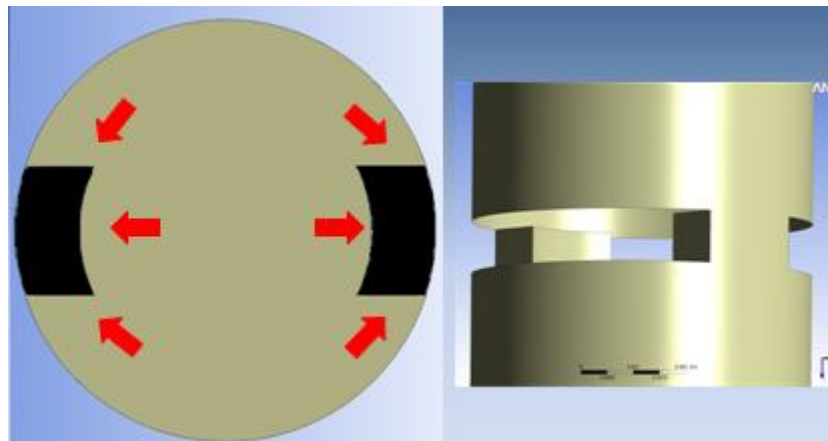


Figure 46: Inside geometry of the probe

In Figure 46 it is possible to see the bottom wall and its limiting lines close to the black blocks that indicate the side walls of the probe. The inside walls and the slit area of the probe can be seen at the right side of the figure, while the left side points out using red arrows the areas of the probe that can be critical for fluid stagnation, and bacterial contamination.

Figure 47 shows examples of how the wall shear stress varies inside the probe, as predicted by the CFD simulations. In this case the velocity at the channel inlet was 3 m/s, which should provide higher values of shear stress.

The walls were designated from 1 to 4, and they represent the following walls inside the slit area of the probe: number 1 is the bottom wall, walls number 2 are the ones facing the flow, wall number 3 is the one parallel to the flow, the only one with a

curvature. Finally walls numbers 4 are the ones at the outlet of the slit area. The two orange arrows shown in Figure 47 indicate the flow direction for the views 1 and 3.

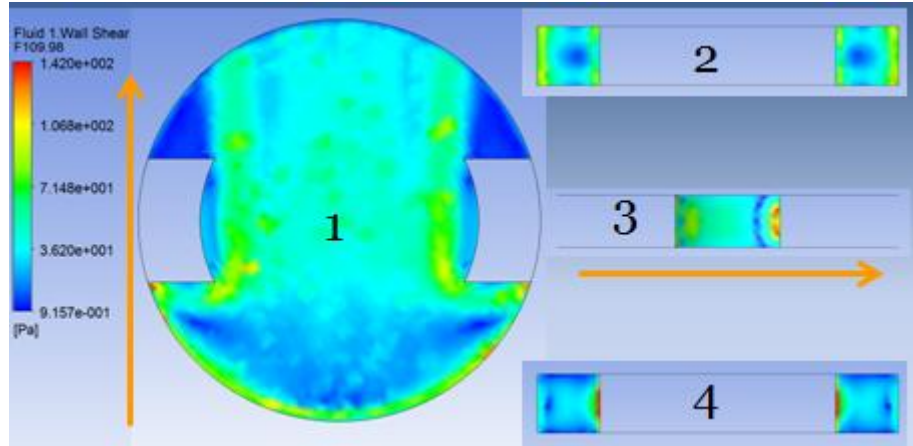


Figure 47: Wall shear stress variation inside the probe

Based on simulations for different inlet velocities, each one resulting in wall shear stress profiles like the one shown in Figure 47, the plots in Figure 48 was made, where the blue points indicate the maximum wall shear stress values and the red ones the minimum ones obtained.

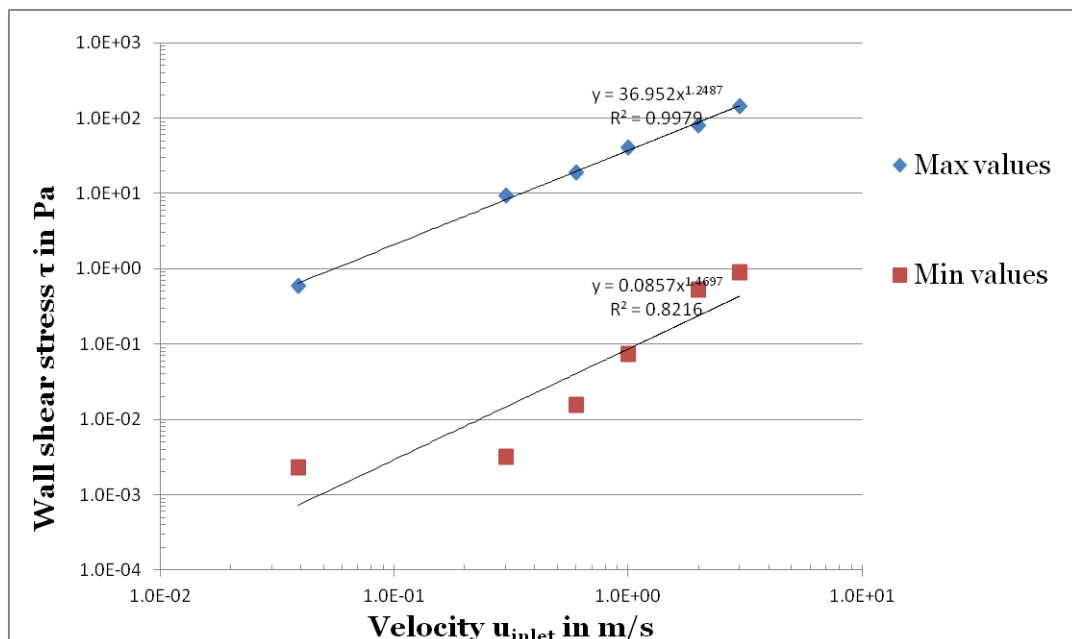


Figure 48: Wall shear stress inside the probe

The maximum and minimum wall shear stress increases when the velocity increases. The values of the inlet velocities at the channel were varied between 0.03 m/s and 3m/s, and this variation resulted in shear stress values from 0.002 to 142 Pa.

4.5 Changes in the probe Geometry

Aiming at improving the probe performance and preventing bacteria adhesion, different probe geometries were considered in the simulations, based on the methodology reported in chapter 3.6.

The results show the effects of the changes in various parameters that can impact the spectrophotometer measurements. Figures 50 and 51 show the flow velocity profile taken from a line inside the probe area, right into the slit center as indicated in Figure 49. Figure 50 shows simulation results for an inlet velocity of 0.03m/s; in the sequence Figure 51 shows similar results for an initial flow speed of 3 m/s, respectively the minimum and maximum values used in this study.

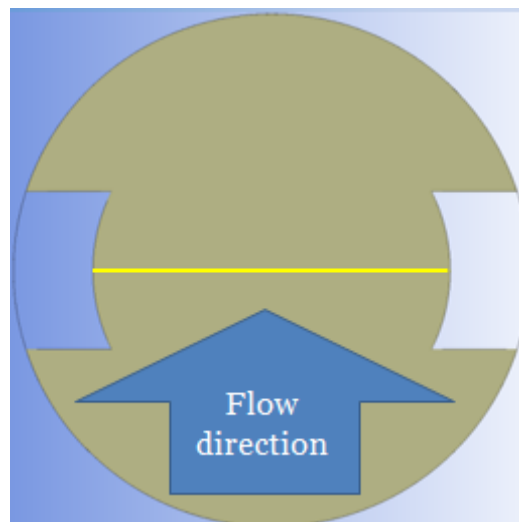


Figure 49: Representative sketch for the line inside the probe where the measurement is made.

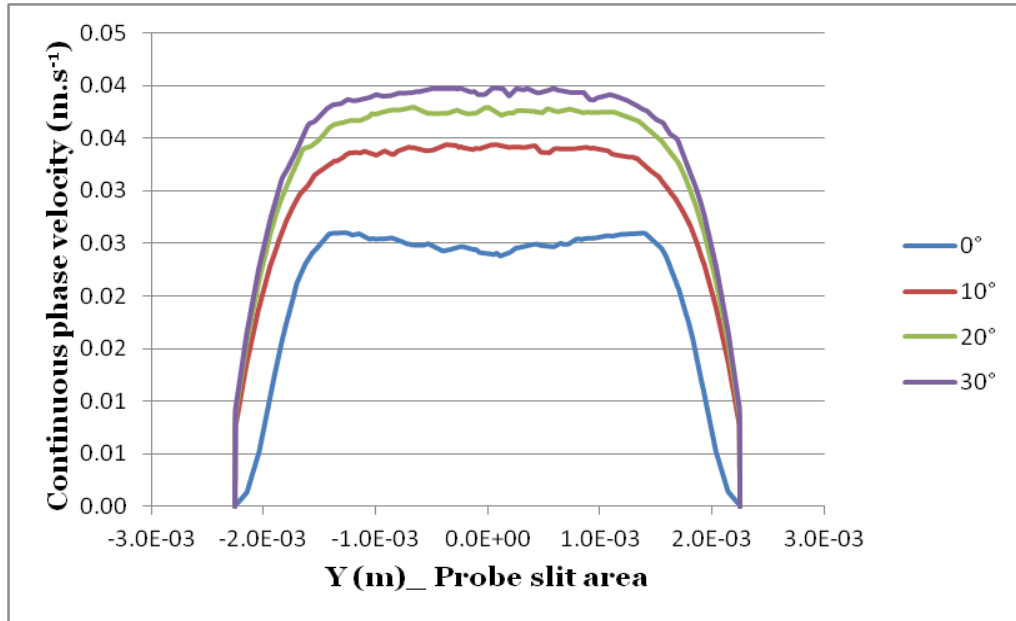


Figure 50: Flow velocity profiles for different probe constructions, given the slit inlet angle θ , with initial flow velocity of 0.03 m/s.

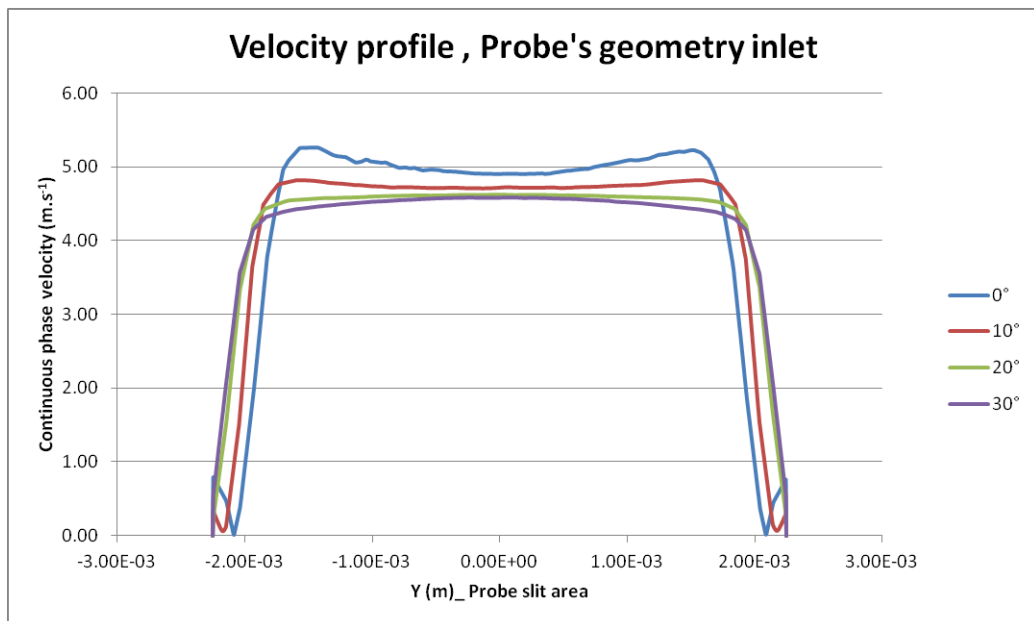


Figure 51: Flow velocity profiles for different probe construction, given the slit inlet angle θ , with initial flow velocity of 3 m/s.

The velocity profiles shown in figure 50 indicate that the main effect of the geometry changes for the lower initial velocity, is how developed get the flow velocity profile, when the probe inlet angle is increased. A different effect can be observed in figure 51, where it is possible to see that the velocity profiles tend to be wider when the angle θ increases. This is an evidence of a higher shear rate near the walls.

The increase of the fluid shear rate near the wall can be easily seen in figure 52 below, although the higher values of shear rate should not be enough to provide a droplet breakup overcoming the critical Weber number of the droplets. a variation of that value could be enough the proved sufficient wall shear stress to avoid bacterial contamination at the wall. Figure 52 corresponds to the lower simulation initial flow velocity of 0.003 m/s.

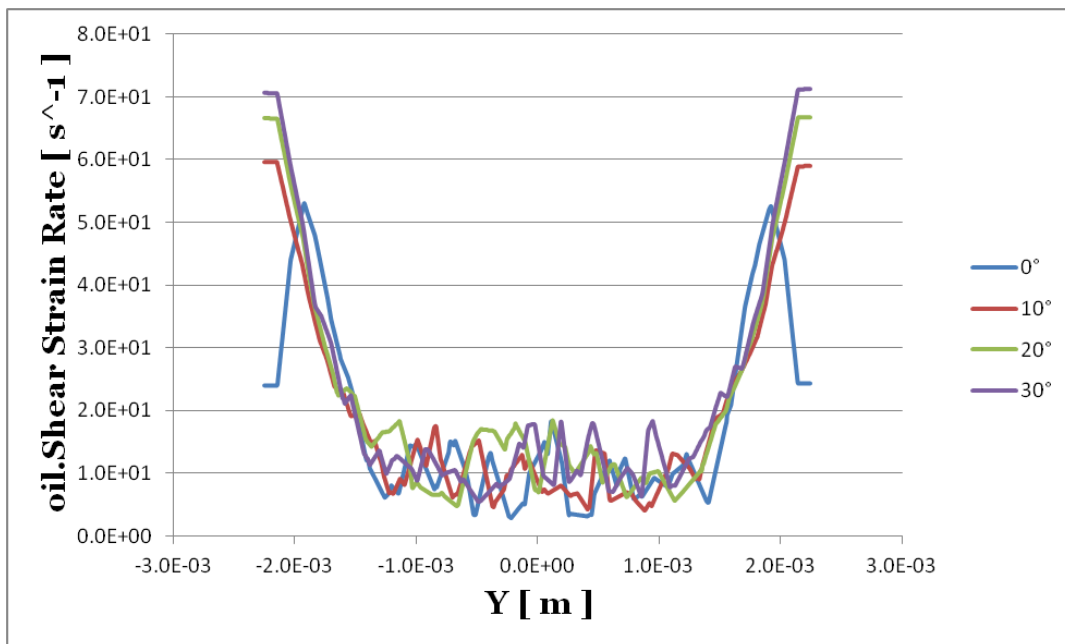


Figure 52: Oil shear stress rate for different inlet geometries, for an initial flow velocity of 0.03 m/s

Finally concerning the effects of the geometry changes in the probe the next figure presents the oil fraction profiles inside the probe, based on the inlet oil volume, and in contrast of the wall shear stress values, where the changes result in a higher wall shear stress inside the probe. The sensitivity effect of the probe with droplet diameter higher than 10 micron is increased along with the geometry changes. The increase sensitivity can be seen in Figure 53.

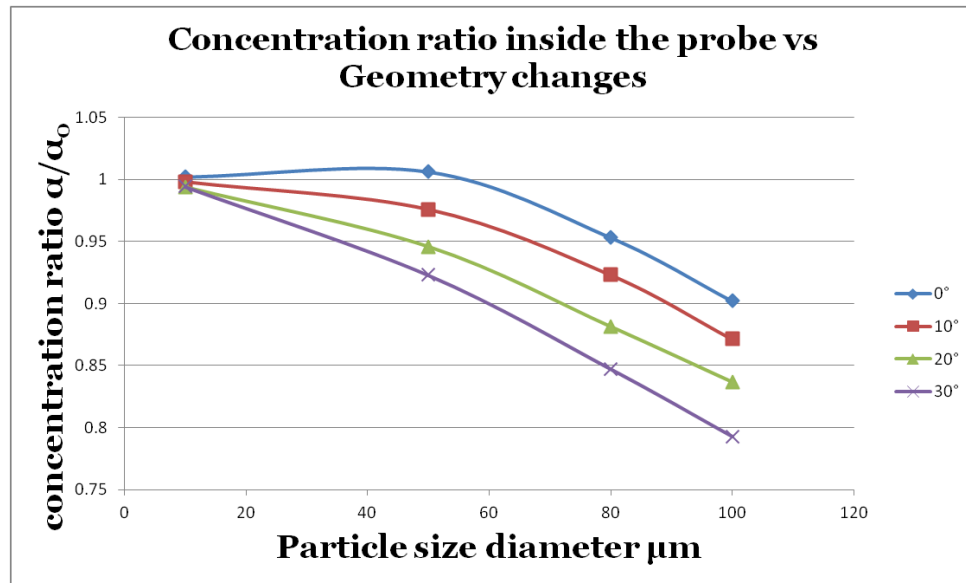


Figure 53: Concentration inside the probe vs. geometry change

4.6 Comparison between Euler-Euler and Euler-Lagrange models discretization

It is known that the Euler-Euler discretization, due to the approach takes consideration the dispersed fluid as a continuum one and therefore losing the individual behavior of the components present at the dispersion, it has some disadvantages when compared with an Euler-Lagrange approach, especially considering the dispersed phase. Furthermore the Euler-Euler model is expected to have more difficulty to get accurate data, when the dispersed phase has a range of particle sizes, because the Euler-Euler model uses a single velocity field to all the multiple size groups.

Even though the simulations presented were prepared mainly using a single droplet diameter in each simulation, an additional study was made using the particle tracking model, in order to evaluate in more details a small group of particles, and identify if they will present any particular behavior that may not be predicted by the Euler-Euler model.

The next figures show simulation results using the k-w model, the same turbulence model used in all the previous simulation results. All the new set of simulation refer to simulations with metal working fluid with the same characteristics

as before. The oil volume fraction was fixed at 5%, and a 10 micrometer droplet diameter was used to represent the dispersion. The only main difference at this result is the information of the number of points of injection to the dispersed phase, this points were placed at the inlet in a equally disperse configuration, and the total number of injection points was studied in order to evaluate if the small number of droplets consider at the entering at the domain, can represent a emulsion which is a dispersion usually with a enormous number of droplets contained at the dispersed phase. Before any discussion about the results from the CFD simulation it is important to explain that a new mesh sensitivity study was carried, using the previous mesh as start point. After the mesh was once more validated the further avaliation at the flow behavior was made.

The next chart in Figures 56 was made with the concentration ratio taken from cuts along the Plexiglas channel as shown in Figure 54. The point where the distance met the zero at the axis represents the concentration ratio inside the slit area of the probe, and it is represented in Figure 55 by the blue surface.

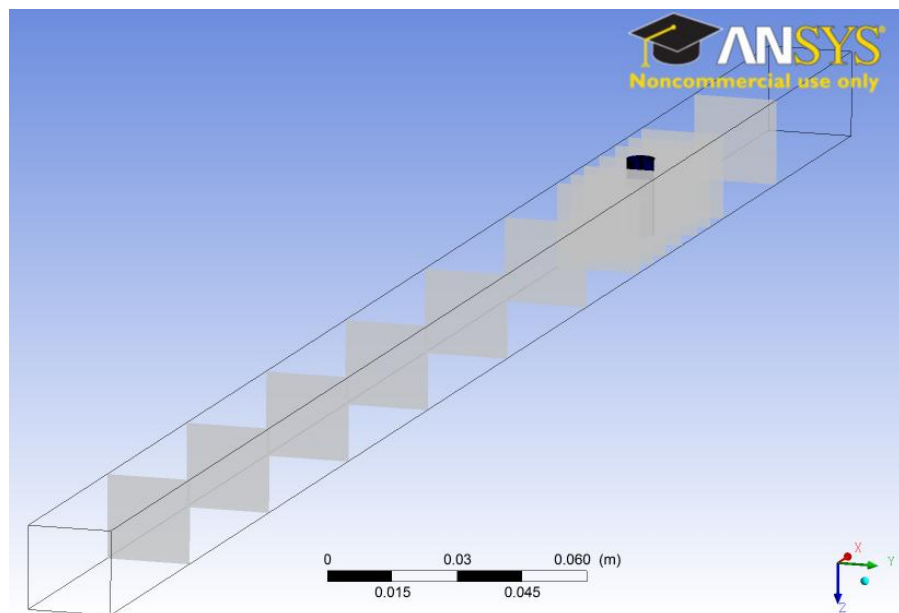


Figure 54: Plexiglas measurement areas of the particle tracking model

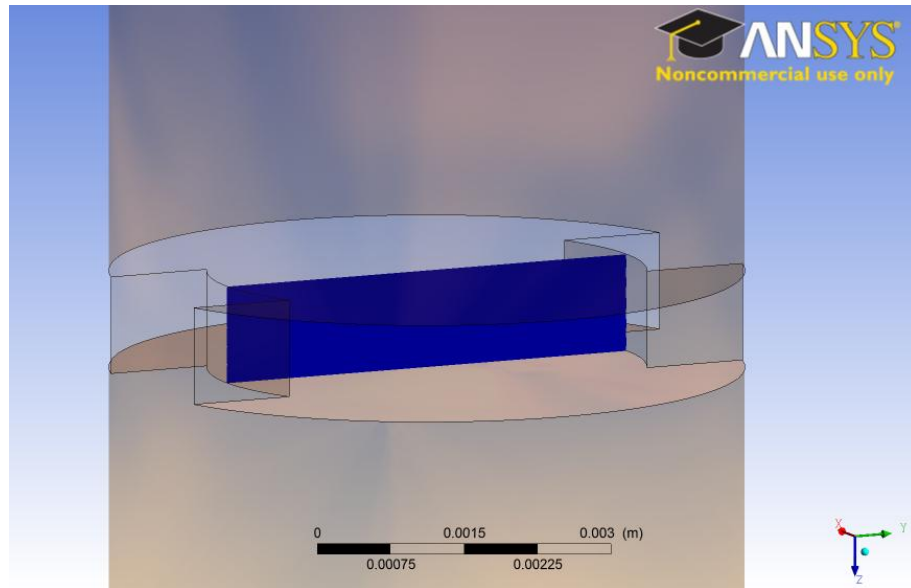


Figure 55: Measurement area inside the probe slit chamber

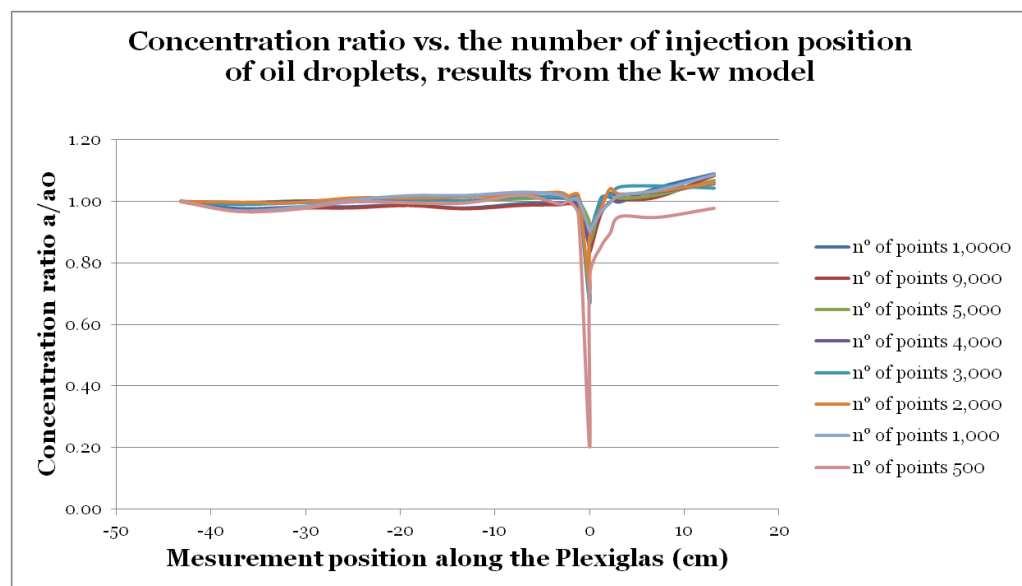


Figure 56: Concentration ratio vs. the number of injection position of oil droplets, results from the k-w model

Figure 56 shows the volume fraction data using the particle tracking model along the channel, and the k-w turbulence model. It is possible to see that along the channel the concentration is approximately constant, but inside the probe the values tend to be lower than expected if the flow is isokinetic around and inside the probe. Although in extreme cases when the inlet points are about 500 the value of the oil volume fraction inside the probe is about 20% of the inlet value, this disturbance

could be caused by the smaller number of particles chosen, which is not enough to represent the emulsion, and then many of the particles travel around the probe rather than through the slit area. Besides, it is possible to see an increase of the oil concentration ratio after the probe, which may be due to the turbulence disturbances created after the probe structure.

In the sequence the velocity profile inside the probe is shown evidencing that for any two phase flow model, the continuum phase flow behavior is basically the same as shown in Figure 57.

Finally, in order to highlight the differences between the models, a chart with the oil volume fraction was made using a line inside the probe as a measurement position, like the one shown in Figure 49, and a plot of the oil volume fraction over this line was created, as shown in Figure 58.

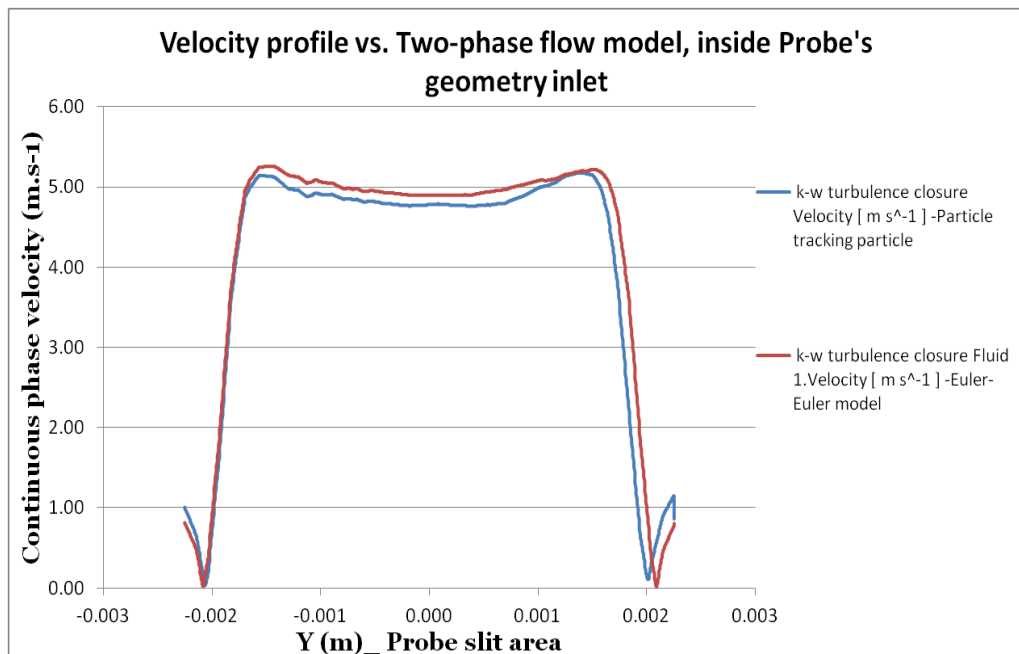


Figure 57: Velocity profile vs. Two-phase flow model, inside Probe's geometry inlet

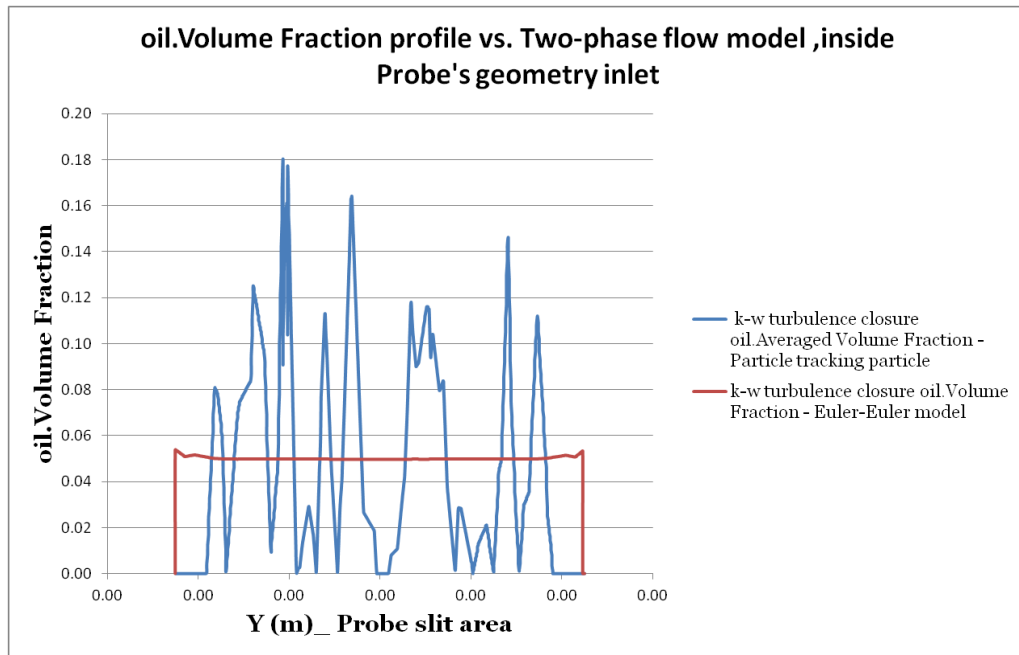


Figure 58: Oil. Volume Fraction profile vs. Two-phase flow model, inside Probe's geometry inlet

After all the data it is possible to see that the particle tracking model is much more sensitive to the particles individual motion, but taken points of measurements cannot represent the measurement over the entire cross section. That why at the table below, it is showed the average oil concentration ratio in the volume of the slit area, for each simulation at pictures 57 and 58. It happens, because when each droplet is tracked over a volume, during a time step or for some time steps, it may or not pass for all the cell inside that volume area, that is why the Figure 59 shows this picks of oil fraction, which does not mean that the average concentration over the probe is different than the one showed at the Euler-Euler simulation.

Table 5: Concentration ratio inside the volume of the probe slit area

concentration ratio a/a_0	Two-phase model
1.00	oil. Volume Fraction - Euler-Euler model with k-w turbulence closure
1.08	oil. Averaged Volume Fraction - Particle tracking particle with k-w turbulence closure

Additionally, in order to better understand the concentration ratio increase after the probe observed in figure 56.. A final study was carried out using the Euler – Lagrange discretization, using again the turbulence model: the k- ω . For the new set of simulations a new geometry was created, and the channel was made longer than the previous one, adding 50 cm after the point where the probe is located. The idea here was to evaluate if the outlet boundary condition was not interfering with the oil concentration ratio behavior. The next figures show the results obtained for the oil concentration ratio, the Turbulence Eddy dissipation and the Turbulence Kinetic Energy, respectively figures 59 and 60.

It is important to highlight here that further simulation was made considering that the minimum number of points of oil droplets injection should be about 5000, it was selected to be the first one in that the oil fraction deviation at the “zero” position from the channel length, at the figure 56, was lower or equal to 5% taken that the deviation was calculated using the as base curves using the maximum injections points where less or equal 5%.

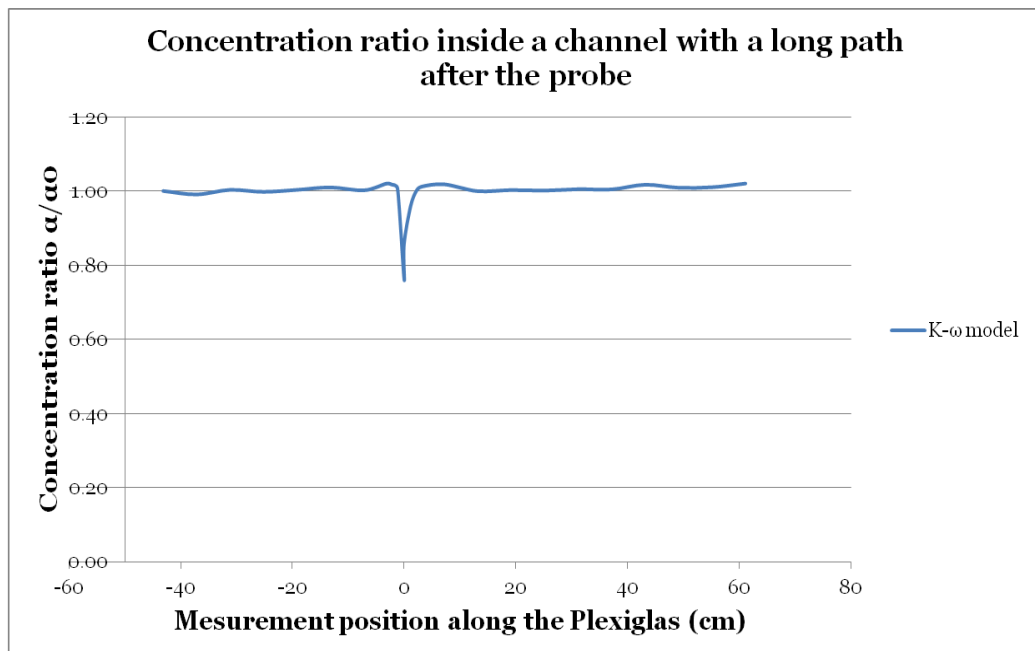


Figure 59: Concentration ratio inside a channel with a long path after the probe

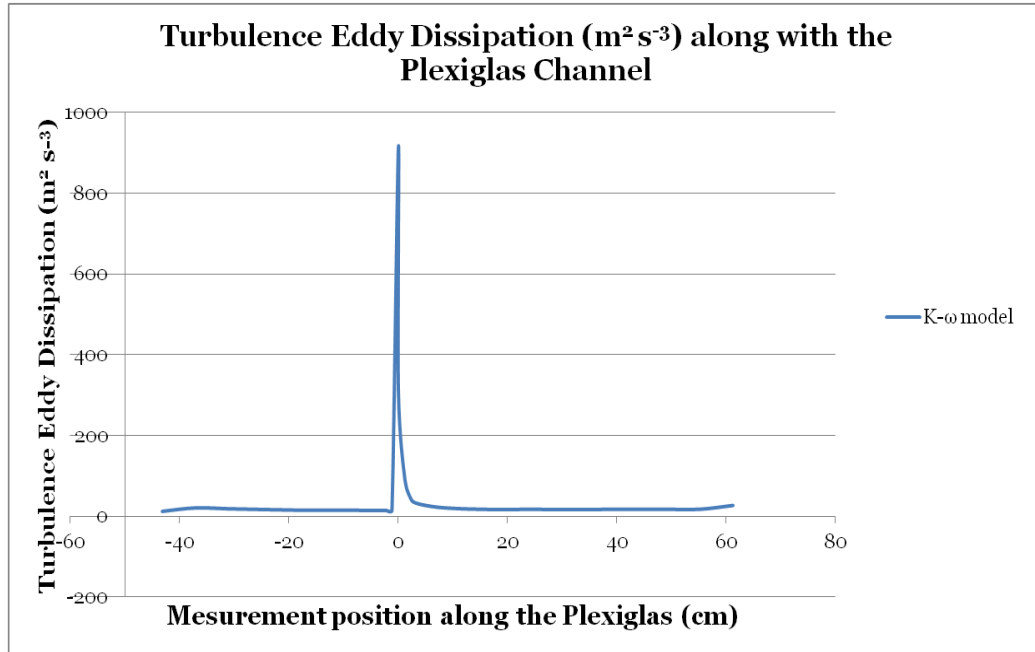


Figure 60: Turbulence Eddy Dissipation ($\text{m}^2 \text{s}^{-3}$) along with the Plexiglas Channel

Basically, in the new set of simulations it is found that for the K- ω model the concentration ratio is essentially the same found before when the original channel was used, and that both the turbulence kinetic energy and the dissipation rate showed a behavior much closer than expected, with an area with much higher values near the probe geometry, which is explained by the drastic restriction of the fluid path at this point. After some distance, the disturbance originated by the blockage effect is dissipated, and the turbulence and the dissipation rate decrease to values close to the ones before the probe.

The last picture in this chapter show the velocity profiles for a plane positioned along the channel, perpendicular to the probe main structure and passing through the middle of the probe slit. As for the velocity profiles, the Figuree 63 shows the velocities vectors, which allow the reader to see that the K- ω model is able to predict formed recirculation areas near to the. The assumption can be supported considering that the K- ω model also produced higher values for the Turbulence Kinetic Energy and Dissipation rate at this area.

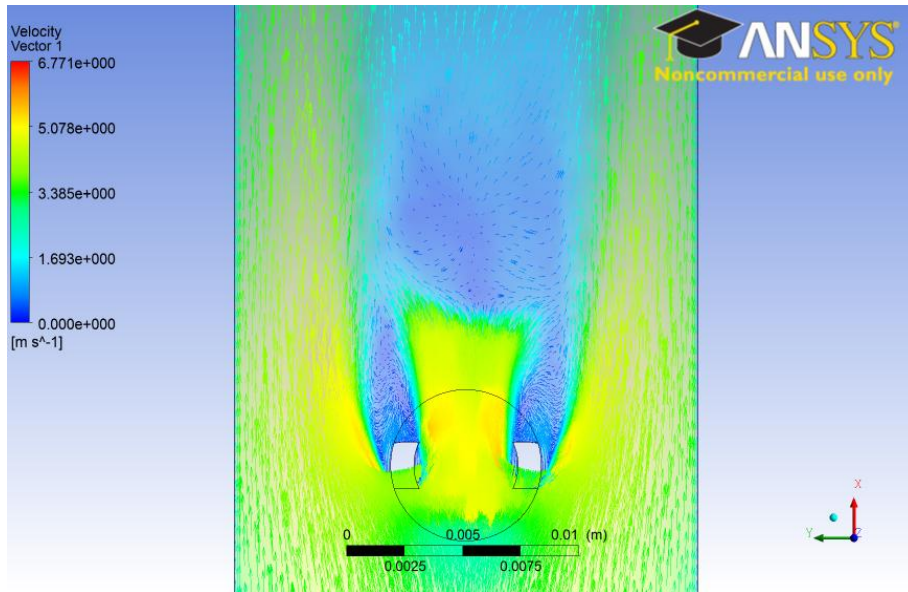


Figure 61: Velocity vector along the Plexiglas channel, for Euler Lagrange simulation and $k-\omega$ turbulence model

5. COMPARATIVE ANALYSIS: SIMULATIONS VS. EXPERIMENTS

The goal of providing in situ measurements prepared according with the two systems set ups described at chapters 3.1 and 3.2 is to validate the simulation data from those systems. Unfortunately due the challenge of finding a equipment able to perform a measurement inside the 1 mm high slit of the probe. The methodology used to validate the simulation data especially in concern of the oil concentration inside the probe, and to observe whether any segregation phenomena can take place due the flow characteristics. Considering that the segregation effects would be most resulting from inertial forces, one way to observe this being only using the spectrophotometry readings is to evaluate the measurement from the same oil concentration for various initial flow speeds, locking for any shift between the spectra for each flow velocity at the system inlet. In addition of what was previous explain about the experiments, in order to have a representative set of results. The experiments were made three times for each concentration.

5.1 In-situ Measurements at the Plexiglas channel

The experiments methodology for the Plexiglas channel was made in agreement with the test descriptions informed at chapter 3.1, as it follows. In addition, with the aim of ensure representativeness of the data collected, the experiments were reapedted three times for each concentration. And for each velocity the spectra was taken 20 times over two minutes, considering that the measurements were made for each speed gradually increasing the frequency of the pump and then repeated lowering the pumping frequency until the initial speed. The next graphs, Figures 62-66, presented the results for the concentrations from 1% up to 10%, in volume. Looking at all the charts for the different concentration of the metalworking fluid, it is possible to admit that there is none or almost no change at the results for each velocity, pointing that for this Plexiglas channel build at laboratory the

segregation effects is not to be considered as a problem over the measurement with the spectrophotometer.

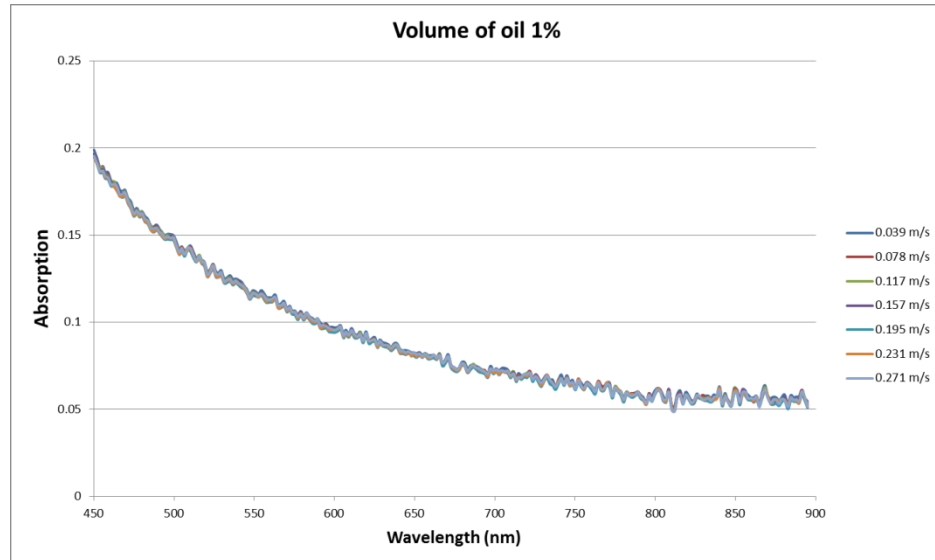


Figure 62: Spectrometer charts, Volume of oil 1%

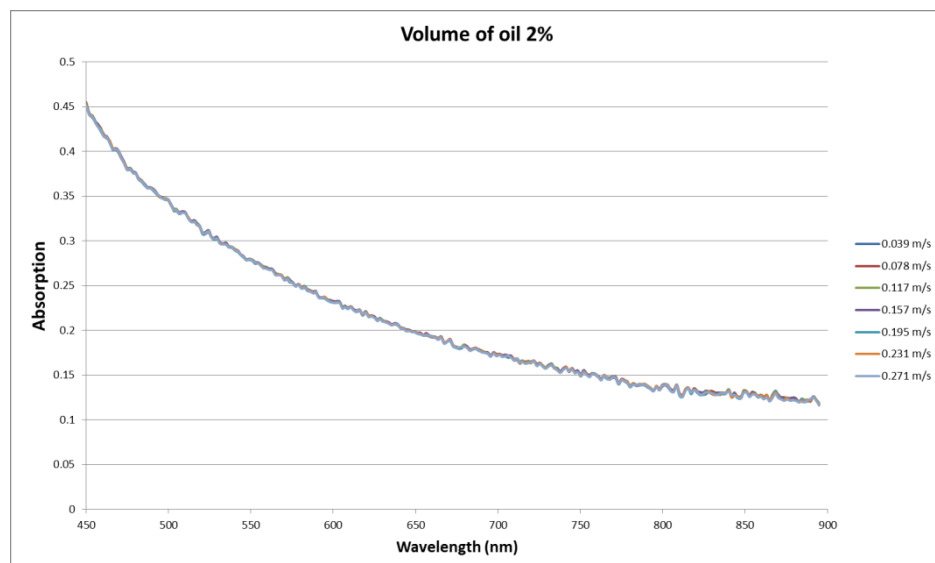


Figure 63: Spectrometer charts, Volume of oil 2%

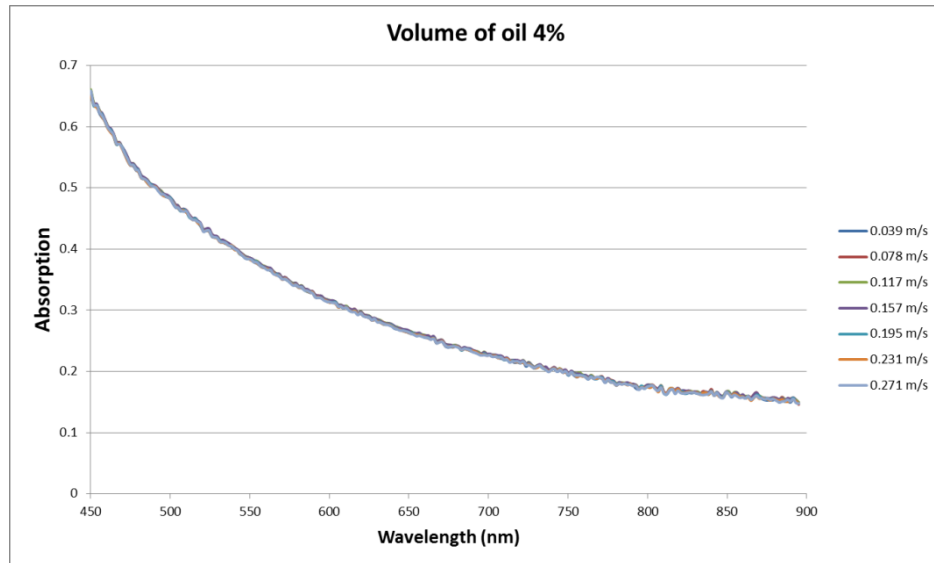


Figure 64: Spectrometer charts, Volume of oil 4%

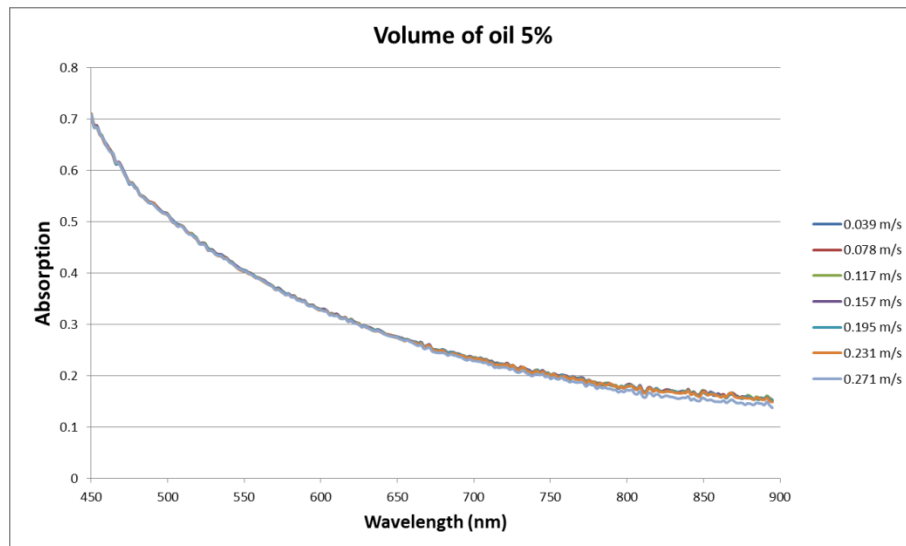


Figure 65: Spectrometer charts, Volume of oil 5%

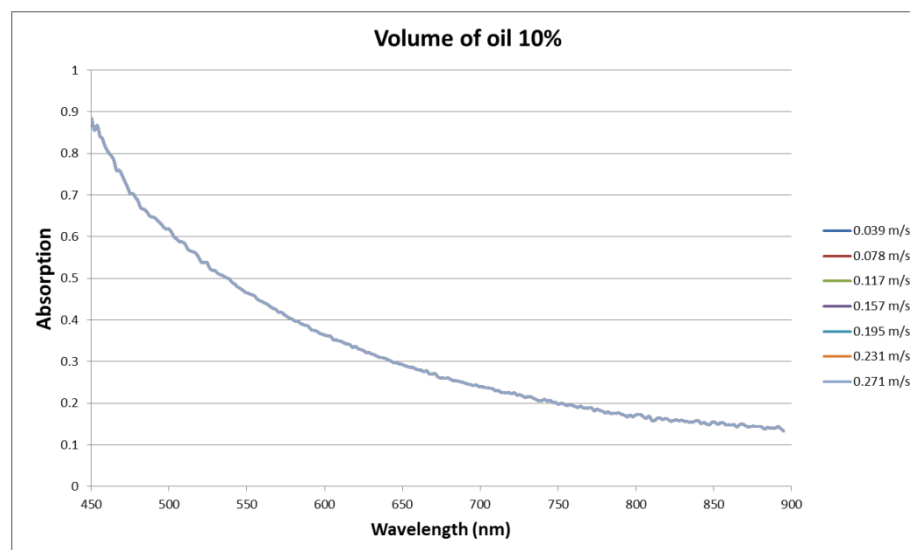


Figure 66: Spectrometer charts, Volume of oil 10%

As final information about the proposed measurement system built should work, using the spectrophotometer, the next chart shows how the probe can easily indicate the alteration that the oil concentration present at the emulsion, a chart was built with the higher inlet flow velocity for each oil concentration studied, see Figure 67.

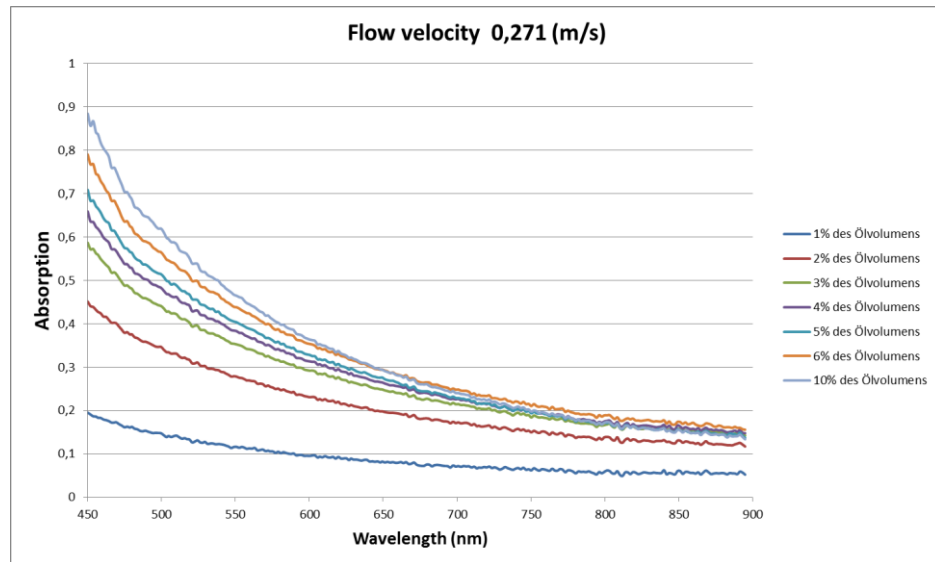


Figure 67: Spectrometer charts from various oil concentrations and fixed flow velocity 0.271(m/s)

5.2 In-situ Measurements using the nozzle adapter directly at the drilling machine

The measurements made direct at the drilling machine, where made at a regular machine that has been daily in operation at the workshop at Bremen University. Consequently none concentration study was performed with the metalwork fluid, since it should be kept at the process concentration all the time, about 5% in volume, although the study with different flow speeds was performed looking again for segregation effects. The measurements were repeated for some days with the some metalwork fluid at the machine during the machine working process, and for each measurement performed a static measurement was performed

with the metal working fluid from the machine, tested using a beaker a recipient. The results are following at the three next figures, Figure 68-69.

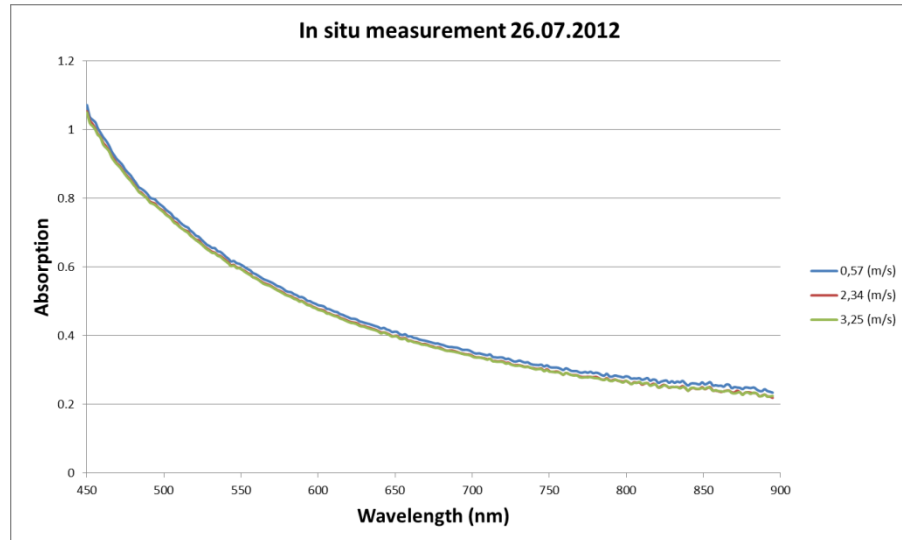


Figure 68: Spectrometer charts from the In situ measurement (26.07.2012)

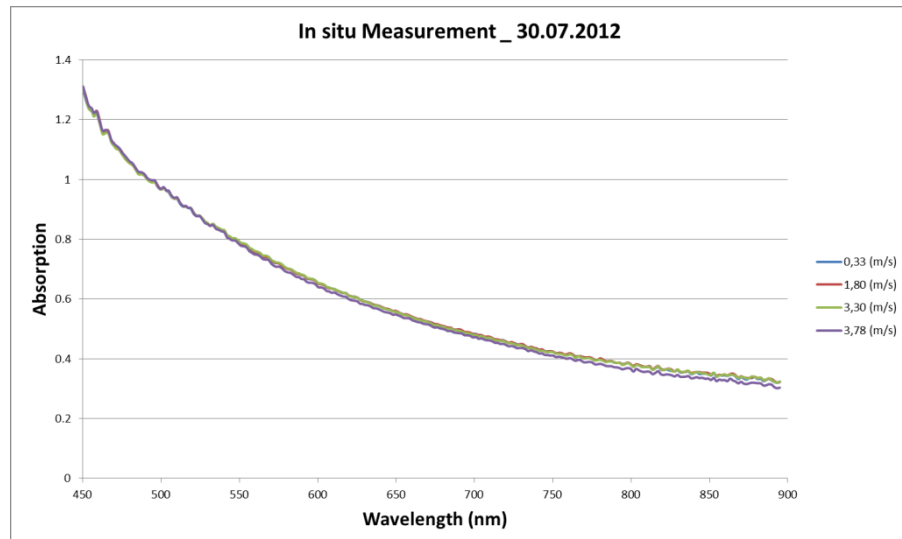


Figure 69: Spectrometer charts from the In situ measurement (30.07.2012)

Once again it is possible to see that the metalworking flow velocity has no influence over the measurement performed with the spectrometer, and it is in agreement with the simulation carried using CFD simulation.

6. CONCLUSIONS

In this work computational fluid dynamics simulations were performed to better understanding and predict the flow behavior inside the scattering area of the slit of a spectrophotometer. In order to ensure the measurement results can correspond to the real concentration of the emulsion. A Euler-Euler approach is used to model the two-phase flow behavior, where each phase was treated as a continuum, one interpenetrating each other, and was represented by averaged conservation equation. Although it is not like a Lagrangian model that can track it particle individually The Euler- Euler approach is faster to process and can give the motion behavior for each class of oil droplet, as they are divided by main diameters.

A first concern was to study the segregation effects around and inside the probe, and a sensibility analysis was performed considering the processes conditions. The results showed that higher the inlet speed, both for the Plexiglas system and the nozzle used direct at the drilling machine, higher the occurrence of segregation effects, as result from inertial forces. The same happens when the main droplet diameter increases. for the cases the MWF droplet diameter range should be found, the segregation effect will not be bigger than 5% a can be neglected.

The sensibility study regarding the probe position is in agreement with the previous studies of segregation, although a position where the side wall of the probe is placed facing the flow stream should be avoided, it still cannot be consider detrimental to the measurements. Again here it was possible to see that the measurement system should be less accurate when the dispersed phase is composed of particles with a droplet size bigger than 10 microns, diameter that should not be found in a MWF during a machine operation.

Additionally it was investigated other subjects: the bacterial adhesion hypothesis, a study concerning the probe geometry and finally a study including a tracking particle model, to compare with the previous simulation.

In agreement with the previous work of the EPM group, for the bacterial adhesion it was considered that a minimum wall shear stress about 3 to 5 Pa was need to prevent bacterial adhesion inside the probe walls. Although, the results found for the probe original geometry indicate that even for the higher inlet velocity the

presence of stagnation areas due the probe inside geometry results in a wall shear stress value high enough to prevent the bacterial adhesion to occur. In response of that fact, a new geometry was proposed to the probe, in order to provide an isokinetic condition for the flow around and inside the probe, and eliminate the recirculation areas.

The probe geometry study was carried just for the Plexiglas geometry and the results were mainly as expected, providing an increased velocity profile inside the probe slit areas, and as a result of that, the wall shear stress was increased as well, therefore increasing the capability of avoiding bacterial adhesion. The odder result of the geometry changing was the sensitivity of the oil concentration ratio inside the probe, by the rate of changing proposed by the increasing of the inlet wall angle of opening, more the oil concentration rate would differ from the start one. The results suggest that even the capability of preventing bacteria adhesion may be increased the geometry of the probe can still be changed to provide a better conditions for both problems, the segregation effect and the bacterial adhesion.

At the end, a tracking particle model was used in order to compeer the results obtained previously, the new set of simulation aim to evaluate if the particle should be considered individually or not. The simulation using the Euler - Lagrange approach where performed using as turbulence model, the k- ω and model. The results from the k- ω turbulence model using the particle tracking model, were used to compeer with the previous data. And the it showed a increased oil rate change when it is compared with the Euler –Euler simulation. Even though it should not invalidate the measurement of the spectrophotometer because the temporal main values measurements may avoid the error cause for the instantaneous fluctuations of velocities caused by the turbulent flow. A more detailed studied is indicated to be carried in the subject.

7. FUTURE WORK

Add the work already done about the wall shear stress at the inner wall of the probe, regarding the possible bacteria adhesion should be summarized and finished to the final work.

Improvement of the probe geometry should be done to avoid the internal recirculation areas and to increase wall shear stress at the walls which would be a way to avoid bacteria adhesion. Perhaps changes like the one showed at the Figure 73.

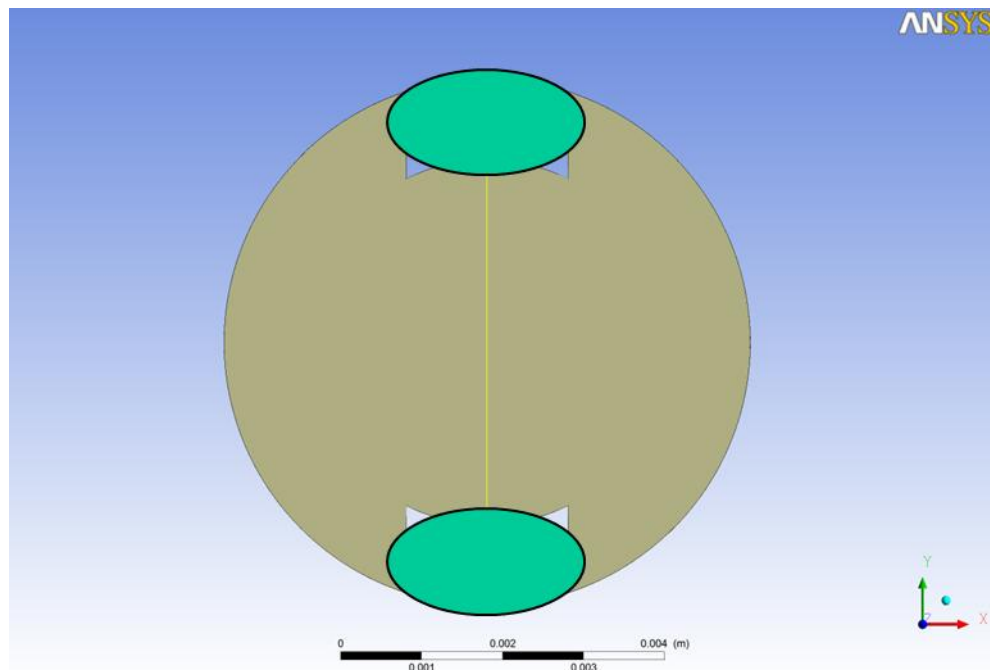


Figure 70: Geometry improvement

Another recommendation for further work is to improve the studied using the particle tracking model, in order to assure that the individual particle behavior will not change the oil concentration rate over the entire path of the channel. More tests could be also performed using the Plexiglas system, to establish more experimental data that could better support the simulation results.

REFERENCES

- Abbassi-Sourki, F., Huneault, M. a., & Bousmina, M. (2009). Effect of compatibilization on the deformation and breakup of drops in step-wise increasing shear flow. *Polymer*, *50*(2), 645–653. doi:10.1016/j.polymer.2008.11.027
- Auton, T. R., Hunt, J. C. R., & Prud'Homme, M. (2006). The force exerted on a body in inviscid unsteady non-uniform rotational flow. *Journal of Fluid Mechanics*, *197*(-1), 241. doi:10.1017/S0022112088003246
- Baden, S. B., Chrisochoides, N. P., Gannon, D. B., & Norman, M. L. (n.d.). *Structured Adaptive Mesh Refinement (SAMR) Grid Methods The IMA Volumes in Mathematics and its Applications* (p. 3). Springer New York.
- Berger, E., & Wille, R. (1972). Periodic Flow Phenomena. *Annual Review of Fluid Mechanics*, *4*(1), 313–340. doi:10.1146/annurev.fl.04.010172.001525
- Binks, B. P. (1998). *Modern Aspects of Emulsions Science*. (B. P. Binks, Ed.) (p. 23). Cambridge: RSC.
- Busscher, H. J., & van der Mei, H. C. (2006). Microbial adhesion in flow displacement systems. *Clinical microbiology reviews*, *19*(1), 127–41. doi:10.1128/CMR.19.1.127-141.2006
- Cai, X., & Wallis, G. B. (1993). The added mass coefficient for rows and arrays of spheres oscillating along the axes of tubes. *Physics of Fluids A: Fluid Dynamics*, *5*(7), 1614. doi:10.1063/1.858838
- Deluhery, J., & Rajagopalan, N. (2005). A turbidimetric method for the rapid evaluation of MWF emulsion stability. *Colloids and Surfaces A: Physicochemical and Engineering Aspects*, *256*(2-3), 145–149. doi:10.1016/j.colsurfa.2004.12.001
- Friedlander, S. K. (1977). *Smoke, Dust and Haze. Fundamentals of Aerosol Behavior* (p. Ch.7 and Ch.10.9). New York: Wiley. doi:978-019512999
- Gerrard, J. H. (1978). The Wakes of Cylindrical Bluff Bodies at Low Reynolds Number. *Philosophical Transactions of the Royal Society A: Mathematical, Physical and Engineering Sciences*, *288*(1354), 351–382. doi:10.1098/rsta.1978.0020
- Gosman, A. D., & Loannides, E. (1983). Aspects of Computer Simulation of Liquid-Fueled Combustors. *Journal of Energy*, *7*(6), 482–490. doi:10.2514/3.62687
- Guillemot, G., Vaca-Medina, G., Martin-Yken, H., Vernhet, A., Schmitz, P., & Mercier-Bonin, M. (2006). Shear-flow induced detachment of *Saccharomyces cerevisiae*

- from stainless steel: influence of yeast and solid surface properties. *Colloids and surfaces. B, Biointerfaces*, 49(2), 126–35. doi:10.1016/j.colsurfb.2006.03.001
- Hama, F. R., Long, J. D., & Hegarty, J. C. (1957). On Transition from Laminar to Turbulent Flow. *Journal of Applied Physics*, 28(4), 388. doi:10.1063/1.1722760
- HIGASHITANI, K., OGAWA, R., HOSOKAWA, G., & MATSUNO, Y. (1982). Kinetic theory of shear coagulation for particles in a viscous fluid. *Journal of Chemical Engineering of Japan*, 15(4), 299–304. doi:10.1252/jcej.15.299
- Jensen, B. B. B., & Friis, A. (2004). Critical wall shear stress for the EHEDG test method. *Chemical Engineering and Processing: Process Intensification*, 43(7), 831–840. doi:10.1016/S0255-2701(03)00101-6
- Kissler. (2012). Recourcenschonende Produktion mit Kühl-Schmierstoffen at 8. Bremer KSS-Workshop.
- Köhler, K. (2010). *Simultanes Emulgieren und Mischen*. Logos Verlag Berlin GmbH.
- Lauder, B. E., & Spalding, D. B. (1974). The numerical computation of turbulent flows. *Computer Methods in Applied Mechanics and Engineering*, 3(2), 269–289. doi:10.1016/0045-7825(74)90029-2
- Laurien, E., & Herbert, O. jr. (2009). *Numerische Strömungsmechanik Grundgleichungen und Modelle – Lösungsmethoden – Qualität und Genauigkeit* (3. Revisio., pp. pp. 15, 50–51, 99– 120). Wiesbaden, pp. 15, 50-51, 99- 120: Vieweg+Teubner Verlag.
- Mollet, H., & Grubenmann, A. (2000). *Formulierungstechnik: Emulsionen, Suspensionen, Feste Formen*. Weinheim: Verlag GmbH.
- Okuyama, K., & Higashitani, K. (2006). *Powder Technology Handbook*. (H. Masuda, K. Higashitani, & H. Yoshida, Eds.) (thid edtio., pp. 183–198).
- Pinsky, M. B., Khain, a. P., & Shapiro, M. (2007). Collisions of Cloud Droplets in a Turbulent Flow. Part IV: Droplet Hydrodynamic Interaction. *Journal of the Atmospheric Sciences*, 64(7), 2462–2482. doi:10.1175/JAS3952.1
- Prasad, A., & Williamson, C. H. K. (1997). Three-dimensional effects in turbulent bluff body wakes. *Experimental Thermal and Fluid Science*, 14(1), 9–16. doi:10.1016/S0894-1777(96)00107-0
- Rusche, H. (2002). Computational Fluid Dynamics of Dispersed Two-Phase Flows at High Phase Fractions, (December).
- Saffman, P. G., & Turner, J. S. (2006). On the collision of drops in turbulent clouds. *Journal of Fluid Mechanics*, 1(01), 16. doi:10.1017/S0022112056000020
- Sander, S. (2012). *Simulation of the multiphase flow within optical transmission probes for emulsion characterization*. Universität Bremen.

- Schubert, H. (2005). *Emulgiertechnik Grundlagen, Verfahren und Anwendungen* (p. 234).
- Shih, W. C. L., Wang, C., Coles, D., & Roshko, A. (1993). Experiments on flow past rough circular cylinders at large Reynolds numbers. *Journal of Wind Engineering and Industrial Aerodynamics*, 49(1-3), 351–368. doi:10.1016/0167-6105(93)90030-R
- Silva, L. F. L. R., Damian, R. B., & Lage, P. L. C. (2008). Implementation and analysis of numerical solution of the population balance equation in CFD packages. *Computers & Chemical Engineering*, 32(12), 2933–2945. doi:10.1016/j.compchemeng.2008.03.007
- Speziale, C. G. (1995). *A REVIEW OF REYNOLDS STRESS MODELS FOR TURBULENT SHEAR FLOWS* (Vol. 0088).
- Speziale, C. G., Sarkar, S., & Gatski, T. B. (2006). Modelling the pressure–strain correlation of turbulence: an invariant dynamical systems approach. *Journal of Fluid Mechanics*, 227(-1), 245. doi:10.1017/S0022112091000101
- Tarnogrodzki, A. (1993). Theoretical prediction of the critical weber number. *International Journal of Multiphase Flow*, 19(2), 329–336. doi:10.1016/0301-9322(93)90006-G
- VDI-Wärmeatlas*. (2006). Berlin, Heidelberg: Springer Berlin Heidelberg. doi:10.1007/978-3-540-32218-4
- Versteeg, H. K., & Malalasekera, W. (2007). *An Introduction to Computational Fluid Dynamics: The Finite Volume Method* (2nd ed.). PRENTICE HALL.
- Wang, W., Gong, J., Ngan, K. H., & Angeli, P. (2009). Effect of glycerol on the binary coalescence of water drops in stagnant oil phase. *Chemical Engineering Research and Design*, 87(12), 1640–1648. doi:10.1016/j.cherd.2009.05.004
- Wijngaarden, L. Van, & Jeffrey, D. J. (2006). Hydrodynamic interaction between gas bubbles in liquid. *Journal of Fluid Mechanics*, 77(01), 27. doi:10.1017/S0022112076001110
- Williamson, C. H. K. (1997). Advances in our understanding of vortex dynamics in bluff body wakes. *Journal of Wind Engineering and Industrial Aerodynamics*, 69-71, 3–32. doi:10.1016/S0167-6105(97)00145-1
- Wolschin, G. (2013). *Hydrodynamik* (pp. 572–573). doi:10.1007/978-3-642-33335-4_81928
- Zdravkovich, M. M. (1997). *Flow Around Circular Cylinders Volume 1: Fundamentals*. Oxford Science Publications.